

# A parametric large-eddy simulation study of wind-farm blockage and gravity waves in conventionally neutral boundary layers

L. Lanzilao<sup>1,†</sup> and J. Meyers<sup>1</sup>

<sup>1</sup>Department of Mechanical Engineering, KU Leuven, Celestijnenlaan 300 – box 2421, B-3001 Leuven, Belgium

(Received 13 June 2023; revised 26 October 2023; accepted 7 December 2023)

We present a suite of large-eddy simulations (LES) of a wind farm operating in conventionally neutral boundary layers. A fixed 1.6 GW wind farm is considered for 40 different atmospheric stratification conditions to investigate effects on wind-farm efficiency and blockage, as well as related gravity-wave excitation. A tuned Rayleigh damping layer and a wave-free fringe-region method are used to avoid spurious excitation of gravity waves, and a domain-size study is included to evaluate and minimize effects of artificial domain blockage. A fully neutral reference case is also considered, to distinguish between a case with hydrodynamic blockage only, and cases that include hydrostatic blockage induced by the air column above the boundary layer and the excitation of gravity waves therein. We discuss in detail the dependence of gravity-wave excitation, flow fields and wind-farm blockage on capping-inversion height, strength and free-atmosphere lapse rate. In all cases, an unfavourable pressure gradient is present in front of the farm, and a favourable pressure gradient in the farm, with hydrostatic contributions arising from gravity waves at least an order of magnitude larger than hydrodynamic effects. Using respectively non-local and wake efficiencies  $\eta_{nl}$  and  $\eta_w$ , we observe a strong negative correlation between the unfavourable upstream pressure rise and  $\eta_{nl}$ , and a strong positive correlation between the favourable pressure drop in the farm and  $\eta_w$ . Using a simplified linear gravity-wave model, we formulate a simple scaling for the ratio  $(1 - \eta_{nl})/\eta_w$ , which matches reasonably well with the LES results.

**Key words:** atmospheric gravity waves, boundary layers, flow blockage, large-eddy simulations, wind farm

† Email address for correspondence: [luca.lanzilao@kuleuven.be](mailto:luca.lanzilao@kuleuven.be)

## 1. Introduction

Conventionally neutral boundary layers (CNBLs) often occur in offshore conditions, with air temperatures adapting to the sea-water temperature given a sufficiently large offshore fetch (Csanady 1974; Smedman, Bergstrom & Grisogono 1997; Lange *et al.* 2004). Such boundary layers are characterized by a neutral stratification, but with a boundary layer that is often capped by a strong stably stratified inversion layer (the capping inversion) and a stably stratified free atmosphere aloft; conditions that are driven by larger weather-scale circulation patterns. When large wind farms are operated in a CNBL, they may excite gravity waves consisting of two-dimensional interface waves on the capping inversion and three-dimensional internal waves in the atmosphere above (Smith 2010; Allaerts & Meyers 2017). These waves alter the pressure field in and around the farm, which result in significant slow down of wind speeds in front of the farm, a phenomenon also known as flow blockage, together with a flow speed up over the farm, which enhances the wake recovery mechanism (Allaerts *et al.* 2018; Blegg *et al.* 2018). With the current and future plans for large offshore wind-farm developments across the world, a better understanding of the interaction of wind farms with CNBLs is necessary.

To date, the number of large-eddy simulation (LES) studies of wind farms operating in CNBLs is limited to a handful of cases. This is mainly due to two facts. First, wind-farm simulations in CNBLs require larger numerical domains than simulations that do not consider thermal stratification above the atmospheric boundary layer (ABL). In fact, the presence of wind-farm induced gravity waves alter the flow fields several tens of kilometres upstream and at the sides of the farm (Allaerts & Meyers 2017, 2019; Maas 2023). Second, the presence of gravity waves requires the use of appropriate methods for inflow and outflow conditions together with non-reflective upper boundary conditions. Only very recently, a first approach was proposed, based on a wave-free fringe-region technique (Lanzilao & Meyers 2023*b*), that does not excite spurious waves at the inlet and outlet of the simulation domain, while still allowing for a turbulent inflow in LES. In the current work we use this approach to set-up a large simulation study that focuses on the influence of thermal stratification above the ABL on wind-farm performance and wind-farm blockage. Moreover, we carefully investigate the effect of domain size on possible artificial domain blockage in case of too small computational domains.

A large part of wind-farm-LES performed in the past decade made use of pressure-driven boundary layers (PDBLs), which refer to ABLs without Coriolis forces, wind veer and thermal stratification. This simplified description of the atmosphere is reasonable when turbines are located in the surface layer, where the Coriolis force and boundary-layer height effects are negligible. Early PDBL wind-farm simulations were, e.g. performed by Meyers & Meneveau (2010), Calaf, Meneveau & Meyers (2010), Wu & Porté-Agel (2011), Lu & Porté-Agel (2011) and Yang, Meneveau & Shen (2014*a,b*). These early studies were characterized by the assumption of ‘infinite’ wind farms, using periodic boundary conditions in all directions, allowing for small simulation domains. With the increase in computational resources, semi-finite and finite wind-farm-LES were performed, with the goal of investigating the flow behaviour also in regions surrounding the farm. Examples of these type of studies are given by Porté-Agel, Wu & Chen (2013), Wu & Porté-Agel (2013), Wu & Porté-Agel (2015), Stevens, Graham & Meneveau (2014*b*), Stevens, Gayme & Meneveau (2014*a*), Stevens, Gayme & Meneveau (2016), Wu *et al.* (2019) and Stieren & Stevens (2022). We note that many more PDBL simulations have been presented in the past, including those looking at stable or unstable surface-layer stratification. We refer to Porté-Agel, Bastankhah & Shamsoddin (2020) for an extensive overview.

With wind turbines growing in size, the assumption that wind farms operate in the inner part of the ABL is more and more questionable. Therefore, Coriolis forces need to be added to the governing equations, giving rise to the Ekman spiral in the ABL. This type of flow, if no (stable) stratification is present in the free atmosphere (nor the surface layer), is defined as a truly neutral boundary layer (TNBL) in the literature. For instance, the simulations in TNBLs performed by Goit & Meyers (2013) and van der Laan *et al.* (2015) clearly show the importance of considering the Coriolis force. However, the equilibrium height of the TNBL can be several kilometres high, scaling with the Rossby–Montgomery height (which is defined as  $u_* / |f_c|$ , where  $u_*$  denotes the friction velocity while  $f_c$  represents the Coriolis frequency). In practice, this situation rarely occurs, as the free atmosphere is usually stratified starting from 0.5 km to 1 km above the ground, damping turbulence and impeding further boundary-layer development. The importance of the inversion layer and stable free atmosphere on the flow within the ABL was, e.g. noted by Csanady (1974) and Zilitinkevich & Esau (2002). Hess (2004) characterized the entrainment of momentum on the boundary layer as a function of the height of the capping inversion using LES while Zilitinkevich & Esau (2003, 2005) and Zilitinkevich, Esau & Baklanov (2007) improved the equilibrium height formulation for the CNBL. More recently, Taylor & Sarkar (2007, 2008) and Pedersen, Gryning & Kelly (2014) used LES to investigate how the capping inversion and free-atmosphere stratification modify the temporal evolution of the CNBL profiles.

Shortly after, CNBLs started to be used also in LES of wind farms. Churchfield *et al.* (2012) and Archer, Mirzaeisefat & Lee (2013) were among the first to perform wind-farm–LES in CNBLs using SOWFA, an OpenFOAM based LES solver. However, both studies mostly focused on wind-farm wakes and turbine–turbine interactions, without reporting on the effects induced by the presence of a capping inversion and a stably stratified free atmosphere. Abkar & Porté-Agel (2013) and Allaerts & Meyers (2015) investigated the farm performance and the vertical entrainment of kinetic energy in the ABL under various capping-inversion strengths and free-atmosphere lapse rates adopting an infinite farm (with periodic boundary conditions). Later, Allaerts & Meyers (2017) explored wind-farm operation in CNBLs using a farm with finite length in the streamwise direction. Here, the vertical domain dimension was extended up to 25 km, to allow for a proper Rayleigh damping layer (RDL) at the top of the domain, since in a semi-finite wind-farm set-up, internal gravity waves can be triggered. They found that the flow divergence induced by the farm pushes upward the inversion layer, generating a cold anomaly that in turn leads pressure feedbacks and a slow down of the flow in front of the farm. This result was earlier predicted by Smith (2010) based on a linear-theory model. Various more recent studies have further investigated this behaviour both using LES (Wu & Porté-Agel 2017; Allaerts *et al.* 2018; Lanzilao & Meyers 2022, 2023b; Maas 2022, 2023; Maas & Raasch 2022) and much faster linearized wind-farm flow models (Allaerts & Meyers 2019; Devesse *et al.* 2022; Smith 2022, 2023).

With the field measurement campaign of Bleeg *et al.* (2018), and later Schneemann *et al.* (2021), demonstrating upstream slow down of the wind speed in the order of  $4 \pm 2\%$  in operational wind farms, a lot of research has started focusing on investigating wind-farm blockage. In the absence of thermal stratification above the ABL, the drag forces introduced by the wind farm are compensated by the difference between in and outgoing momentum. This is possible because the flow can freely expand above the farm, resulting in a minor flow slow down in front of it. Since no hydrostatic forces play a role in this scenario, we name this phenomenon hydrodynamic blockage (i.e. the joined induction of all turbines in the farm). A large part of the literature has claimed this phenomenon to be the root mechanism of flow blockage, which has been investigated using simple analytical

models (Branlard & Meyer Forsting 2020; Branlard *et al.* 2020; Centurelli *et al.* 2021; Segalini 2021), numerical simulations (Bleeg & Montavon 2022; Strickland & Stevens 2020, 2022) and wind-tunnel experiments (Medici *et al.* 2011; Segalini & Dahlberg 2019). These studies report reductions in wind speed at turbine hub height in the order of 1 % to 2 %. In the case of thermal stratification above the ABL, the capping inversion acts as a semi-rigid lid. In fact, the hydrostatic forces related to the displacement of the denser fluid columns above prevent the boundary layer expanding along the vertical direction. Moreover, these forces are further modulated by the excitation of gravity waves. We note that the effects of vertical confinement associated with atmospheric stability and, therefore, hydrostatic forces has been recently investigated also by Smith (2023). Hence, in CNBLs, we name the flow slow down upstream of the farm as hydrostatic blockage. The latter is generally much stronger than the hydrodynamic one, with wind-speed reductions in the order of 10 % and more (Allaerts & Meyers 2017; Maas 2022). Although these studies were performed with a semi-infinite farm, Lanzilao & Meyers (2022, 2023b) and Maas (2023) noted similar behaviour in fully finite farms. Comparing these results with field measurements is rather difficult. In fact, gravity-wave effects extend over distances of several tens of kilometres, which makes them difficult to detect using traditional lidar systems. However, recently, analysis of supervisory control and data acquisition (SCADA) data from the Nordsee Ost and Amrumbank West wind farms located in the German Bight area have shown that velocity deficits and flow-blockage effects are strongly influenced by the capping-inversion height (Cañadillas *et al.* 2023).

In the current article we aim to further investigate relations between wind-farm blockage and capping-inversion height, strength and free-lapse rate, using the LES suite that we present. We remark that our focus is on offshore conditions, where the diurnal cycle is weak and CNBLs occur. The key differences that distinguish our work from others are the use of an appropriate top boundary condition and fringe-region forcing for gravity waves, the presence of a finite farm and the vast set of atmospheric states considered, which allow a more systematic study of the effects of thermal stratification above the ABL. The article is structured as follows. The simulation set-up is elaborated in § 2. Thereafter, § 3 discusses the boundary-layer initialization. Next, the sensitivity of the farm performance to the atmospheric state is shown in § 4. Finally, conclusions are drawn in § 5.

## 2. Methodology

The governing equations and the LES solver are described in §§ 2.1 and 2.2, respectively. Next, the boundary conditions and the buffer layers adopted to minimize wave reflection are discussed in § 2.3. Finally, the numerical set-up, wind-farm layout and atmospheric states are summarized in §§ 2.4, 2.5 and 2.6, respectively.

### 2.1. Governing equations

In the current study we make use of the filtered Navier–Stokes equations with Boussinesq approximation coupled with a transport equation for the potential temperature to investigate the flow in and around a large-scale wind farm (Allaerts & Meyers 2017). Such equations read as

$$\frac{\partial \tilde{u}_i}{\partial x_i} = 0, \quad (2.1)$$

$$\frac{\partial \tilde{u}_i}{\partial t} + \frac{\partial}{\partial x_j} (\tilde{u}_j \tilde{u}_i) = f_c \epsilon_{ij3} \tilde{u}_j + \delta_{i3} g \frac{\tilde{\theta} - \theta_0}{\theta_0} - \frac{\partial \tau_{ij}^{sgs}}{\partial x_j} - \frac{1}{\rho_0} \frac{\partial \tilde{p}^*}{\partial x_i} - \frac{1}{\rho_0} \frac{\partial p_\infty}{\partial x_i} + f_i^{tot}, \quad (2.2)$$

$$\frac{\partial \tilde{\theta}}{\partial t} + \frac{\partial}{\partial x_j} (\tilde{u}_j \tilde{\theta}) = -\frac{\partial q_j^{sgs}}{\partial x_j}, \quad (2.3)$$

where the horizontal directions are denoted with  $i = 1, 2$  while the vertical one is indicated by  $i = 3$ . Moreover,  $\delta_{ij}$  denotes the Kronecker delta while  $\epsilon_{ijk}$  is the Levi–Civita symbol. The filtered velocity and potential-temperature fields are noted with  $\tilde{u}_i$  and  $\tilde{\theta}$ , respectively.

The first term on the right-hand side represents the Coriolis force due to planetary rotation, where the frequency  $f_c = 2\Omega_E \sin \phi$ , with  $\Omega_E$  the Earth angular velocity and  $\phi$  the Earth latitude. The second component of the angular velocity vector  $\Omega_E \cos \phi$  is neglected here since it is negligible when compared with the other terms in the momentum equations (Wyngaard 2010). Thermal buoyancy is taken into account by the second term, where  $g = 9.81 \text{ m s}^{-2}$  denotes the gravitational constant and  $\theta_0$  is a reference potential temperature. Moreover, we make use of the Boussinesq approximation so that the incompressible continuity equation holds. This assumption has two implications. First, fluctuations in density are related to thermal effects rather than pressure ones, so that acoustic waves are filtered out. Second, all density variations from the background state are neglected except for the buoyancy term. Consequently, the thermodynamic equation has a direct influence only on the vertical momentum equation. This is a valid assumption for our study since the scale of the vertical motions is much smaller than the density scale height, which is typically in the order of 7 km (Spiegel & Veronis 1960; Allaerts 2016). Moreover, Maas (2022) performed two wind-farm–LES, one with Boussinesq approximation and one with the anelastic assumption. He found nearly identical numerical results at turbine hub height, with only minor differences several kilometres above the ABL.

The flow is driven across the domain by applying a steady background pressure gradient  $\partial p_\infty / \partial x_i$ , with  $i = 1, 2$ . The latter is related to the geostrophic wind  $G$  through the geostrophic balance, where  $\rho_0$  denotes a reference air density. The pressure oscillations around  $p_\infty$  are denoted with  $\tilde{p}^*$ . Moreover, the term  $f_i^{tot} = f_i + f_i^{ra} + f_i^{fr}$  groups all external forces exerted on the flow. Here,  $f_i^{ra}$  and  $f_i^{fr}$  represent the body forces applied within the RDL and fringe region, respectively, while  $f_i$  denotes the wind-turbine drag force. Finally, the effects of unresolved scales are modelled by the subgrid-scale stress tensor  $\tau_{ij}^{sgs}$  and the subgrid-scale heat flux  $q_j^{sgs}$ . The notations  $(x_1, x_2, x_3)$  and  $(x, y, z)$ ,  $(\tilde{u}_1, \tilde{u}_2, \tilde{u}_3)$  and  $(\tilde{u}, \tilde{v}, \tilde{w})$  and  $\tilde{p}^*$  and  $\tilde{p}$  are used interchangeably. Moreover, for the sake of simplicity, the tilde will not be used in the rest of the article.

## 2.2. Flow solver

The governing equations (2.1)–(2.3) are solved using the SP-Wind solver, an in-house software developed over the past 15 years at KU Leuven (Meyers & Sagaut 2007; Calaf *et al.* 2010; Goit & Meyers 2015; Allaerts & Meyers 2017, 2018; Munters & Meyers 2018; Lanzilao & Meyers 2022, 2023*b*). The solver structure adopted here is mainly based on the version developed and used in Allaerts & Meyers (2017) and Lanzilao & Meyers (2022, 2023*b*). The equations are advanced in time using a classic fourth-order Runge–Kutta scheme with a time step based on a Courant–Friedrichs–Lewy number of 0.4. The streamwise ( $x$ ) and spanwise ( $y$ ) directions are discretized with a Fourier pseudo-spectral method. This implies that all linear terms are discretized in the spectral domain while nonlinear operations are computed in the physical domain, reducing the cost of convolutions from quadratic to log-linear (Fornberg 1996). Furthermore, the 3/2 dealiasing technique proposed by Canuto *et al.* (1988) is adopted to avoid aliasing error.

For the vertical dimension ( $z$ ), an energy-preserving fourth-order finite difference scheme is adopted (Verstappen & Veldman 2003). The effects of subgrid-scale motions on the resolved flow are taken into account with the stability-dependent Smagorinsky model proposed by Stevens, Moeng & Sullivan (2000) with Smagorinsky coefficient set to  $C_s = 0.14$ , similarly to previous studies performed with SP-Wind (Goit & Meyers 2015; Allaerts & Meyers 2017; Munters & Meyers 2018). The constant  $C_s$  is damped near the wall by using the damping function proposed by Mason & Thomson (1992). Furthermore, continuity is enforced by solving the Poisson equation during every stage of the Runge–Kutta scheme. In regard to the turbine trust force, we model it using a non-rotating actuator disk model (Allaerts & Meyers 2015; Goit & Meyers 2015). We refer to Delpont (2010) for more details on the discretization of the continuity and momentum equations while the implementation of the thermodynamic equation and sub-grid scale (SGS) model are explained in detail in Allaerts (2016).

### 2.3. Boundary conditions

The effect of the bottom wall on the flow is modelled with classic Monin–Obukhov similarity theory for neutral boundary layers (NBLs) (Moeng 1984). This wall-stress boundary condition is only dependent on the surface roughness  $z_0$ , which we assume to be constant. We refer to Allaerts (2016) for further details on the implementation. Periodic boundary conditions are naturally imposed at the streamwise and spanwise sides of the computational domain. At the top of the domain, a rigid-lid condition is used, which implies zero shear stress and vertical velocity and a fixed potential temperature. However, in case of stratified free atmospheres, a rigid-lid condition reflects back gravity waves triggered by the wind-farm drag force. To minimize gravity-wave reflection, we adopt a RDL in the upper part of the domain (Klemp & Lilly 1977; Durran & Klemp 1983; Allaerts & Meyers 2017; Lanzilao & Meyers 2023b). This body force dissipates the upward energy transported by gravity waves before it reaches the top of the domain and it reads as

$$f_i^{ra}(\mathbf{x}) = -v(z) (u_i(\mathbf{x}) - U_{G,i}), \tag{2.4}$$

where  $U_{G,1} = G \cos \alpha$ ,  $U_{G,2} = G \sin \alpha$  and  $U_{G,3} = 0$  with  $\alpha$  the geostrophic wind angle. Moreover,  $v(z)$  is a one-dimensional function which reads as

$$v(z) = v^{ra} N \left[ 1 - \cos \left( \frac{\pi}{s^{ra}} \frac{z - (L_z - L_z^{ra})}{L_z^{ra}} \right) \right], \tag{2.5}$$

where  $L_z$  and  $L_z^{ra}$  denote the height of the computational domain and of the RDL, respectively, while  $N = \sqrt{g\Gamma/\theta_0}$  represents the Brunt–Väisälä frequency, with  $\Gamma$  the lapse rate in the free atmosphere. Moreover,  $v^{ra}$  controls the force magnitude while  $s^{ra}$  regulates the function gradient along the vertical direction. Lanzilao & Meyers (2023b) have shown that the quality of the RDL strongly depends on these two tuning parameters, which are carefully tuned with the aim of minimizing gravity-wave reflection; see § 2.4.

The periodic boundary condition along the streamwise direction recycles back the wind-farm wake. To break the periodicity and impose an inflow condition, we use a fringe technique (Spalart & Watmuff 1993; Lundbladh *et al.* 1999; Nordstrom, Nordin & Henningson 1999; Inoue, Matheou & Teixeira 2014; Stevens *et al.* 2014b; Munters,

Meneveau & Meyers 2016; Lanzilao & Meyers 2023b). This body force reads as

$$f_i^{fr}(\mathbf{x}) = -h(x) (u_i(\mathbf{x}) - u_{prec,i}(\mathbf{x})), \tag{2.6}$$

where  $u_{prec,i}(\mathbf{x})$  denotes the statistically steady inflow fields provided by a precursor simulation. Moreover,  $h(x)$  is a one-dimensional non-negative function that is non-zero only within the fringe region, and is expressed as

$$h(x) = h_{max} \left[ F \left( \frac{x - x_s^h}{\delta_s^h} \right) - F \left( \frac{x - x_e^h}{\delta_e^h} + 1 \right) \right] \tag{2.7}$$

with

$$F(x) = \begin{cases} 0 & \text{if } x \leq 0, \\ \frac{1}{1 + \exp \left( \frac{1}{x-1} + \frac{1}{x} \right)} & \text{if } 0 < x < 1, \\ 1 & \text{if } x \geq 1. \end{cases} \tag{2.8}$$

The parameters  $x_s^h$  and  $x_e^h$  denote the start and end of the fringe function support while its smoothness is regulated by  $\delta_s^h$  and  $\delta_e^h$ . Moreover,  $h_{max}$  denotes the maximum value of the fringe function.

Lanzilao & Meyers (2023b) noted that the standard fringe technique triggers spurious gravity waves that propagate through the domain of interest, significantly altering the numerical results. Therefore, in the current study we use the new wave-free fringe-region technique developed by Lanzilao & Meyers (2023b). In addition to applying the body force  $f_i^{fr}$  described above, this technique also damps the convective term in the vertical momentum equation within the fringe region, multiplying it by the following damping function:

$$d(x, z) = 1 - \left[ F \left( \frac{x - x_s^d}{\delta_s^d} \right) - F \left( \frac{x - x_e^d}{\delta_e^d} + 1 \right) \right] \mathcal{H}(z - H). \tag{2.9}$$

Here,  $x_s^d$  and  $x_e^d$  define the start and end of the damping function support while  $\delta_s^d$  and  $\delta_e^d$  control the function smoothness. Moreover,  $H$  denotes the capping-inversion height while  $\mathcal{H}$  represents a Heaviside function. For more details, we refer the reader to Lanzilao & Meyers (2023b) and to § 2.4 below.

#### 2.4. Numerical set-up

The flow solver makes use of two numerical domains concurrently marched in time, i.e. the precursor and main domains. The precursor domain does not contain turbines and is only used for generating a turbulent fully developed statistically steady flow that drives the simulation in the main domain. Similarly to Allaerts & Meyers (2017, 2018), we fix the precursor domain length and width to  $L_x^p = L_y^p = 10$  km, with  $L_z^p = 3$  km. The wind farm is located in the main domain. The first-row turbine should be far enough from the inflow to properly capture the flow slow down in the farm induction region. Moreover, the last-row turbine should be far enough from the fringe region to minimize spurious effects and to let the farm wake to develop. Similarly, the domain width should be large enough to minimize sidewise blockage and to limit the channelling effects at the farm sides. In Appendix A we present an extensive domain sensitivity study, where we analyse in detail the effects of the

domain size on the numerical results. Based on this, we select a domain size of  $L_x \times L_y = 50 \times 30 \text{ km}^2$ , with a distance between the main domain inflow and first-row turbine of  $L_{ind} = 18 \text{ km}$ . This domain size is further used for all simulations performed in § 4. The vertical domain dimension is dictated by the presence of gravity waves. Following previous studies, we fix the main domain height to  $L_z = 25 \text{ km}$  (Allaerts & Meyers 2017, 2018; Lanzilao & Meyers 2022, 2023b). We note that the only reason why we have a domain with such a vertical extent is to allow gravity waves to decay and radiate energy outward (i.e. for minimizing reflectivity).

In SP-Wind the precursor domain width and height should match those of the main domain when they are run concurrently. Therefore, we adopt the tiling technique to extend the precursor flow fields in the  $y$  direction from 10 to 30 km (Sanchez Gomez *et al.* 2023). In regard to the  $z$  direction, we extrapolate the flow fields from 3 to 25 km, using a constant geostrophic wind. At these altitudes the flow is laminar and no turbulence needs to be added. We note that these operations are done offline, i.e. after that the numerical solution has reached a statistically steady state in the precursor domain.

In regard to the grid resolution, we fix  $\Delta x = 31.25 \text{ m}$  and  $\Delta y = 21.74 \text{ m}$  in the streamwise and spanwise direction, respectively. This leads to  $N_x = 1600$  and  $N_y = 1380$  grid points for the main domain and to  $N_x^p = 320$  and  $N_y^p = 460$  points for the precursor domain. A stretched grid is adopted in the vertical direction. The latter is composed of 300 uniformly spaced grid points within the first 1.5 km to capture the strong velocity gradients around the turbine rotor disk, leading to a grid resolution of  $\Delta z = 5 \text{ m}$ . This allows us to obtain a ratio between  $\Delta z$  and the buoyancy length scale  $l_b = 1.69 \overline{w'w'}^{0.5} N^{-1}$ , defined by Brost & Wyngaard (1978), in the capping inversion and free atmosphere above 2 for the majority of the simulation cases (Otte & Wyngaard 2001; Pedersen *et al.* 2014). Next, a first stretch is applied from 1.5 to 15 km, where 180 points are used. A second one is applied in the last 10 km of the domain, i.e. from 15 to 25 km. In summary, the domain is 25 km high and the vertical grid contains a total of 490 grid points. The combination of spanwise and vertical grid resolution allows us to have a total of 9 and 40 grid points along the turbine rotor disk width and height, which is in accordance with simulations in the literature (Calaf *et al.* 2010; Wu & Porté-Agel 2011; Allaerts & Meyers 2017). The combination of precursor and main numerical domains leads to a total of approximately  $5.2 \times 10^9$  degrees of freedom (DOF). We note that this number is evaluated as the product between the number of grid cells and the number of variables (i.e.  $u$ ,  $v$ ,  $w$  and  $\theta$ ). Finally, we also perform four simulations on a domain that contains a single turbine. In these cases, the precursor and main domains have equal sizes (i.e.  $10 \times 10 \times 25 \text{ km}^3$ ). Those simulations are used for evaluating the power output of a turbine that operates in isolation, which will serve in § 4 for computing the non-local efficiency and for scaling some of the results. More information about the single-turbine simulations is reported in Appendix B.

The vertical gravity-wave wavelength derived using gravity-wave linear theory under the hydrostatic assumption is given by  $\lambda_z = 2\pi G/N$ . According to the free-lapse rate values adopted in our study (see § 2.6), the vertical wavelength varies between 3.8 and 10.7 km. Following Klemp & Lilly (1977), who suggested that the depth of the RDL should be at least in the order of  $\lambda_z$ , we set  $L_z^{ra} = 10 \text{ km}$ . Moreover, we fix  $v^{ra} = 5.15$  and  $s^{ra} = 3$ . These parameters minimize gravity-wave reflection and are chosen following the procedure detailed in Lanzilao & Meyers (2023b). The Rayleigh function is shown in figure 1(a).

The body force applied within the fringe region, located at the end of the main domain, should be strong enough to impose the inflow condition without violating the stability constraint imposed by the fourth-order Runge–Kutta method (Schlatter, Adams & Kleiser



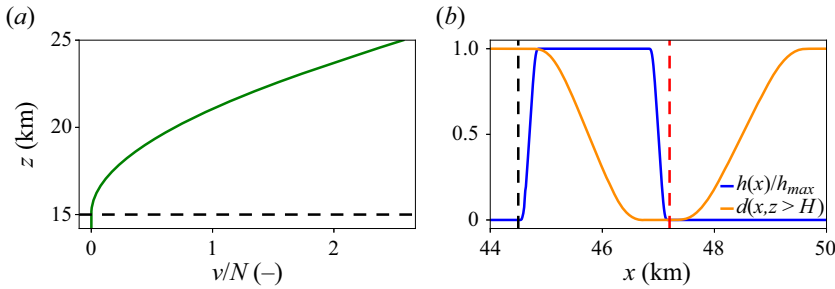


Figure 1. (a) Rayleigh function obtained with  $v^{ra} = 5.15$  and  $s^{ra} = 3$  values. (b) Fringe and damping functions used with the wave-free fringe-region techniques. The black horizontal and vertical dashed lines denote the start of the RDL and the fringe region while the red vertical dashed line marks the end of the fringe forcing. We remark that the fringe region is placed at the end of the main domain.

2005). We carried out some tests (not shown) and we noted that  $h_{max} = 0.3 \text{ s}^{-1}$  satisfies both constraints. Moreover, we fix the fringe-region length to  $L_x^{fr} = 5.5 \text{ km}$ . Given the wind-farm layout (see § 2.5), this means that there are gaps of 18 km and 11.65 km upwind and downwind of the farm. Furthermore, we set  $x_s^h = L_x - L_x^{fr}$ ,  $x_e^h = L_x - 2.8 \text{ km}$  and  $\delta_s^h = \delta_e^h = 0.4 \text{ km}$  while  $x_s^d = x_s^h$ ,  $x_e^d = L_x$ ,  $\delta_s^d = 2.5 \text{ km}$  and  $\delta_e^d = 3 \text{ km}$ . Lanzilao & Meyers (2023b) have shown that this set of parameters minimize the spurious gravity waves triggered by the fringe forcing. The fringe and damping functions are shown in figure 1(b).

### 2.5. Wind-farm layout

The wind-farm set-up is inspired by the work of Lanzilao & Meyers (2022, 2023b). Hence, we have 16 rows and 10 columns for a total of  $N_t = 160$  IEA offshore turbines (Bortolotti *et al.* 2019) with a rated power of  $P_{rated} = 10 \text{ MW}$  arranged in a staggered layout with respect to the main wind direction. The farm is relatively densely spaced with streamwise and spanwise spacings set to  $S_x = S_y = 5D$ , where  $D = 198 \text{ m}$  denotes the turbine rotor diameter. This corresponds to a density of roughly  $P_{rated}/S_x S_y D^2 \approx 10 \text{ MW km}^{-2}$ , where  $s_x = S_x/D$  and  $s_y = S_y/D$  denote the non-dimensional streamwise and spanwise spacings, respectively. We note that this is a relatively dense scenario that is nonetheless considered nowadays in some development areas.

The turbine hub height measures  $z_h = 119 \text{ m}$  while the thrust coefficient is selected from the turbine thrust curve. In this work the undisturbed inflow wind speed varies between 9.1 and 9.5  $\text{m s}^{-1}$  (see table 1), so that all turbines operate below their rated power. Consequently, we fix the thrust coefficient to  $C_T = 0.88$ , which is representative of the values that the thrust set point assumes for wind speeds between 5 and 9.5  $\text{m s}^{-1}$  (Bortolotti *et al.* 2019). The corresponding disk-based thrust coefficient is then  $C'_T = 1.94$  (Calaf *et al.* 2010; Meyers & Meneveau 2010). Moreover, a simple yaw controller is implemented to keep all turbine rotor disks perpendicular to the incident wind flow measured one rotor diameter upstream.

The farm has a length and width of  $L_x^f = 14.85 \text{ km}$  and  $L_y^f = 9.4 \text{ km}$ , respectively. The ratios  $L_{ind}/L_x^f$ ,  $L_x/L_x^f$  and  $L_y/L_y^f$  measure 1.21, 3.37 and 3.19, respectively. We note that in the current work, we only focus on the effect of atmospheric conditions on the flow behaviour given a constant farm layout. Investigating the effects of farm density and shape is a topic for future research.

Cases	$H$ (m)	$\Delta\theta$ (K)	$\Gamma$ (K km <sup>-1</sup> )	$\Delta H$ (m)	$M_{hub}$ (m s <sup>-1</sup> )	$\Pi_{hub}$ (%)	$u_*$ (m s <sup>-1</sup> )	$\alpha$ (°)	$\gamma_v$ (-)	$Fr$ (-)	$P_N$ (-)	$N_t$ (-)
H150- $\Delta\theta 0$ - $\Gamma 0$	—	0.00	0	—	9.47	3.30	0.277	-18.28	1.06	—	—	160
H150- $\Delta\theta 2$ - $\Gamma 1$	251	1.58	1	56	9.47	3.48	0.280	-15.48	1.02	2.53	5.95	160
H150- $\Delta\theta 2$ - $\Gamma 4$	245	1.95	4	48	9.48	3.48	0.280	-15.88	1.03	2.32	3.05	160
H150- $\Delta\theta 2$ - $\Gamma 8$	240	2.36	8	44	9.47	3.40	0.279	-16.29	1.07	2.08	2.11	160
H150- $\Delta\theta 5$ - $\Gamma 1$	211	4.42	1	44	9.47	3.39	0.278	-18.23	1.06	1.63	6.86	160
H150- $\Delta\theta 5$ - $\Gamma 4$	210	4.67	4	42	9.47	3.30	0.277	-18.28	1.06	1.59	3.46	160
H150- $\Delta\theta 5$ - $\Gamma 8$	209	5.00	8	42	9.47	3.32	0.277	-18.40	1.10	1.51	2.36	160
H150- $\Delta\theta 8$ - $\Gamma 1$	196	7.35	1	47	9.46	3.17	0.276	-19.30	1.09	1.30	7.22	160
H150- $\Delta\theta 8$ - $\Gamma 4$	195	7.57	4	48	9.46	3.35	0.276	-19.40	1.08	1.28	3.65	160
H150- $\Delta\theta 8$ - $\Gamma 8$	195	7.87	8	48	9.45	3.08	0.275	-19.32	1.14	1.22	2.44	160
H150- $\Delta\theta 5$ - $\Gamma 4$ -st	210	4.67	4	42	9.47	3.30	0.277	-18.28	1.06	1.59	3.46	1
H300- $\Delta\theta 0$ - $\Gamma 0$	—	0.00	0	—	9.42	3.60	0.281	-12.60	0.97	—	—	160
H300- $\Delta\theta 2$ - $\Gamma 1$	348	1.95	1	57	9.38	3.66	0.280	-11.83	0.98	1.97	4.41	160
H300- $\Delta\theta 2$ - $\Gamma 4$	348	2.19	4	52	9.38	3.68	0.280	-11.87	0.98	1.85	2.20	160
H300- $\Delta\theta 2$ - $\Gamma 8$	347	2.49	8	49	9.39	3.63	0.281	-11.95	0.97	1.75	1.57	160
H300- $\Delta\theta 5$ - $\Gamma 1$	325	4.93	1	67	9.41	3.61	0.281	-12.59	0.97	1.29	4.76	160
H300- $\Delta\theta 5$ - $\Gamma 4$	325	5.15	4	66	9.42	3.60	0.281	-12.60	0.97	1.26	2.38	160
H300- $\Delta\theta 5$ - $\Gamma 8$	326	5.42	8	63	9.41	3.59	0.281	-12.55	0.98	1.22	1.66	160
H300- $\Delta\theta 8$ - $\Gamma 1$	316	7.93	1	78	9.43	3.58	0.281	-12.91	0.98	1.03	4.87	160
H300- $\Delta\theta 8$ - $\Gamma 4$	316	8.15	4	77	9.43	3.59	0.281	-12.92	0.98	1.01	2.43	160
H300- $\Delta\theta 8$ - $\Gamma 8$	316	8.46	8	76	9.43	3.58	0.282	-12.88	0.98	0.99	1.71	160
H300- $\Delta\theta 5$ - $\Gamma 4$ -st	325	5.15	4	66	9.42	3.60	0.281	-12.60	0.97	1.26	2.38	1

Table 1. For caption see next page.

Cases	$H$ (m)	$\Delta\theta$ (K)	$\Gamma$ (K km <sup>-1</sup> )	$\Delta H$ (m)	$M_{hub}$ (m s <sup>-1</sup> )	$\Pi_{hub}$ (%)	$u_*$ (m s <sup>-1</sup> )	$\alpha$ (°)	$\gamma_v$ (-)	$Fr$ (-)	$P_N$ (-)	$N_t$ (-)
H500- $\Delta\theta$ - $\Gamma$ 0	—	0.00	0	—	9.24	3.93	0.277	-9.09	0.93	—	—	160
H500- $\Delta\theta$ 2- $\Gamma$ 1	521	2.04	1	75	9.22	3.95	0.277	-8.94	0.91	1.60	3.04	160
H500- $\Delta\theta$ 2- $\Gamma$ 4	524	2.26	4	68	9.22	3.96	0.277	-8.93	0.92	1.50	1.50	160
H500- $\Delta\theta$ 2- $\Gamma$ 8	523	2.54	8	66	9.22	3.96	0.277	-8.93	0.92	1.42	1.06	160
H500- $\Delta\theta$ 5- $\Gamma$ 1	507	5.05	1	90	9.24	3.92	0.278	-9.08	0.92	1.03	3.10	160
H500- $\Delta\theta$ 5- $\Gamma$ 4	509	5.28	4	87	9.24	3.93	0.277	-9.09	0.93	0.99	1.54	160
H500- $\Delta\theta$ 5- $\Gamma$ 8	511	5.59	8	86	9.24	3.93	0.277	-9.11	0.93	0.97	1.08	160
H500- $\Delta\theta$ 8- $\Gamma$ 1	503	8.05	1	96	9.25	3.93	0.278	-9.14	0.93	0.81	3.11	160
H500- $\Delta\theta$ 8- $\Gamma$ 4	504	8.29	4	94	9.25	3.93	0.278	-9.15	0.93	0.80	1.55	160
H500- $\Delta\theta$ 8- $\Gamma$ 8	504	8.61	8	92	9.25	3.94	0.278	-9.15	0.91	0.79	1.11	160
H500- $\Delta\theta$ 5- $\Gamma$ 4-st	509	5.28	4	87	9.24	3.93	0.277	-9.09	0.93	0.99	1.54	1
H1000- $\Delta\theta$ 0- $\Gamma$ 0	—	0.00	0	—	9.13	4.18	0.275	-7.90	0.86	—	—	160
H1000- $\Delta\theta$ 2- $\Gamma$ 1	1003	2.08	1	96	9.12	4.16	0.275	-7.93	0.86	1.80	1.63	160
H1000- $\Delta\theta$ 2- $\Gamma$ 4	1003	2.32	4	95	9.12	4.15	0.275	-7.97	0.86	1.80	0.82	160
H1000- $\Delta\theta$ 2- $\Gamma$ 8	1003	2.65	8	95	9.14	4.15	0.275	-7.88	0.86	1.80	0.58	160
H1000- $\Delta\theta$ 5- $\Gamma$ 1	1001	5.08	1	99	9.13	4.16	0.275	-7.87	0.86	0.74	1.65	160
H1000- $\Delta\theta$ 5- $\Gamma$ 4	1001	5.33	4	99	9.13	4.18	0.275	-7.90	0.86	0.73	0.82	160
H1000- $\Delta\theta$ 5- $\Gamma$ 8	1001	5.33	8	99	9.13	4.17	0.275	-7.91	0.86	0.70	0.58	160
H1000- $\Delta\theta$ 8- $\Gamma$ 1	1000	8.08	1	100	9.14	4.16	0.275	-7.92	0.86	0.59	1.64	160
H1000- $\Delta\theta$ 8- $\Gamma$ 4	1001	8.33	4	100	9.13	4.16	0.275	-7.98	0.86	0.58	0.82	160
H1000- $\Delta\theta$ 8- $\Gamma$ 8	1001	8.67	8	100	9.13	4.15	0.275	-7.99	0.86	0.57	0.58	160
H1000- $\Delta\theta$ 5- $\Gamma$ 4-st	1001	5.33	4	99	9.13	4.18	0.275	-7.90	0.86	0.73	0.82	1

Table 1. Overview of the spin-up cases used to drive 40 wind-farm simulations and four single-turbine simulations. The parameters are averaged over the last 4 h of the spin-up phase and include the capping-inversion height  $H$ , the capping-inversion strength  $\Delta\theta$ , the free-atmosphere lapse rate  $\Gamma$ , the capping-inversion thickness  $\Delta H$ , the turbulence intensity measured at hub height  $\Pi_{hub}$ , the velocity magnitude measure at hub height  $M_{hub}$ , the friction velocity  $u_*$ , the geostrophic wind angle  $\alpha$ , the shape factor  $\gamma_v$ , the Froude number  $Fr$ , the  $P_N$  number and the number of turbines  $N_t$ . Note that the parameters  $H$ ,  $\Delta\theta$ ,  $\Gamma$  and  $\Delta H$  have been estimated by fitting the spin-up profiles averaged over the last 4 h of the precursor simulations with the Rampanelli & Zardi (2004) model.

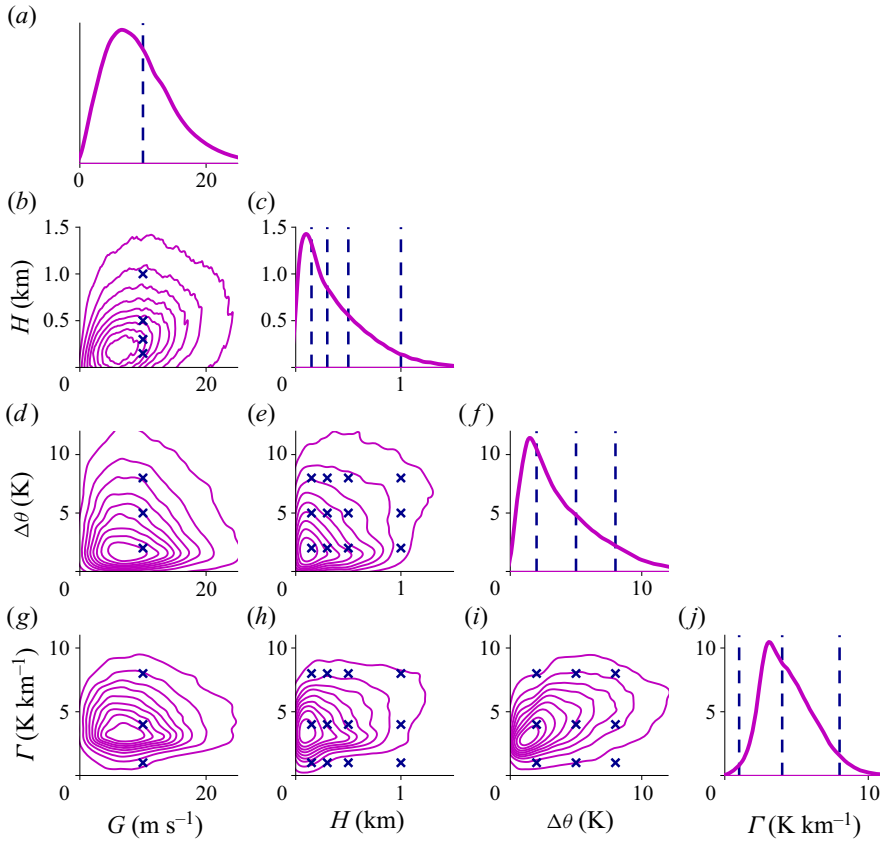


Figure 2. Joint probability density function of the geostrophic wind  $G$ , capping-inversion height  $H$ , capping-inversion strength  $\Delta\theta$  and free-atmosphere lapse rate  $\Gamma$ . The parameters that characterize the CNBL profile are obtained by fitting the ERA5 vertical potential-temperature profile between the surface level and 2.5 km using the Rampanelli & Zardi (2004) model. The geostrophic wind is obtained by taking the mean velocity magnitude between the top of the capping inversion and 2.5 km. The blue vertical dashed lines and crosses denote the parameters selected in the current study, i.e.  $G = 10 \text{ m s}^{-1}$ ,  $H = 150, 300, 500, 1000 \text{ m}$ ,  $\Delta\theta = 2, 5, 8 \text{ K}$  and  $\Gamma = 1, 4, 8 \text{ K km}^{-1}$ . All combinations are considered, for a total of 36 cases.

### 2.6. Atmospheric state

To select a range of relevant atmospheric states, we analysed 30 years of ERA5 re-analysis data (from 1988 to 2018) measured at 51.6N 3.0E, which is the nearest grid point to the Belgian–Dutch offshore wind-farm cluster. We use the model proposed by Rampanelli & Zardi (2004) to fit the vertical potential-temperature profile from the surface level up to 2.5 km, using a least square fit to all levels in this range. The outputs of this model consist of an estimate of the capping-inversion height  $H$  and strength  $\Delta\theta$  and lapse rate  $\Gamma$  in the free atmosphere. To evaluate the geostrophic wind, we compute the mean velocity magnitude between the top of the capping inversion and 2.5 km.

The subplots on the diagonal of figure 2 display the probability density functions of such parameters while the joint probability density functions are shown in the off-diagonal subplots. In this study we fix the geostrophic wind to  $10 \text{ m s}^{-1}$ , which is in line with previous studies (Abkar & Porté-Agel 2013; Wu & Porté-Agel 2017; Allaerts & Meyers 2017, 2018; Lanzilao & Meyers 2022). We note that this value is also chosen so that all turbines operate below their rated power and in a region where the thrust curve typically

shows a rather constant thrust-coefficient value. In regard to the capping-inversion height, we select the values of 150, 300, 500 and 1000 m, so that we can explore farm operations in shallow and deep boundary layers. The capping-inversion strength  $\Delta\theta$  is set to 2, 5 or 8 K while we fix  $\Gamma$  to 1, 4 or 8 K km<sup>-1</sup>. This wide variety of capping-inversion strengths and free-lapse rates allows us to study the influence of interfacial and internal waves on farm energy extraction and flow blockage. The ground temperature and the capping-inversion thickness are fixed to  $\theta_0 = 288.15$  K and  $\Delta H = 100$  m for all simulations. The blue crosses in [figure 2](#) denote the 36 atmospheric states that we selected. Finally, we fix the latitude to  $\phi = 51.6^\circ$ , which leads to a Coriolis frequency of  $f_c = 1.14 \times 10^{-4}$  s<sup>-1</sup>, and the surface roughness to  $z_0 = 1 \times 10^{-4}$  m for all simulations. This value represents calm sea conditions and enters in the range of values observed over the North Sea, and more generally offshore (Taylor & Yelland 2000; Allaerts & Meyers 2017; Kirby, Nishino & Dunstan 2022; Lanzilao & Meyers 2022). We note that we also include four additional simulations of a wind-farm operating in neutral atmospheres, which will be further discussed in § 3.3. More details on the atmospheric states selected and the suite of simulations performed are reported in [table 1](#).

In the remainder of the text, the state variables will be accompanied by a bar in case of time averages. For the horizontal averages along the full streamwise and spanwise directions, we use the angular brackets  $\langle \cdot \rangle$ . The notations  $\langle \cdot \rangle_f$  and  $\langle \cdot \rangle_s$  are used to represent spanwise averages along the width of the farm (i.e. from first- to last-turbine column) and at its side, respectively. In case of a horizontal average over the full spanwise direction and along the turbine rotor height or capping-inversion thickness, we adopt the notation  $\langle \cdot \rangle_r$  and  $\langle \cdot \rangle_c$ , respectively. For instance, the notation  $\langle \cdot \rangle_{f,r}$  represents a spanwise average over the farm width and a vertical average over the turbine rotor height. We refer to [figure 23](#) in [Appendix A](#) for more details. Finally, we note that the RDL and fringe region will be left out of the figures in the remainder of the main text.

### 3. Boundary-layer initialization

The spin-up of the precursor simulations is discussed in § 3.1. After the spin-up phase, we start the main domain simulation and we perform a wind-farm start-up phase driven by the precursor simulation, during which the flow adjusts to the presence of the farm. This phase is discussed in § 3.2. Finally, we discuss the methodology used to perform simulations in a NBL reference case in § 3.3.

#### 3.1. Generation of a fully developed turbulent flow field

The various  $H$ ,  $\Delta\theta$  and  $\Gamma$  values selected are combined together to form 36 atmospheric states, which range from a shallow boundary layer with a strong inversion layer and free-atmosphere stratification, to a deep boundary layer with low  $\Delta\theta$  and  $\Gamma$  values. The initial vertical potential-temperature profiles are generated giving the  $H$ ,  $\Delta\theta$  and  $\Gamma$  values as input to the Rampanelli & Zardi (2004) model. For the initial velocity profile, we use a constant geostrophic wind above the capping inversion. Within the ABL, we use the Zilitinkevich (1989) model with friction velocity  $u_* = 0.26$  m s<sup>-1</sup>, which is in the range of values observed by Brost, Lenschow & Wyngaard (1982). The velocity profiles below the capping inversion are then combined with the laminar profile in the free atmosphere following the method proposed by Allaerts & Meyers (2015).

Next, we add random divergence-free perturbations with an amplitude of  $0.1G$  in the first 100 m to the vertical velocity profiles. This initial state is given as input to the precursor simulation. Since no turbines are located in the domain, the only drag force

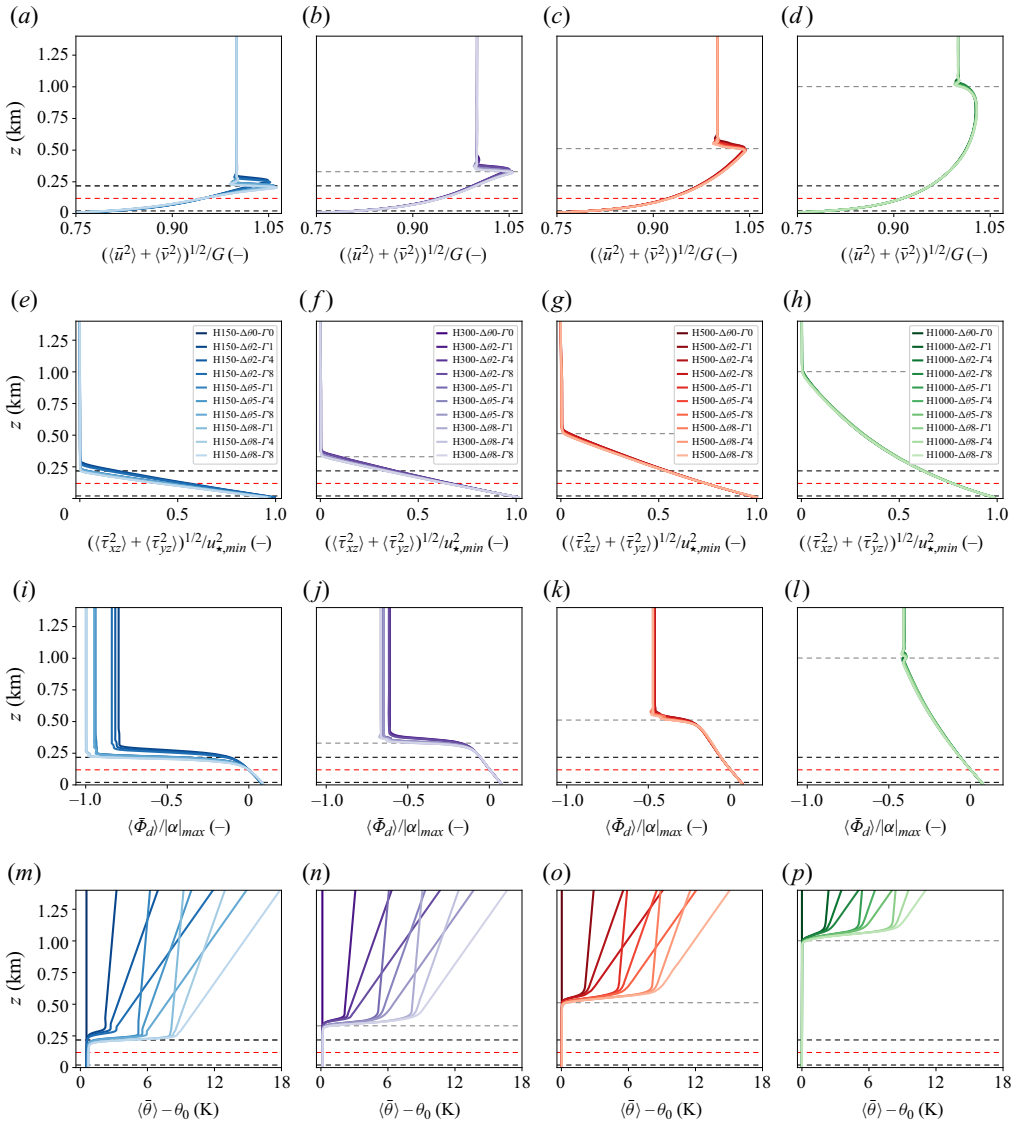


Figure 3. Vertical profiles of (a–d) velocity magnitude, (e–h) shear stress magnitude, (i–l) wind direction and (m–p) potential temperature averaged along the full horizontal directions and over the last 4 h of the simulation. The results are shown for (a,e,i,m) H150, (b,f,j,n) H300, (c,g,k,o) H500 and (d,h,l,p) H1000 cases using various capping-inversion strengths and free-atmosphere lapse rates. Moreover, the profiles are further normalized with  $G = 10 \text{ m s}^{-1}$ ,  $u_{*,min} = 0.275 \text{ m s}^{-1}$ ,  $|\alpha|_{max} = 19.4^\circ$  and  $\theta_0 = 288.15 \text{ K}$ . The red dashed line denotes the turbine hub height while the black dashed lines are representative of the rotor dimension. Finally, the grey dashed line represents the averaged inversion-layer height. We note that the results shown here only refer to the precursor simulations.

acting on the flow is the wall stress. The flow is advanced in time for 20 h, which is sufficient to obtain a turbulent fully developed statistically steady state (Pedersen *et al.* 2014; Allaerts & Meyers 2017; Lanzilao & Meyers 2023b). Figure 3 illustrates vertical profiles of several quantities of interest averaged over the last 4 h of the simulations and over the full horizontal directions. Figure 3(a–d) shows the velocity magnitude normalized

with the geostrophic wind. The boundary layer extends up to the capping inversion, which limits its growth. All velocity profiles show a common feature, that is, the presence of a super-geostrophic jet near the top of the ABL, which is a typical phenomenon observed in this type of atmospheric conditions. Pedersen *et al.* (2014) investigated the evolution of this super-geostrophic jet in detail, while, e.g. Goit & Meyers (2015, Appendix B) and Allaerts & Meyers (2015) mathematically derived the existence of such jets by following on the findings of Zilitinkevich (1989). We note that this phenomenon is more accentuated for the H150 cases, where a stronger wind shear along with stronger velocity gradients at the top of the ABL are attained. Next, figure 3(e–h) displays the shear stress magnitude, which is non-zero only below the capping inversion, with a quasi-linear profile. We note that varying  $\Delta\theta$  and  $\Gamma$  results in very minor differences in terms of velocity and shear stresses. Next, figure 3(i–l) shows the flow angle. At turbine hub height, the flow is parallel to the  $x$  direction. This is achieved by using the wind-angle controller developed and tuned by Allaerts & Meyers (2015), which is designed to ensure a desired orientation of the hub-height wind direction ( $\Phi_d = 0^\circ$  in this case). Below the turbine-tip height, the flow is almost unidirectional since most of the wind-direction change occurs within the inversion layer, except for deep boundary layers. The geostrophic wind angle, which is the angle between the surface stress and the geostrophic wind velocity, is larger for shallow boundary layers, as noted by Allaerts & Meyers (2017). Finally, the thermal stratification is illustrated in figure 3(m–p) by means of potential-temperature profiles. For sake of completeness, we also show the neutral cases here. However, we note that those cases are artificially generated (see § 3.3).

The various spin-up cases together with some parameters of interest averaged over the last 4 h of simulation are summarized in table 1. During the spin-up phase, the capping-inversion height moves slightly upward. The increase in inversion-layer height is more accentuated for the shallow boundary-layer cases. For instance, the H150 cases show a growth of 67 m on average over the 20 h of spin-up. However, the height of the capping inversion is still below turbine-tip height for six of those cases. For the H1000 cases, the boundary-layer height remains unaltered. This result is consistent with the equilibrium theory of Csanady (1974) and with previous LES findings (Pedersen *et al.* 2014; Allaerts & Meyers 2015, 2017). The capping-inversion strength slightly increases for the majority of the cases while the free-atmosphere stratification remains unchanged. The velocity magnitude at turbine hub height varies between 9.1 and 9.5 m s<sup>-1</sup> among all cases, meaning that turbines operate in the region 2 (Bortolotti *et al.* 2019). Moreover, the turbulence intensity at turbine hub height varies from 3.3 % to 4.1 %. These values are in line with those observed by Barthelmie *et al.* (2009) and Türk & Emeis (2010) over the North Sea. The large variance in the Froude number, defined as  $Fr = U_B/\sqrt{g'H}$  with  $U_B$  the bulk velocity along the  $x$  direction (i.e. the streamwise velocity averaged over the full streamwise and spanwise directions and along the boundary-layer height) and  $g' = g\Delta\theta/\theta_0$  the reduced gravity, will allow us to analyse the flow response to wind-farm forcing under critical ( $Fr \approx 1$ ), subcritical ( $Fr \leq 1$ ) and supercritical ( $Fr \geq 1$ ) conditions with varying  $P_N = U_B^2/NGH$  numbers. We note that, while the pressure feedback due to interfacial waves depends upon the  $Fr$ , the  $P_N$  number relates to the pressure perturbation induced by internal waves (see Smith (2010) and Allaerts & Meyers (2019) for more details). Both the  $Fr$  and  $P_N$  number values for all cases are reported in table 1.

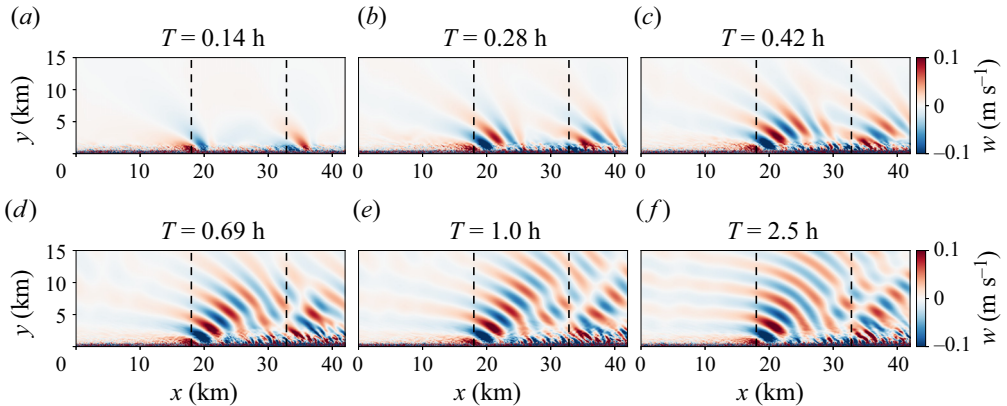


Figure 4. Instantaneous contours of vertical velocity for case H500- $\Delta\theta_2$ - $\Gamma_8$  obtained (a–d) during the wind-farm start-up phase, (e) at the end of the wind-farm start-up phase and (f) at the end of the simulation. The  $x$ - $z$  plane is taken along the centreline of the domain, i.e. at  $y = 15$  km. The black vertical dashed lines denote the location of the first- and last-row turbine. We note that the fringe region and RDL are not displayed in the plots.

### 3.2. Wind-farm start-up phase

The turbulent fully developed inflow profiles previously discussed are now used to drive the simulation in the main domain, where the turbines impose a drag force on the flow. However, before collecting flow statistics over time, a second spin-up phase is required. In fact, the flow has to adjust to the presence of the farm in the main domain before reaching a new statistically steady state. We name this phase wind-farm start-up. Figure 4 shows the time evolution of the vertical velocity field on an  $x$ - $z$  plane for case H500- $\Delta\theta_2$ - $\Gamma_8$ . The flow divergence induced by the farm drag force displaces upward the capping inversion, which in turn triggers a first train of internal gravity waves in proximity to the first-row turbine location. *Vice versa*, the flow convergence in the farm wake moves the capping inversion downward, generating a second train of internal waves at the last-row turbine location. This is clearly visible in figure 4(a). The two out-of-phase trains of waves are convected downstream, until they eventually merge at  $T = 1$  h, as shown in figure 4(e). At this point, the numerical solution is further advanced in time for 1.5 h. The instantaneous vertical velocity flow field taken at  $T = 2.5$  h is displayed in figure 4(f). By comparing the numerical solution at  $T = 1$  h against that obtained at  $T = 2.5$  h, we note minimal differences. A similar behaviour is observed for the streamwise and spanwise velocity fields (not shown). This means that 1 h of wind-farm spin-up time suffices for the flow to adjust to the farm drag force. We note that other cases have similar velocity magnitude at hub height (see table 1), meaning that the number of flow-through times would be very similar to that of case H500- $\Delta\theta_2$ - $\Gamma_8$ . Therefore, similarly to Allaerts & Meyers (2017) and Lanzilao & Meyers (2022), we fix the duration of the wind-farm start-up phase to 1 h, which corresponds to roughly two and a half wind-farm flow-through times. Next, we switch off the wind-angle controller in the precursor simulation and we collect statistics during a time window of 1.5 h.

### 3.3. Construction of a neutral boundary-layer reference case

For each inversion-layer height, we also include a case characterized by the absence of the capping inversion and a neutral free atmosphere, an idea originally proposed



by Lanzilao & Meyers (2022). To do so, the fringe forcing in the main domain only forces the velocity field to the one provided by the CNBL developed in the precursor domain, leaving the potential temperature constant with height. To give an example, case H500- $\Delta\theta$ - $\Gamma$ 0 is driven by the flow fields obtained in the precursor simulation of case H500- $\Delta\theta$ - $\Gamma$ 4, but sets the temperature profile in the main domain to a constant value. Consequently, in this case, the farm operates under the same turbulent inflow velocity profile but in the absence of thermal stratification above the ABL. We note that the same strategy is used for cases H150- $\Delta\theta$ - $\Gamma$ 0, H300- $\Delta\theta$ - $\Gamma$ 0 and H1000- $\Delta\theta$ - $\Gamma$ 0. This is admittedly a numerical construction that does not really exist in reality but allows us to factor out effects due to thermal stratification above the ABL. It has however also some drawbacks. For instance, the capping-inversion height is much lower than the Ekman-layer equilibrium height that the boundary layer would attain in a TNBL. Therefore, in the main domain, the flow within the ABL inevitably starts mixing with the free atmosphere, varying its shear and veer already before reaching the first-row turbine location. In the H150- $\Delta\theta$ - $\Gamma$ 0 and H300- $\Delta\theta$ - $\Gamma$ 0 cases, this flow mixing is very high, varying considerably the flow profiles. For instance, the flow angle at the farm entrance measures approximately  $10^\circ$  in the H150- $\Delta\theta$ - $\Gamma$ 0 case. However, this effect becomes negligible in the H500- $\Delta\theta$ - $\Gamma$ 0 and H1000- $\Delta\theta$ - $\Gamma$ 0 cases, where the flow remains parallel to the streamwise direction and, in general, profiles show very similar results in front of and across the farm, with a farm efficiency of 47.0 % and 46.7 %, respectively. Therefore, we use case H500- $\Delta\theta$ - $\Gamma$ 0 as a reference simulation for a farm operating in the absence of thermal stratification above the ABL in the rest of this article, and we refer to it as the NBL reference case.

A working example of this idea is given in figure 5(a,b), which displays the flow field obtained in the main domain for the NBL reference case (i.e. H500- $\Delta\theta$ - $\Gamma$ 0) and the H500- $\Delta\theta$ - $\Gamma$ 4 case, respectively. The two simulations are driven by the same turbulent inflow profiles. However, the potential-temperature profile is set to a constant in figure 5(a) while figure 5(b) uses the potential temperature provided by the precursor simulations. By comparing the results of these two simulations, it is easy to investigate the effects induced by the thermal stratification above the ABL on the wind-farm flow behaviour. The various differences will be analysed in detail in § 4.

#### 4. Sensitivity of wind-farm performance to the atmospheric state

The wind-farm flow development under various atmospheric conditions is examined in this section. First, we perform a qualitative analysis on the separate effects of varying the capping-inversion height, strength and free-atmosphere lapse rate on farm performance in §§ 4.1 and 4.2, respectively. Next, we compare the LES results against various one- and two-dimensional gravity-wave linear-theory models in § 4.3. Thereafter, we carry out a quantitative comparison in terms of state variables among all simulation cases in § 4.4. Finally, the column-averaged wind-farm power output is presented in § 4.5, followed by a discussion on the non-local, wake and farm efficiencies in § 4.6, where we also propose a new scaling parameter for the ratio of the non-local to wake efficiency.

##### 4.1. Effects of the inversion-layer height on the flow development

We start our analysis with figure 6, which shows the  $x$ - $z$  plane across the sixth column of turbines of the instantaneous horizontal velocity magnitude together with the base and top of the inversion layer computed by fitting the LES data with the Rampanelli & Zardi (2004) model. Every turbine imparts a force on the flow, generating a patch of low wind

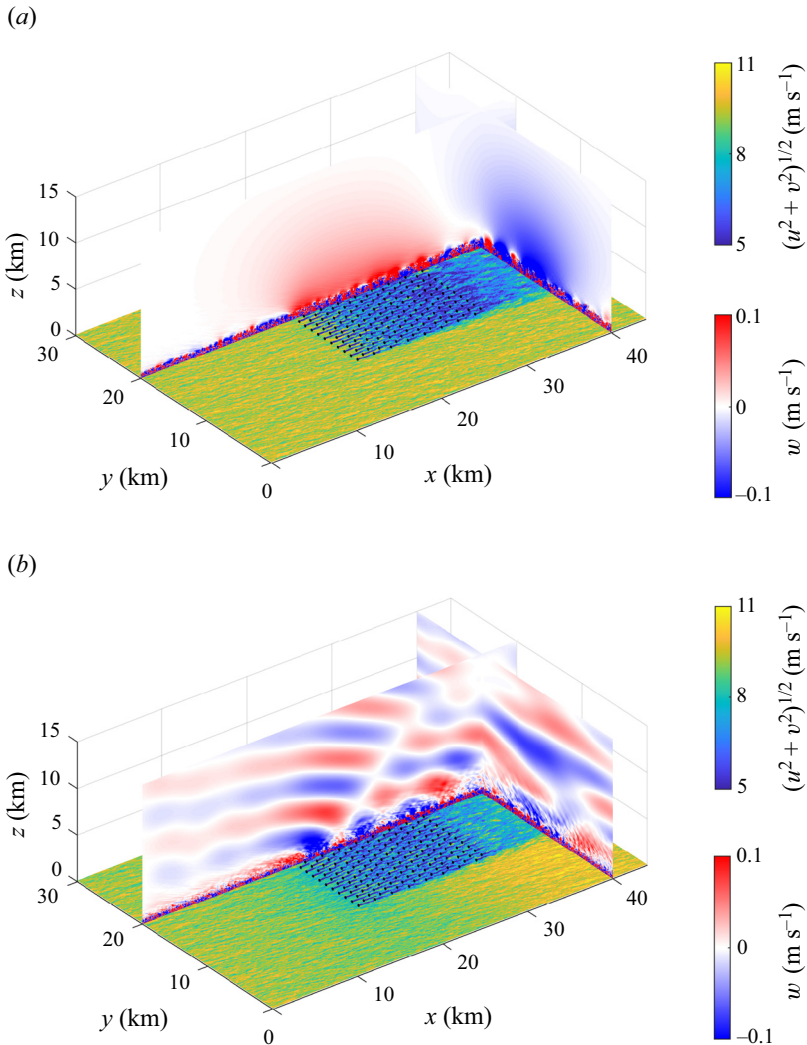


Figure 5. Snapshot of the instantaneous flow field obtained after 2.5 h of simulation time in the (a) NBL reference case and in (b) CNBL conditions. The two simulations correspond to cases H500- $\Delta\theta$ 0- $\Gamma$ 0 and H500- $\Delta\theta$ 5- $\Gamma$ 4, respectively. The  $x$ - $y$  plane shows contours of velocity magnitude  $(u^2 + v^2)^{1/2}$  taken at turbine hub height while the  $x$ - $z$  and  $y$ - $z$  planes display the vertical velocity field. The black disks denote the wind-turbine rotor locations. Finally, we note that the fringe region and RDL are not displayed. We remark that the only difference in the NBL reference case consists in the absence of thermal stratification above the ABL.

speed downwind. Figure 6(a) shows that such velocity deficits are very strong in a shallow boundary layer. In fact, the turbine-tip height is in close proximity to the capping-inversion base, which limits energy entrainment and, therefore, flow mixing, slowing down the wake recovery process. Moreover, this also limits the growth of the internal boundary layer (IBL) generated by the wind-turbine wakes expansion. Therefore, to conserve mass, the flow deceleration is mostly compensated by a flow redirection at the sides of the farm, generating high-speed flow channels. This is visible in figure 7(a), which shows the time-averaged turbine-orientation angle with respect to the streamwise direction for all turbines in the farm. Here, the angles between the first- and last-turbine columns vary

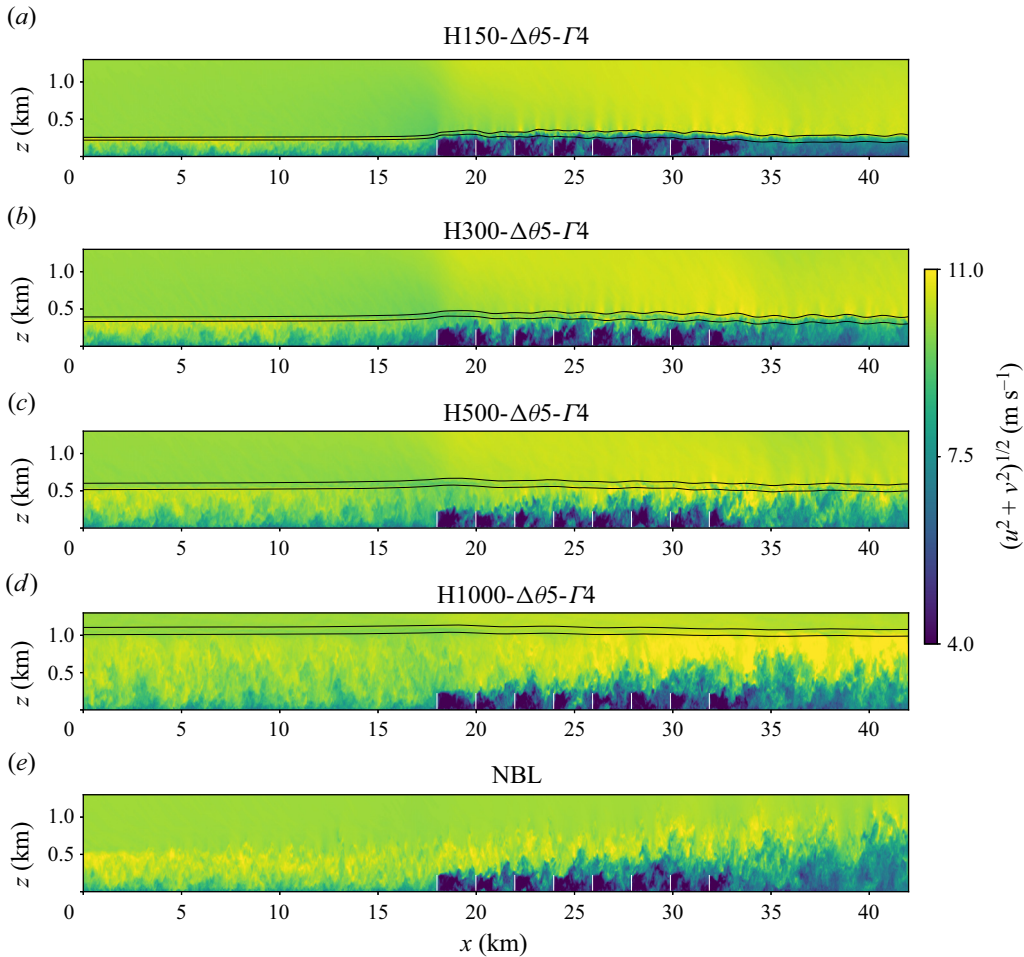


Figure 6. Contours of the instantaneous horizontal velocity magnitude in an  $x$ - $z$  plane taken across the sixth column of turbines, i.e. at  $y = 15.25$  km, for cases (a) H150- $\Delta\theta 5$ - $\Gamma 4$ , (b) H300- $\Delta\theta 5$ - $\Gamma 4$ , (c) H500- $\Delta\theta 5$ - $\Gamma 4$ , (d) H1000- $\Delta\theta 5$ - $\Gamma 4$  and (e) the NBL reference case. The black lines represent the bottom and top of the inversion layer computed with the Rampanelli & Zardi (2004) model. Finally, the location of the turbine rotor disks is indicated with vertical white lines. The NBL reference case refers to simulation H500- $\Delta\theta 0$ - $\Gamma 0$ .

between  $-8^\circ$  and  $8^\circ$ . The asymmetry with respect to the domain centreline observed in figure 7 is due to the presence of the Coriolis effects. The upward motion caused by the strong flow divergence results in a capping-inversion vertical displacement, which reaches a maximum in proximity to the second-row turbines, with a relative capping-inversion displacement of 42.9%. A strong wind-speed reduction is also observed in the farm induction region. Furthermore, the low level of energy entrainment also causes a strong wind-farm wake. The interaction between the IBL and capping inversion decreases as  $H$  increases. We observe in figure 6(c) that the vertical wake expansion reaches the inversion-layer height only in the farm wake.

For a deep boundary layer, the capping-inversion effects on the wind-farm response become negligible. Here, the IBL does not interact with the inversion layer. This also allows a high-speed flow region to form between the IBL and capping-inversion base, as shown in figure 6(d), which enhances flow mixing and consequently the vertical transport

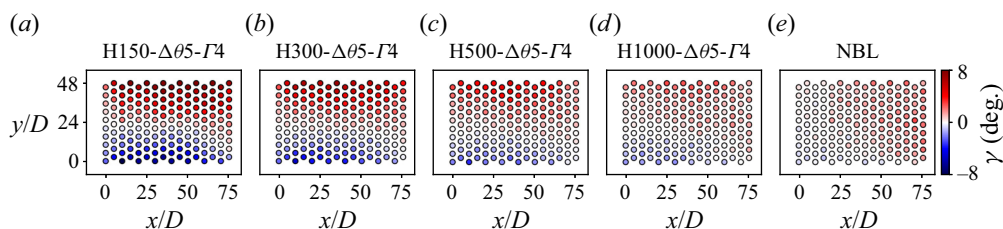


Figure 7. Turbine-orientation angle with respect to the streamwise direction for cases (a) H150- $\Delta\theta_5$ - $\Gamma_4$ , (b) H300- $\Delta\theta_5$ - $\Gamma_4$ , (c) H500- $\Delta\theta_5$ - $\Gamma_4$ , (d) H1000- $\Delta\theta_5$ - $\Gamma_4$  and (e) the NBL reference case. The latter refers to simulation H500- $\Delta\theta_0$ - $\Gamma_0$ .

of energy (not shown here), therefore replenishing the turbine and farm wake at a higher rate. This also translates into a much smaller flow redirection at the farm sides since the vertical expansion of the IBL is not constrained by the inversion layer. Figure 7(d) shows variation in turbine-orientation angles only between  $-2^\circ$  and  $2^\circ$  for this case. In all atmospheres with thermal stratification above the ABL, figure 6 shows that the turbulent structures are damped by the inversion layer, leaving the free atmosphere non-turbulent. A different behaviour is observed in figure 6(e), which illustrates the results obtained in a neutral atmosphere. The turbulence structures at the top of the boundary layer are not damped by buoyant forces in this case, allowing the IBL to reach higher altitudes. Here, the reduction in wind speed caused by the turbines is solely balanced by the boundary-layer thickening. In fact, figure 7(e) shows that all turbines have positive orientation angles, which gradually increase towards the last row.

The upward displacement of the inversion layer, which has to be considered as an interfacial wave, brings air with a lower potential temperature to a higher altitude, generating a cold anomaly. This is illustrated in figure 8, which shows the  $x$ - $z$  plane of the time-averaged potential-temperature perturbation field together with the base and top of the inversion layer, averaged in the horizontal directions along the farm width. The negative perturbation in the potential-temperature field is about 7 and 2 K in cases H150- $\Delta\theta_5$ - $\Gamma_4$  and H1000- $\Delta\theta_5$ - $\Gamma_4$ , respectively. This considerable difference is caused by the higher inversion-layer displacement attained in case H150- $\Delta\theta_5$ - $\Gamma_4$  (and in shallow boundary-layer flows, in general), which measures 42.9% (i.e. 90 m) against the 3.8% (i.e. 40 m) obtained for case H1000- $\Delta\theta_5$ - $\Gamma_4$ . We note that the cold anomaly extends to the farm induction region in all cases. Moreover, the interfacial waves along the capping inversion are also clearly visible. In fact, figure 8 shows that the interfacial-wave crests correspond to high potential-temperature perturbations. Finally, the flow acceleration in the wind-farm wake pushes the inversion layer downward, generating a hot anomaly. Since the ABL itself is neutral, potential-temperature perturbations do not occur below the inversion layer.

As noted by Smith (2010) and Allaerts & Meyers (2017), variations in the potential-temperature field are strongly correlated to pressure perturbations. In fact, a cold anomaly translates into a higher column of cold and heavy air, which locally increases pressure. *Vice versa*, a hot anomaly generates a region of low pressure. This behaviour is illustrated in figure 9, which shows an  $x$ - $z$  plane of the time-averaged pressure-perturbation field together with the base and top of the inversion layer, averaged in the horizontal directions along the farm width. The strong cold anomaly generated in shallow boundary layers gives rise to strong increases in pressure, with a peak in the farm entrance region. This strong counteracting pressure gradient extends across the whole farm induction region. By comparing figure 9(a,d), it becomes clear that the unfavourable pressure

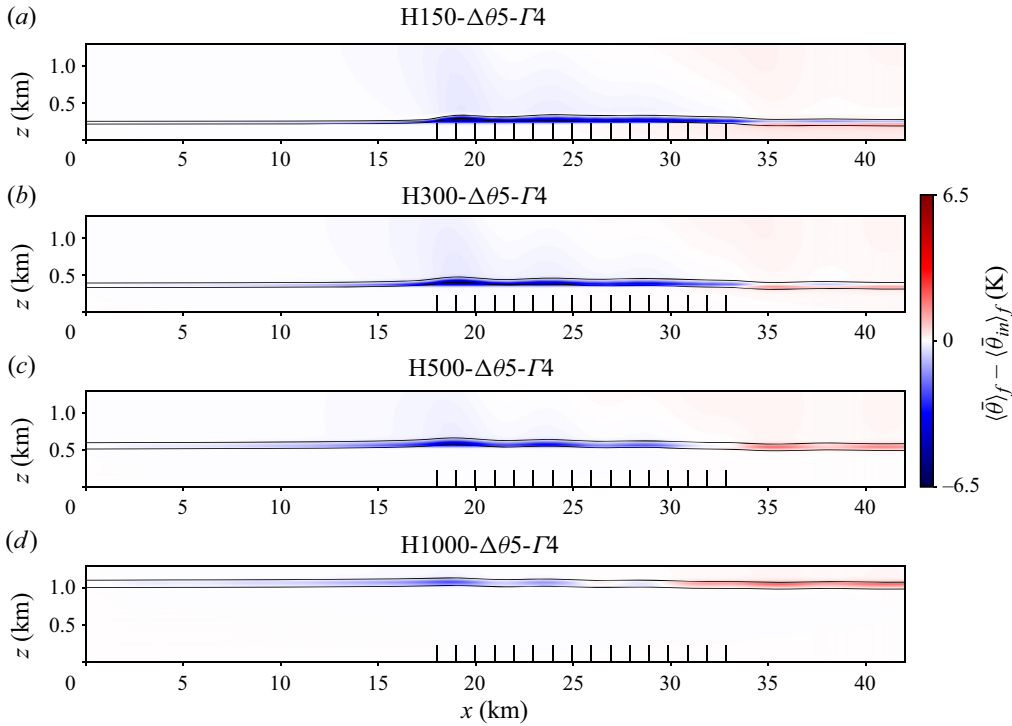


Figure 8. Contours of the time-averaged potential-temperature perturbation with respect to the inflow in an  $x$ - $z$  plane further averaged in the  $y$  direction along the width of the farm for cases (a) H150- $\Delta\theta$ 5- $\Gamma$ 4, (b) H300- $\Delta\theta$ 5- $\Gamma$ 4, (c) H500- $\Delta\theta$ 5- $\Gamma$ 4 and (d) H1000- $\Delta\theta$ 5- $\Gamma$ 4. The black lines represent the bottom and top of the inversion layer computed with the Rampanelli & Zardi (2004) model. Finally, the location of the turbine rotor disks is indicated with vertical black lines.

gradient is inversely proportional to the capping-inversion height. The low pressure region downwind of the farm generated by the hot anomaly gives rise to a favourable pressure gradient across the farm that enhances the wake recovery mechanism. Finally, figure 9(e) shows the pressure perturbation obtained in a neutrally stratified atmosphere. Here, the unfavourable pressure gradient, which is solely due to the flow slow down caused by the cumulative turbine induction, is an order of magnitude lower than that obtained in stratified atmospheres and only extends up to roughly six rotor diameters upstream of the first-row turbines. Moreover, also the favourable pressure gradient is negligible when compared with that obtained in the presence of thermal stratification above the ABL.

#### 4.2. Effects of the inversion-layer strength and free-atmosphere lapse rate on the flow development

Following the work of Klemp & Lilly (1975) and Vosper (2004), Sachsperger, Serafin & Grubišić (2015) derived a two-dimensional gravity-wave linear model in which they found that the wavenumber  $k_x$  of the interfacial waves depends upon the capping-inversion strength and Brunt-Väisälä frequency as follows:

$$k_x = \frac{g\Delta\theta}{2U_B^2\theta_0} + \frac{N^2\theta_0}{2g\Delta\theta}. \quad (4.1)$$

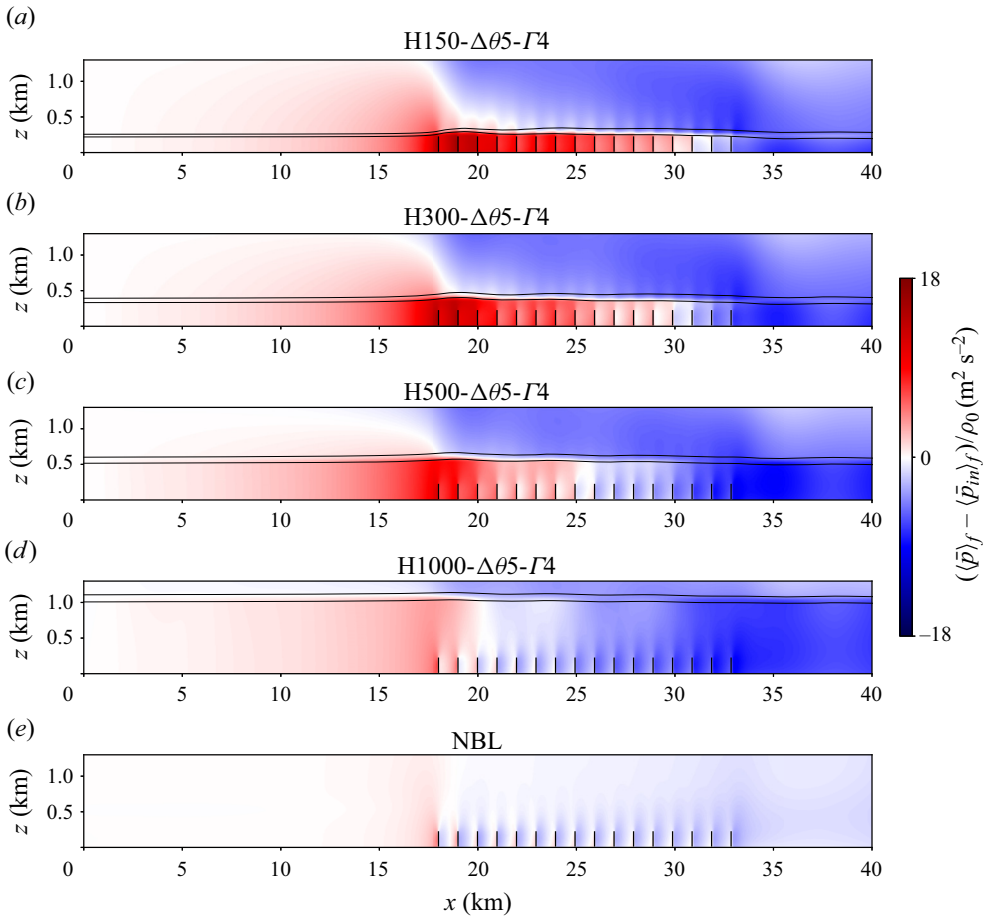


Figure 9. Contours of the time-averaged pressure perturbation with respect to the inflow in an  $x$ - $z$  plane further averaged in the  $y$  direction along the width of the farm for cases (a) H150- $\Delta\theta$ 5- $\Gamma$ 4, (b) H300- $\Delta\theta$ 5- $\Gamma$ 4, (c) H500- $\Delta\theta$ 5- $\Gamma$ 4, (d) H1000- $\Delta\theta$ 5- $\Gamma$ 4 and (e) the NBL reference case. The black lines represent the bottom and top of the inversion layer computed with the Rampanelli & Zardi (2004) model. Finally, the location of the turbine rotor disks is indicated with vertical black lines. The NBL reference case refers to simulation H500- $\Delta\theta$ 0- $\Gamma$ 0.

Sachsperger *et al.* (2015) showed that, under a constant Brunt-Väisälä frequency, the interfacial-wave horizontal wavelength  $\lambda_x = 2\pi/k_x$  is inversely related to the strength of the capping inversion  $\Delta\theta$ . Consequently, when  $\Gamma$  is kept constant, a stronger capping inversion supports interfacial waves with a lower wavelength. This is visible in figure 10, where we compare  $x$ - $y$  planes taken at the turbine hub height of velocity magnitude, vertical velocity and pressure perturbation of three simulations where the only varying parameter is  $\Delta\theta$ . Figure 10(a-c) shows that a higher  $\Delta\theta$  causes a higher flow speed up at the farm sides. This is due to the fact that, on average, a high inversion-layer strength reduces the capping-inversion upward displacement. Consequently, the flow rate at the farm sides has to increase to compensate for the limited thickening of the boundary layer. The vertical velocity fields shown in figure 10(e-g) clearly illustrate that the upward motion caused by these waves propagates down to turbine hub height, generating patches of low and high wind speed. According to (4.1), the interfacial-wave wavelength is 6.1 and 4 km for cases H500- $\Delta\theta$ 5- $\Gamma$ 1 and H500- $\Delta\theta$ 8- $\Gamma$ 1, which is in line with the 7.3 km and

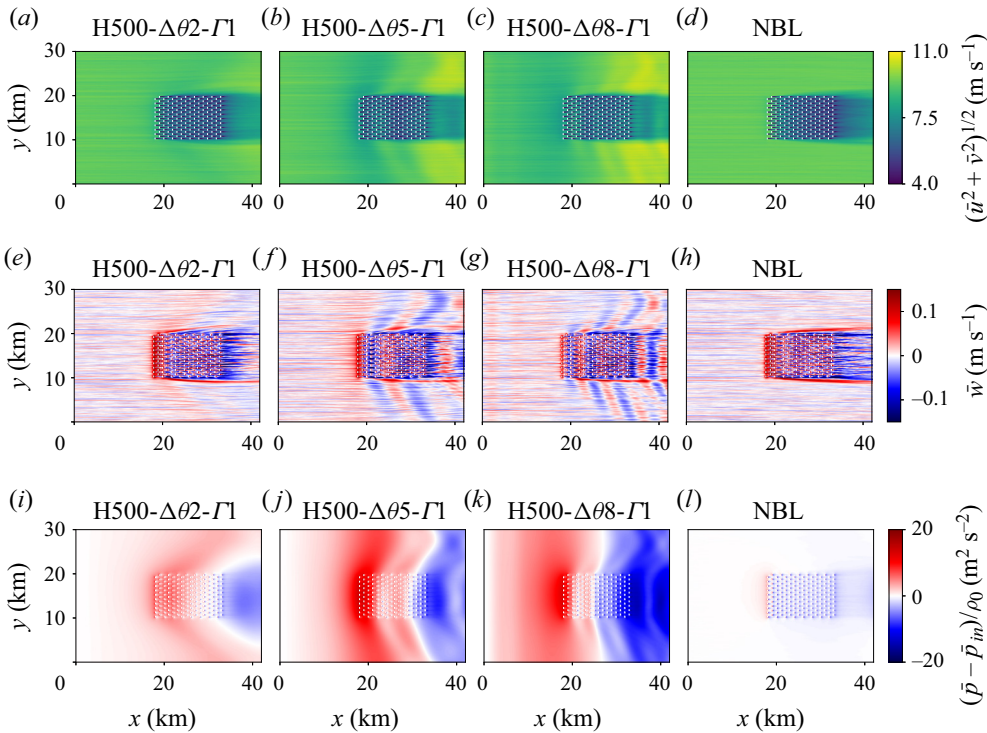


Figure 10. Contours of the time-averaged (*a–d*) velocity magnitude, (*e–h*) vertical velocity and (*i–l*) pressure perturbation in an *x–y* plane taken at turbine hub height for cases (*a,e,i*) H500- $\Delta\theta 2-\Gamma 1$ , (*b,f,j*) H500- $\Delta\theta 5-\Gamma 1$ , (*c,g,k*) H500- $\Delta\theta 8-\Gamma 1$  and (*d,h,l*) the NBL reference case. The location of the turbine rotor disks is indicated with vertical white lines. The NBL reference case refers to simulation H500- $\Delta\theta 0-\Gamma 0$ .

4.9 km observed in figure 10(*f,g*). However,  $\lambda_x$  measures 10.1 km for case H500- $\Delta\theta 2-\Gamma 1$ , which corresponds to 2/3 of the farm length. For this case, interfacial waves are not visible in figure 10(*a,e,i*). We speculate that a longer domain is necessary for these waves to become clearly visible. We also remark the presence of a V-shape pattern at the farm sides, which is very similar to that noted by Allaerts & Meyers (2019). This phenomenon will be further discussed in § 4.3.

Finally, figure 10(*i–k*) displays pressure perturbation with respect to the inflow value. Here, we note that the pressure oscillations seem to be superimposed on top of a large-scale gradient. We believe that the large-scale gradient is caused by the global displacement of the capping inversion. Interfacial waves further corrugate this surface, giving rise to the pressure oscillations particularly visible in figure 10(*j,k*), which have a similar wavelength to the trapped lee waves observed in figure 10(*f,g*). Furthermore, we note that the footprint of the counteracting pressure gradient in the farm induction region together with the favourable one across the farm is positively correlated with  $\Delta\theta$ . However, case H500- $\Delta\theta 5-\Gamma 4$  shows the highest pressure-perturbation magnitude, the latter being roughly 1.5 times that obtained in case H500- $\Delta\theta 2-\Gamma 1$ . We speculate that this is due to the choking effect (Smith 2010), since  $Fr = 0.99$  in this case. Moreover, the V-shape pattern causes a favourable pressure gradient also at the farm sides, which further enhances the channelling effects. We note that the recycling of pressure perturbations along the spanwise direction suggests that the domain width should be further increased in future studies. Finally, figure 10(*d,h,l*) shows the results obtained in the NBL reference case. As

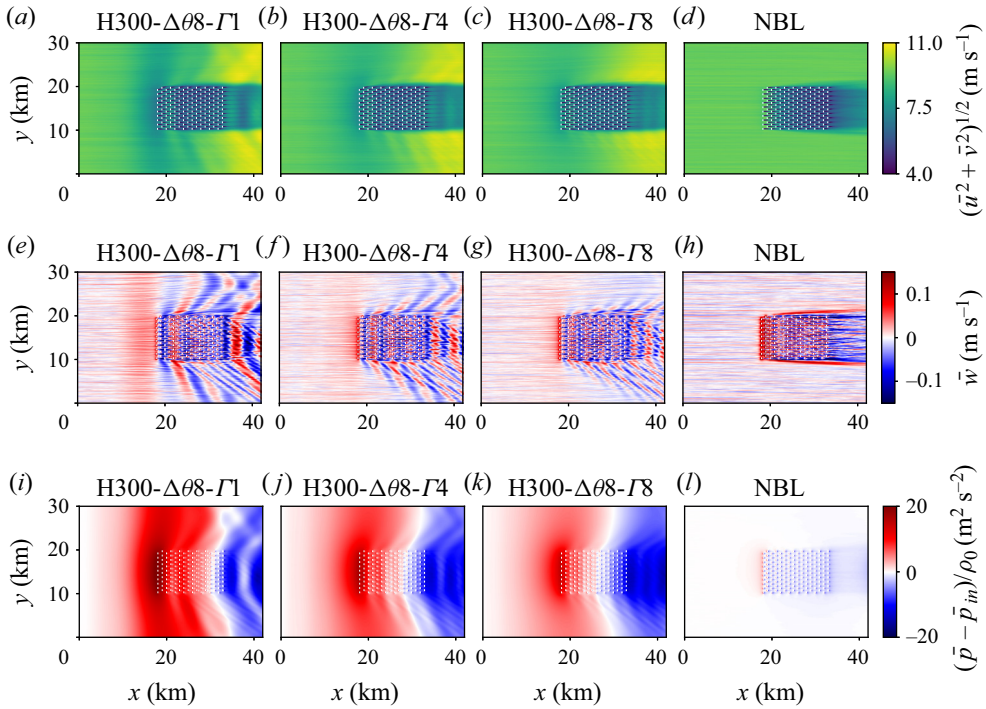


Figure 11. Contours of the time-averaged (a–d) velocity magnitude, (e–h) vertical velocity and (i–l) pressure perturbation in an  $x$ – $y$  plane taken at turbine hub height for cases (a,e,i) H300- $\Delta\theta$ 8- $\Gamma$ 1, (b,f,j) H300- $\Delta\theta$ 8- $\Gamma$ 4, (c,g,k) H300- $\Delta\theta$ 8- $\Gamma$ 8 and (d,h,l) the NBL reference case. The location of the turbine rotor disks is indicated with vertical white lines. The NBL reference case refers to simulation H500- $\Delta\theta$ 0- $\Gamma$ 0.

mentioned earlier, the pressure perturbations are at least one order of magnitude lower than in cases with thermal stratification above the ABL. This explains the absence of velocity reductions several kilometres upstream of the farm together with a monotonic decrease in velocity magnitude between the first- and last-row turbines.

We now turn our attention to the effects of changes in the free-atmosphere lapse rate. Equation (4.1) shows that the interfacial-wave horizontal wavelength is negatively correlated with the Brunt–Väisälä frequency. This means that an increase in free-atmosphere stability results in a lower  $\lambda_x$  value. Figure 11 clearly illustrates this behaviour. As  $\Gamma$  increases, air parcels find more resistance in displacements along the vertical direction due to the stronger buoyant forces. Therefore, a stronger free-lapse rate damps waves along the inversion layer, limiting its vertical displacement. Consequently, a lower cold anomaly is generated, which leads to lower pressure perturbations. This is visible when comparing figure 11(i,k), which shows  $x$ – $y$  planes of pressure perturbations at turbine hub height obtained with  $\Gamma = 1 \text{ K km}^{-1}$  and  $\Gamma = 8 \text{ K km}^{-1}$ , respectively, while keeping all other parameters constant. This also implies that the hydrostatic flow-blockage effect reduces as the stability of the free atmosphere increases in the presence of a strong capping-inversion strength, as shown in figure 11(a–c). This result is in contrast with findings of Abkar & Porté-Agel (2013) and Wu & Porté-Agel (2017), who observed that changing the free-lapse rate from  $1 \text{ K km}^{-1}$  to  $10 \text{ K km}^{-1}$  caused a power drop of about 35%. However, in their study, they were at the same time varying the capping-inversion height and strength, which explains this difference in power output. Finally, figure 11(e–g) shows the vertical velocity fields, where the V-shape pattern at the farm sides together with



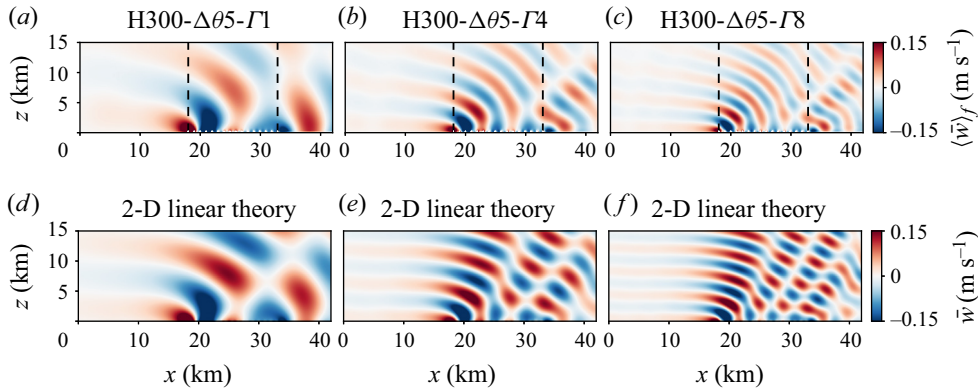


Figure 12. Contours of the time-averaged vertical velocity field in an  $x$ - $z$  plane further averaged along the farm width for cases (a) H300- $\Delta\theta 5$ - $\Gamma 1$ , (b) H300- $\Delta\theta 5$ - $\Gamma 4$  and (c) H300- $\Delta\theta 5$ - $\Gamma 8$ . (d-f) Vertical velocity field obtained with the two-dimensional gravity-wave linear-theory model described in Appendix C. For instance, the internal waves in panel (d) are excited by an obstacle with shape given by the capping-inversion vertical displacement obtained in case H300- $\Delta\theta 5$ - $\Gamma 1$ . The vertical black dashed lines in panel (a-c) denote the location of the first- and last-row turbines while the location of the turbine rotor disks in panels (a-c) are indicated with vertical white lines.

interfacial-wave effects are clearly visible. Interestingly, we also observe slanted lines at the left side of the farm with an angle of  $29^\circ$  with respect to the streamwise direction. We note that this effect is related to the perturbation introduced by the single turbines and will be further discussed in § 4.3. For the sake of comparison, we report again the results obtained for the NBL reference case in figure 11(d,h,l).

### 4.3. Comparison between LES results and gravity-wave linear-theory models

The simplicity of gravity-wave linear-theory models contributed to their spread in analysing mountain-wave phenomena. A wide variety of this type of model can be found in Gill (1982), Nappo (2002), Lin (2007), Sutherland (2010) and Teixeira (2014). More recently, the same theory has been applied to wind-farm studies, since the latter can be considered as a ‘permeable mountain’. Examples of these models can be found in Smith (2010), Allaerts & Meyers (2018), Allaerts & Meyers (2019), Devesse *et al.* (2022) and Smith (2022, 2023). In the current section, we perform a comparison of our results against some of the simplest wind-farm gravity-wave linear-theory models.

Figure 12 compares the internal gravity-wave pattern obtained in three LES against the results obtained with a simple two-dimensional gravity-wave linear-theory model (Nappo 2002). The latter is a quasi-analytical model that takes as an input the shape of the obstacle, assumed impermeable. The obstacle shape also provides the bottom boundary conditions to the system of equations. In the current study, the inversion-layer displacement shown in figure 15(a-d) defines the obstacle shape. For the sake of clearness, we briefly explain this linear model in Appendix C. We remark the excellent agreement between our results and linear theory, particularly in terms of gravity-wave phase line and vertical wavelength. Moreover, the slanted region tilted downstream of zero vertical velocity that forms near the trailing edge of the farm is captured by both models. This supports the idea that this phenomenon is not a manifestation of internal gravity-wave reflection but is rather due to the interaction between two out-of-phase trains of internal waves triggered by the first- and last-row turbines; see figure 4. We believe that this good comparison is mostly a result of the effort spent in properly developing and calibrating the buffer regions in the main

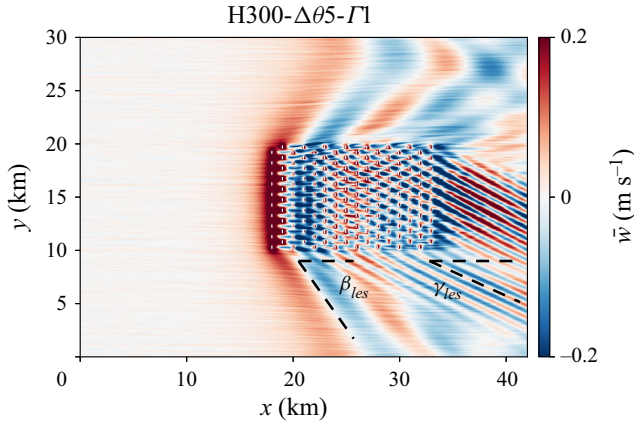


Figure 13. Contours of the time-averaged vertical velocity field in an  $x$ - $y$  plane taken at turbine-tip height for case H300- $\Delta\theta$ 5- $\Gamma$ 1. The definition of the farm V-shape angle  $\beta_{les}$  together with the angle that the slanted lines make with the horizontal  $\gamma_{les}$  are reported in the figure. The location of the turbine rotor disks is indicated with vertical white lines.

domain. We note that a discussion on the internal gravity-wave reflectivity is reported in [Appendix D](#).

Next, [figure 13](#) displays a  $x$ - $y$  plane of the time-averaged vertical velocity field taken at turbine-tip height for case H300- $\Delta\theta$ 5- $\Gamma$ 1. The flow deceleration causes a strong upward motion in the proximity of the first rows of turbines, which results in interfacial waves along the capping inversion. The upward and downward motion that these waves generate is very visible in [figure 13](#), both in and around the farm.

Two additional distinct phenomena take place. First, we observe a V-shape pattern around the farm that has already been observed and investigated by [Allaerts & Meyers \(2019\)](#). They reported that the angle of the pair of characteristic lines that gives rise to this pattern is only dependent on the Froude number and is given by

$$\beta_{lin} = \arctan \left( \left( Fr^2 - 1 \right)^{-1/2} \right), \quad (4.2)$$

where the Froude number is defined as a ratio between a boundary-layer velocity scale (i.e.  $U_B$ ) and the interfacial-wave phase speed. In shallow-water wave theory, the phase speed is given by  $\sqrt{g'H}$  ([Acheson 1990](#); [Sutherland 2010](#)). This theory holds under the assumption that  $L > 4\pi H$ , where  $L$  denotes the length scale of the forcing. If we use the distance between first- and last-row turbines as a length scale (i.e.  $L = L_x^f$ ), this relation holds and the Froude number is therefore defined as  $Fr = U_B / \sqrt{g'H}$  ([Smith 2010](#); [Allaerts & Meyers 2019](#)). For instance, the Froude number is 1.29 for the case shown in [figure 13](#), which results in  $\beta_{lin} = 50.8^\circ$ . This value is in excellent agreement with that observed in the LES results, which measures  $\beta_{les} = 51^\circ$ . Equation (4.2) shows that the angle is well defined only for supercritical flows. In subcritical cases the characteristic lines become imaginary and no V-shape pattern occurs around the farm ([Allaerts & Meyers 2019](#)). The second pattern observed in [figure 13](#) is a set of slanted lines, and is related to the perturbation introduced by the turbine spacing. In fact, if we use as a length scale the equivalent turbine spacing  $S_e = D\sqrt{s_x s_y}$ , then we should define the interfacial-wave phase speed using deep-water wave theory, which holds when  $L < H/\pi$ . We note that the streamwise or spanwise spacings could also be a candidate for the length-scale definition.

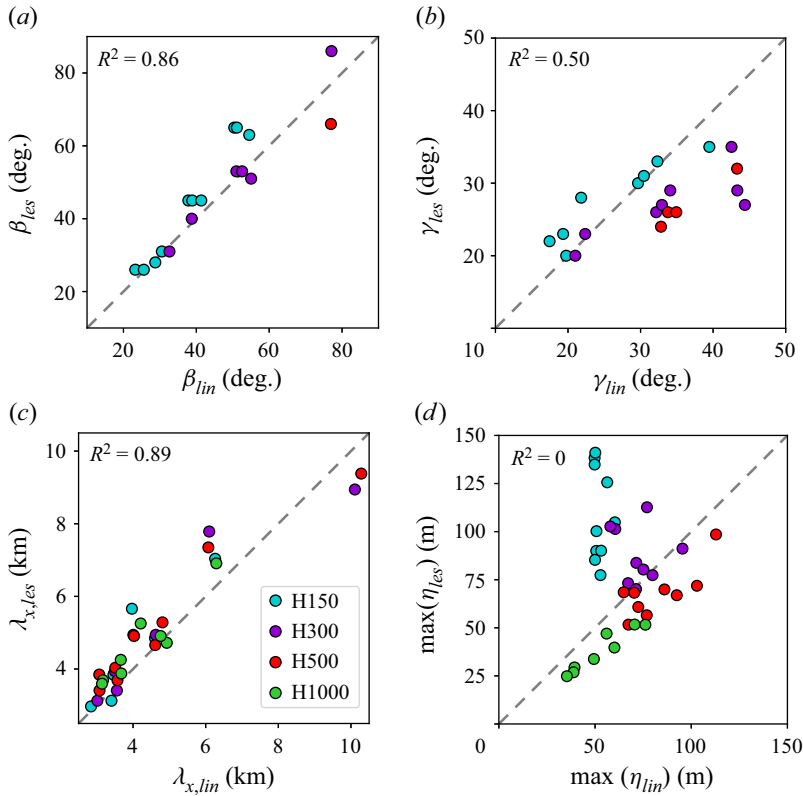


Figure 14. (a,b) Comparison of the  $\beta$  and  $\gamma$  angles measured in the LES results against the values predicted by linear theory (Allaerts & Meyers 2019). (c) Comparison of trapped-wave horizontal wavelength between LES results and the linear-theory model of Vosper (2004) and Sachsperger *et al.* (2015) (i.e. (4.1)). (d) Comparison of maximum inversion-layer vertical displacement between the LES results and the one-dimensional linear model developed by Allaerts & Meyers (2018). The  $R^2$  value denotes the coefficient of determination.

However, we cannot make such distinction as  $S_e = S_x = S_y$  in our work. Using this theory, the Froude number is defined as

$$Fr_{dw} = \frac{U_B}{\sqrt{\frac{g'S_e}{2\pi} \tanh\left(\frac{2\pi H}{S_e}\right)}}, \quad (4.3)$$

where the denominator represents the interfacial-wave phase speed. This Froude number measures 1.88 for case H300- $\Delta\theta 5$ - $\Gamma 1$ . Using (4.2), this results in an angle of  $32.1^\circ$ , which we denote with  $\gamma_{lin}$ . Also, this angle is in good agreement with that observed in the LES results, which measures  $\gamma_{les} = 28^\circ$ . We note that the lines that make the angles  $\beta_{les}$  and  $\gamma_{les}$  with the horizontal are also reported in figure 13. While the angle is explained by (4.2), we also see in figure 13 that these slanted lines only propagate along the left side of the farm. We speculate that this is due to the asymmetry generated by the Coriolis force.

The angles  $\beta_{les}$  and  $\gamma_{les}$  are measured by carefully aligning a slanted line to the pattern observed in the vertical velocity field, as shown in figure 13. A comparison between the  $\beta_{lin}$  and  $\beta_{les}$  angles for supercritical flows is shown in figure 14(a). Overall, we observe an excellent agreement, with values collapsing along the diagonal and a coefficient of determination of 0.86. Next, figure 14(b) compares the angle formed by the slanted lines

triggered by the turbine spacing. We see again a good agreement, with  $\gamma_{les}$  slightly lower than  $\gamma_{lin}$  in deeper boundary layers. Finally, [figure 14\(c\)](#) shows a comparison between the interfacial-wave horizontal wavelength obtained in LES against that evaluated with linear theory, i.e. using [\(4.1\)](#). For this case, the coefficient of determination measures 0.89, indicating a very strong correlation and, therefore, good agreement between linear theory and LES results.

Allaerts & Meyers (2018) derived a linear one-dimensional model for the capping-inversion vertical displacement in response to a drag force imposed within the whole ABL. The governing equation reads as

$$\left(1 - \frac{1}{Fr^2}\right) \frac{\partial \eta}{\partial x} = c_t \Pi(x) - 2(c_t \Pi(x) + c_d) \frac{\eta}{H} - \frac{1}{P_N} \mathcal{G}_N(\eta), \quad (4.4)$$

where  $\Pi(x)$  denotes a step function with support going from the start to the end of the farm and  $c_d = u_* / U_B$  represents the friction with the ground. Moreover, the thrust force imposed on the flow scales linearly with  $c_t$ , which is defined as

$$c_t = \frac{1}{2} \frac{\pi C_T}{4s_x s_y} \eta_w \gamma_v \quad (4.5)$$

with  $\gamma_v = U_{B,r}^2 / U_B^2$  a wind-profile shape factor, where  $U_{B,r}^2$  denotes the velocity in the streamwise direction obtained in the precursor simulation averaged over the full streamwise and spanwise directions and along the turbine rotor height. Moreover,  $\eta_w$  denotes the wake efficiency, which is later defined in [\(4.7a,b\)](#). Finally,  $\mathcal{G}_N(\eta)$  is a linear operator that accounts for internal-wave effects and is expressed as

$$\mathcal{G}_N(\eta) = \frac{1}{2\pi} \int |k| \left( \int \eta(x') e^{-ikx'} dx' \right) e^{ikx} dk. \quad (4.6)$$

We refer to Appendix 2 in Allaerts & Meyers (2018) for a full derivation of [\(4.4\)](#). Given the atmospheric state, [\(4.4\)](#) predicts the capping-inversion displacement along the streamwise direction. Furthermore, we name the maximum inversion-layer vertical displacement obtained with [\(4.4\)](#) and with the LES results as  $\max(\eta_{lin})$  and  $\max(\eta_{les})$ , respectively. These two quantities are displayed in [figure 14\(d\)](#), which shows a good match except for cases H150, for which  $\max(\eta_{lin}) < \max(\eta_{les})$ . The coefficient of determination is zero in this case, as this metric is very sensitive to outliers. We note that the values of  $\eta_w$ ,  $\beta_{les}$ ,  $\gamma_{les}$ ,  $\lambda_{x,les}$  and  $\max(\eta_{les})$  for all cases are summarized in [table 2](#).

In this section we have seen that our results match well when compared against various gravity-wave linear-theory models found in the literature. This further confirms that the LES results are not distorted by the domain boundaries and provide an interesting benchmark for the development, validation and calibration of existing and future low- and medium-fidelity wind-farm models.

#### 4.4. Comparison of flow profiles

We now investigate and compare flow profiles among all cases. Results are reported in [figure 15](#), which displays time-averaged flow profiles as a function of the streamwise direction. We start the analysis with [figure 15\(a–d\)](#) that displays the streamwise variation of vertical inversion-layer displacement, here denoted with  $\eta$ , further averaged along the farm width. For the CNBL cases,  $\eta$  is defined as the difference between the capping-inversion top evaluated in precursor and main domains using the Rampanelli & Zardi (2004) model. It is interesting to see that in the presence of thermal stratification

LES of wind farms operating in CNBLs

Cases	$\beta_{les}$ (°)	$\gamma_{les}$ (°)	$\lambda_{x,les}$ (km)	$\max(\eta_{les})$ (m)	$r$ (%)	$\eta_{int}$ (%)	$\eta_w$ (%)	$\eta_f$ (%)	$P_{1/\rho_0}$ (MWm <sup>3</sup> kg <sup>-1</sup> )	$P_{\infty/\rho_0}$ (MWm <sup>3</sup> kg <sup>-1</sup> )	$\Delta p_u$ (m <sup>2</sup> s <sup>-2</sup> )	$\Delta p_f$ (m <sup>2</sup> s <sup>-2</sup> )
H150-Δθ2-Γ1	26	22	—	138.3	2.57	90	46	41	7.06	7.84	7.53	6.01
H150-Δθ2-Γ4	26	23	—	134.9	0.89	80	52	42	6.30	7.84	9.81	11.12
H150-Δθ2-Γ8	28	28	—	141.0	0.58	75	57	43	5.87	7.84	11.26	14.59
H150-Δθ5-Γ1	45	30	7.03	100.2	4.61	70	50	35	5.47	7.84	11.81	10.07
H150-Δθ5-Γ4	45	31	4.85	90.0	1.78	61	62	37	4.78	7.84	14.37	15.93
H150-Δθ5-Γ8	45	33	3.13	85.4	1.12	57	68	39	4.50	7.84	15.32	19.02
H150-Δθ8-Γ1	65	35	5.66	125.6	8.06	26	123	32	2.08	7.84	24.13	23.17
H150-Δθ8-Γ4	65	—	3.85	90.1	2.59	36	98	36	2.85	7.84	21.70	24.09
H150-Δθ8-Γ8	63	—	2.97	77.4	1.58	42	89	37	3.29	7.84	20.01	24.97
H300-Δθ2-Γ1	31	20	—	104.8	3.33	86	50	43	6.85	8.00	8.06	6.72
H300-Δθ2-Γ4	31	20	—	101.4	0.82	78	58	45	6.25	8.00	9.90	11.78
H300-Δθ2-Γ8	—	23	—	102.7	0.49	75	62	47	6.02	8.00	10.63	14.58
H300-Δθ5-Γ1	53	26	7.79	112.6	7.56	58	71	41	4.62	8.00	15.31	15.09
H300-Δθ5-Γ4	53	27	4.94	83.8	1.92	61	74	45	4.86	8.00	14.93	18.28
H300-Δθ5-Γ8	51	29	3.41	73.2	1.13	64	74	47	5.11	8.00	14.02	19.47
H300-Δθ8-Γ1	86	35	4.94	91.2	7.17	44	100	44	3.50	8.00	21.70	25.54
H300-Δθ8-Γ4	—	29	3.94	77.4	3.75	53	89	47	4.21	8.00	17.97	24.69
H300-Δθ8-Γ8	—	27	3.13	70.1	2.84	58	83	48	4.66	8.00	15.81	24.23

Table 2. For caption see next page.

Cases	$\beta_{les}$ (°)	$\gamma_{les}$ (°)	$\lambda_{x,les}$ (km)	$\max(\eta_{les})$ (m)	$r$ (%)	$\eta_{nl}$ (%)	$\eta_w$ (%)	$\eta_f$ (%)	$P_1/\rho_0$ (MWm <sup>3</sup> kg <sup>-1</sup> )	$P_\infty/\rho_0$ (MWm <sup>3</sup> kg <sup>-1</sup> )	$\Delta P_u$ (m <sup>2</sup> s <sup>-2</sup> )	$\Delta P_f$ (m <sup>2</sup> s <sup>-2</sup> )
H500- $\Delta\theta 2$ - $\Gamma 1$	40	—	8.94	80.3	3.39	82	54	45	6.49	7.90	8.19	8.25
H500- $\Delta\theta 2$ - $\Gamma 4$	—	—	5.28	68.2	0.72	79	60	47	6.28	7.90	9.00	12.09
H500- $\Delta\theta 2$ - $\Gamma 8$	—	—	3.85	68.5	0.41	79	62	49	6.27	7.90	8.89	13.55
H500- $\Delta\theta 5$ - $\Gamma 1$	66	24	7.35	98.5	7.77	59	78	46	4.67	7.90	15.00	18.59
H500- $\Delta\theta 5$ - $\Gamma 4$	62	26	4.66	69.9	2.26	70	71	50	5.51	7.90	11.80	17.44
H500- $\Delta\theta 5$ - $\Gamma 8$	—	26	3.69	60.8	0.97	74	69	51	5.86	7.90	10.37	17.19
H500- $\Delta\theta 8$ - $\Gamma 1$	70	32	4.91	66.9	8.75	64	82	53	5.05	7.90	13.54	22.62
H500- $\Delta\theta 8$ - $\Gamma 4$	70	—	4.03	56.5	5.49	72	75	53	5.66	7.90	11.41	21.17
H500- $\Delta\theta 8$ - $\Gamma 8$	—	—	3.41	51.6	4.98	74	72	54	5.87	7.90	10.17	19.44
H1000- $\Delta\theta 2$ - $\Gamma 1$	—	—	9.38	71.8	3.20	83	56	47	6.34	7.62	7.44	9.36
H1000- $\Delta\theta 2$ - $\Gamma 4$	—	—	4.72	51.7	0.63	88	56	49	6.70	7.62	6.64	10.35
H1000- $\Delta\theta 2$ - $\Gamma 8$	—	—	3.69	47.0	0.55	88	57	50	6.70	7.62	6.12	10.46
H1000- $\Delta\theta 5$ - $\Gamma 1$	—	—	6.91	51.6	11.54	83	62	51	6.30	7.62	7.28	13.33
H1000- $\Delta\theta 5$ - $\Gamma 4$	—	—	4.91	39.7	3.53	87	59	51	6.61	7.62	6.57	12.15
H1000- $\Delta\theta 5$ - $\Gamma 8$	—	—	3.88	33.7	0.77	90	57	52	6.83	7.62	6.08	11.69
H1000- $\Delta\theta 8$ - $\Gamma 1$	—	—	5.25	29.4	15.82	89	60	53	6.75	7.62	5.79	12.59
H1000- $\Delta\theta 8$ - $\Gamma 4$	—	—	4.25	26.9	8.87	90	58	53	6.89	7.62	5.73	12.54
H1000- $\Delta\theta 8$ - $\Gamma 8$	—	—	3.60	24.8	5.96	91	57	52	6.93	7.62	5.58	11.76
NBL	—	—	—	—	—	98	48	47	7.74	7.90	4.63	4.85

Table 2. Overview of the simulation results including the farm V-shape angle  $\beta_{les}$ , the slanted lines angle  $\gamma_{les}$ , the trapped-wave horizontal wavelength  $\lambda_{x,les}$ , the maximum inversion-layer vertical displacement  $\max(\eta_{les})$ , the reflectivity  $r$ , the non-local efficiency  $\eta_{nl}$ , the wake efficiency  $\eta_w$ , the farm efficiency  $\eta_f$ , the first-row turbine power output and the power output of a turbine operating in isolation normalized with a reference air density  $P_1/\rho_0$  and  $P_\infty/\rho_0$ , respectively, and the unfavourable and favourable pressure gradients magnitude  $\Delta P_u$  and  $\Delta P_f$ , respectively. We remark that the NBL reference case refers to simulation H500- $\Delta\theta 0$ - $\Gamma 0$ .

LES of wind farms operating in CNBLs

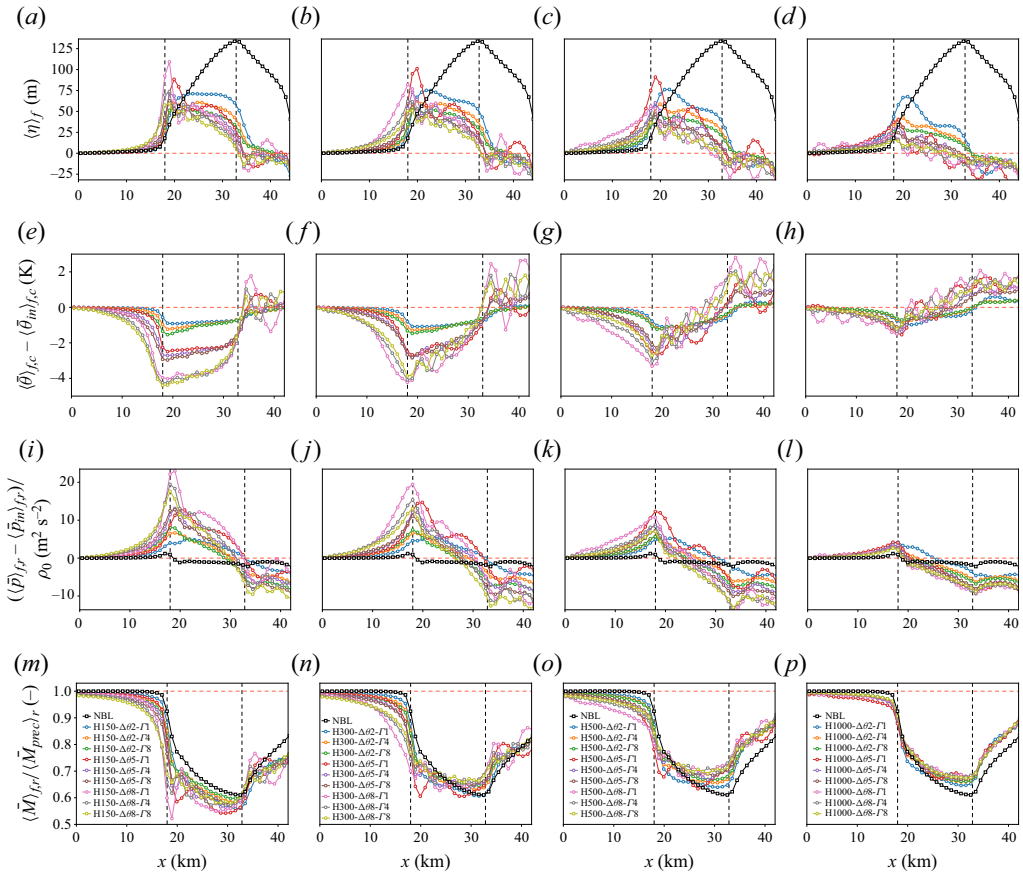


Figure 15. Time-averaged (*a–d*) capping-inversion displacement, (*e–h*) potential-temperature perturbation, (*i–l*) pressure perturbation and (*m–p*) horizontal velocity magnitude averaged over the farm width as a function of the streamwise direction. The potential-temperature perturbation is further averaged over the capping-inversion thickness, while the other quantities are averaged over the turbine rotor height. Moreover, the cases are organized per capping-inversion height. The vertical dashed black lines denote the location of the first- and last-row turbines.

above the ABL, the flow reacts to the presence of the farm several kilometres upstream. Cases with a weak inversion layer show higher displacements, independently from the inversion-layer height. This is due to the weak resistance to vertical motion that air parcels have in such cases. As  $\Delta\theta$  increases, interfacial waves with a lower wavelength get excited within the farm and in its wake. As noted previously, a stronger free atmosphere limits the displacement of the inversion layer, particularly within the first couple of turbine rows. Overall, shallow boundary layers tend to show higher inversion-layer vertical displacements than deeper ones. Moreover,  $\eta$  sharply decreases downwind of the last row of turbines in all cases, as a response to the flow acceleration in the wind-farm wake. In the NBL reference case, the absence of thermal stratification above the ABL allows for higher growth of the boundary layer. In this case,  $\eta$ , which is computed as a streamline, shows a monotonic growth across the farm, with a maximum displacement obtained at the last-row turbine location.

Perturbations in the potential-temperature field are shown in figure 15(*e–f*), averaged within the capping-inversion height and along the farm width. As  $H$  increases, the

cold anomaly reduces in magnitude. For instance, the minimum negative temperature perturbation is  $-1.4$  K for the H1000 cases, while it attains a value of  $-4.6$  K in the H150 cases. Even when the inversion-layer displacement is limited by high  $\Delta\theta$  values, the strong inversion that characterizes such cases generates higher temperature differences, which translate into stronger pressure perturbations. The latter are shown in [figure 15\(i–l\)](#), averaged along the farm width and within the turbine rotor height. Here, we observe that the cases with strong unfavourable and favourable pressure gradients are those with a strong inversion layer. For instance, the counteracting pressure gradient in case H300- $\Delta\theta 8$ - $\Gamma 1$  is 4.4 times that obtained in case H300- $\Delta\theta 2$ - $\Gamma 1$ . Pressure feedbacks in the neutral reference case are negligible when compared with those obtained in the CNBL cases. For instance, case H300- $\Delta\theta 5$ - $\Gamma 4$ , which [figure 2](#) defines as a highly probable atmospheric state over the North Sea, has a 14 times stronger unfavourable pressure gradient than the NBL reference case. However, we should note that all stratified cases are also characterized by a favourable pressure gradient through the farm, while the NBL reference case does not show this feature.

The pressure-perturbation effects on the velocity magnitude are evident in [figure 15\(m–p\)](#). The NBL reference case shows a reduction in wind speed only several rotor diameters upstream of the farm. Consequently, the velocity at the first-row turbine location is always higher than in the cases with thermal stratification above the ABL. Interestingly, the vertical motion generated by the interfacial waves at the capping-inversion height has direct consequences in terms of velocity magnitude at the turbine hub height, where significant oscillation in velocity magnitude within the farm and in its wake are observed for cases with a strong capping inversion. For instance, the velocity magnitude at the fourth-row turbine location is 5 % higher than that measured at the farm leading edge for case H300- $\Delta\theta 8$ - $\Gamma 1$ . As  $H$  increases, the flow response becomes less sensitive to changes in  $\Delta\theta$  and  $\Gamma$ . In fact, as the inversion-layer height approaches the equilibrium height of the TNBL, its effects on the farm–ABL interactions become smaller. Consequently, the velocity profiles and pressure perturbation of the CNBL cases get closer to those of the NBL reference case, as shown in [figure 15\(l, p\)](#). We remark that a stronger blockage effect and velocity deficits in shallow boundary layers have been observed also in SCADA data from the Nordsee Ost and Amrumbank West wind farms located in the German Bight area (Cañadillas *et al.* 2023) and in a previous study (Allaerts & Meyers 2017).

Cases H500- $\Delta\theta 8$ - $\Gamma 4$ , H1000- $\Delta\theta 8$ - $\Gamma 1$  and H1000- $\Delta\theta 8$ - $\Gamma 4$  in particular show oscillations in the capping-inversion displacement and temperature perturbation already in the farm induction region. Most likely, these are spurious effects introduced by the fringe region. In fact, Lanzilao & Meyers (2023b) have shown that their wave-free fringe-region technique can still introduce some perturbations in the domain of interest for a combination of low  $Fr$  and  $P_N$  numbers, which characterize these three cases; see [table 1](#).

Finally, [figure 16](#) focuses on the pressure build-up measured at the first-row turbine location along the spanwise direction. Here, the inverse relationship between capping-inversion height and counteracting pressure gradient is evident. Moreover, a deep boundary layer makes the simulation quasi-independent of changes in  $\Delta\theta$  and  $\Gamma$ , as all profiles collapse in [figure 16\(d\)](#). However, the pressure build-up in all CNBL cases still remains higher than that attained in the NBL reference case. [Figure 16](#) also shows that turbines situated in the centre of the farm experience a higher counteracting pressure gradient than those located at the farm sides. The asymmetry of the profiles with respect to the domain centreline is caused by the presence of the Ekman layer.



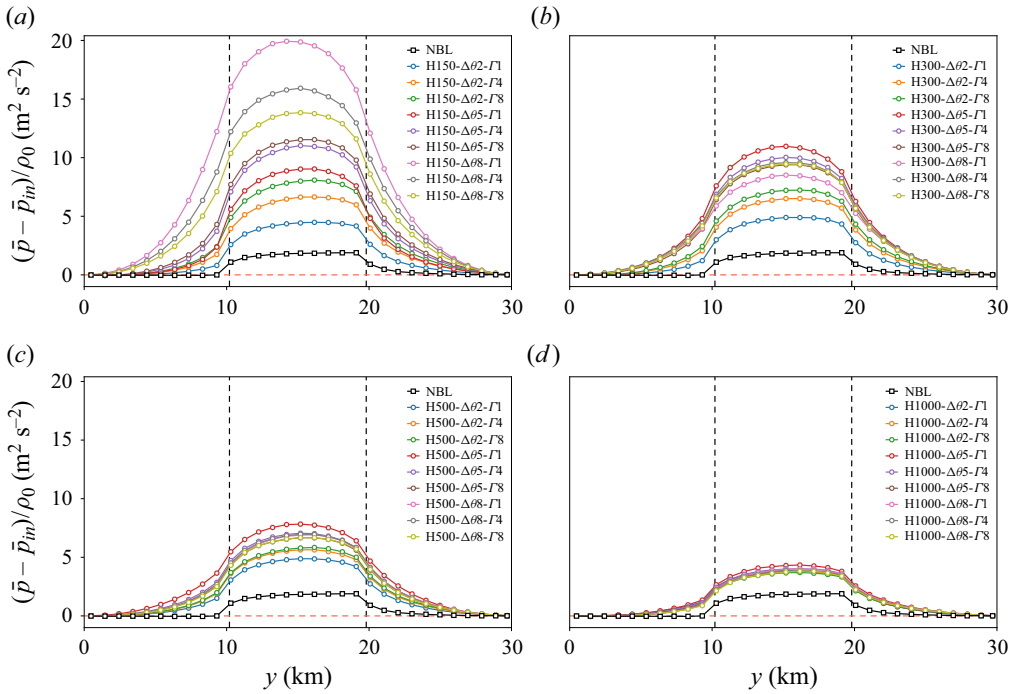


Figure 16. Pressure perturbation as a function of the domain width taken at  $x = 18$  km (i.e. the location of the first-row turbines) and further averaged over the turbine rotor height for cases (a) H150, (b) H300, (c) H500 and (d) H1000. The vertical dashed black lines denote the location of the first- and last-column turbines.

#### 4.5. Wind-farm power production

The time- and row-averaged turbine power output normalized with the first-row turbine power is displayed in figure 17 organized per capping-inversion strength, showing that cases with equal  $\Delta\theta$  have similar trends. Figure 17(a) shows that cases with weak capping-inversion height have similar power output per turbine row. The farm has a staggered layout, therefore, the high-speed channels that form between the turbines in the first row allow for a slightly higher power generation at the second row (McTavish *et al.* 2015; Meyer Forsting, Troldborg & Gaunaa 2017). After a drop of about 50% between the second and third row, the power remains approximately constant, with a minor increase towards the farm trailing edge for the cases with thermal stratification above the ABL. As the inversion-layer strength increases, power fluctuations are observed within the farm. These are mostly caused by the vertical motion generated by interfacial waves. Consequently, the power does not show a monotonic trend across the farm. Instead, the fifth row often extracts more power than the third row when  $\Delta\theta = 5$  K, with differences up to 40%. A more extreme behaviour is observed in figure 17(c), where in three cases a waked row extracts more power than the first row. Moreover, the strong favourable pressure gradient that develops across the farm in cases with a strong inversion layer also leads to an increase in power production towards the end of the farm. This phenomenon is accentuated in shallow boundary layers. For instance, the difference in power output between first- and last-row turbines is only about 8% in case H300- $\Delta\theta$ 8- $\Gamma$ 4, while the last-row turbines produce 23% more power than the first row in case H150- $\Delta\theta$ 8- $\Gamma$ 1.

Figure 17(d–e) shows the same results but normalized with  $P_\infty$ , that is, the power output of a turbine operating in isolation. In the CNBL cases, the ratio  $P_1/P_\infty$  (i.e. the

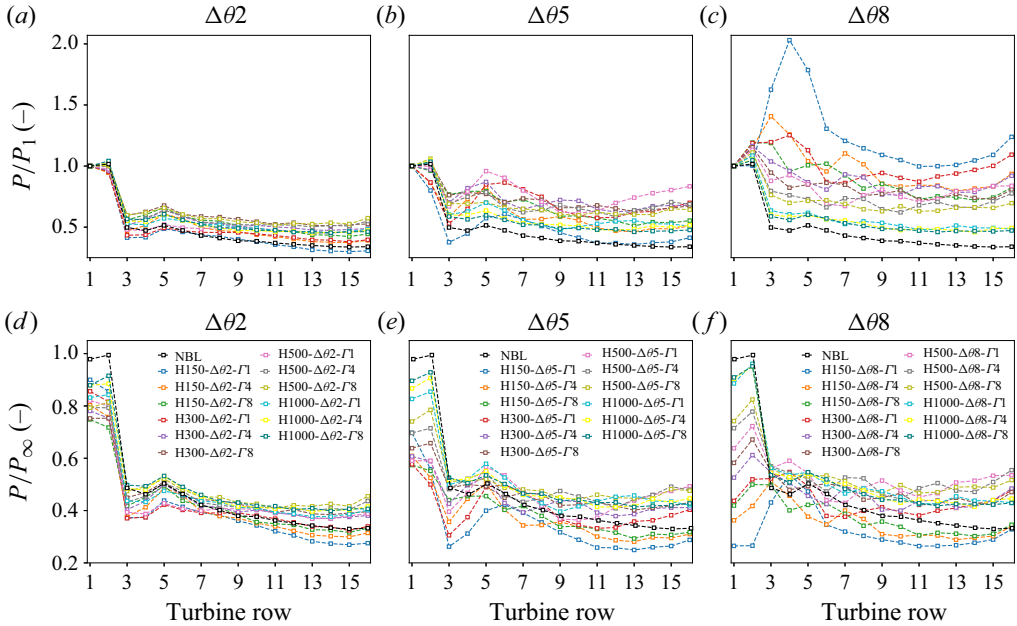


Figure 17. Averaged power output per turbine row normalized by (a–c)  $P_1$  of the respective simulation and (d–f)  $P_\infty$  of the respective inversion-layer height obtained with a capping-inversion strength of (a,d)  $\Delta\theta = 2$  K, (b,e)  $\Delta\theta = 5$  K and (c,f)  $\Delta\theta = 8$  K under different inversion-layer heights and free-atmosphere lapse rates. Here,  $P_1$  denotes the averaged power outputs of first-row turbines while  $P_\infty$  represents the power output of a turbine operating in isolation obtained with the single-turbine simulations – see [Appendix B](#).

non-local efficiency) is always much lower than 1, with a minimum of 0.26 attained in case H150- $\Delta\theta 8$ - $\Gamma 1$ . Moreover, the flow-blockage effect is much more sensitive to the inversion-layer height in the presence of strong capping inversion, as shown in [figure 17\(f\)](#). In the neutral reference case,  $P_1/P_\infty \approx 1$ . Once more, this suggests that the flow deceleration in the farm induction region is mostly related to atmospheric gravity waves. Moreover, the power output keeps decreasing towards the farm trailing edge in the NBL reference case, while a power increase is observed for the majority of the CNBL cases. This is due to the favourable pressure gradient acting as an energy source across the farm. We note that the value of  $P_1$  and  $P_\infty$  for all cases are summarized in [table 2](#).

#### 4.6. Wind-farm efficiencies

We now turn our attention to the wind-farm efficiency. Similarly to [Allaerts & Meyers \(2018\)](#), we define the farm efficiency as  $\eta_f = \eta_w \eta_{nl}$ , with

$$\eta_w = \frac{P_{tot}}{N_t P_1}, \quad \eta_{nl} = \frac{P_1}{P_\infty} \tag{4.7a,b}$$

where  $\eta_w$  and  $\eta_{nl}$  denote the wake and non-local efficiency, respectively. Moreover,  $N_t$  indicates the number of turbines,  $P_{tot}$  the total farm power,  $P_1$  the averaged power output of first-row turbines while  $P_\infty$  represents the power output of a turbine operating in isolation. The latter is evaluated using the single-turbine simulations discussed in [Appendix B](#).

The various efficiencies are illustrated in [figure 18](#) for all cases, with values also reported in [table 2](#). [Figure 18\(a\)](#) shows that the strong counteracting pressure gradient that characterizes shallow boundary layers causes  $\eta_{nl}$  to be lower in the H150 cases than

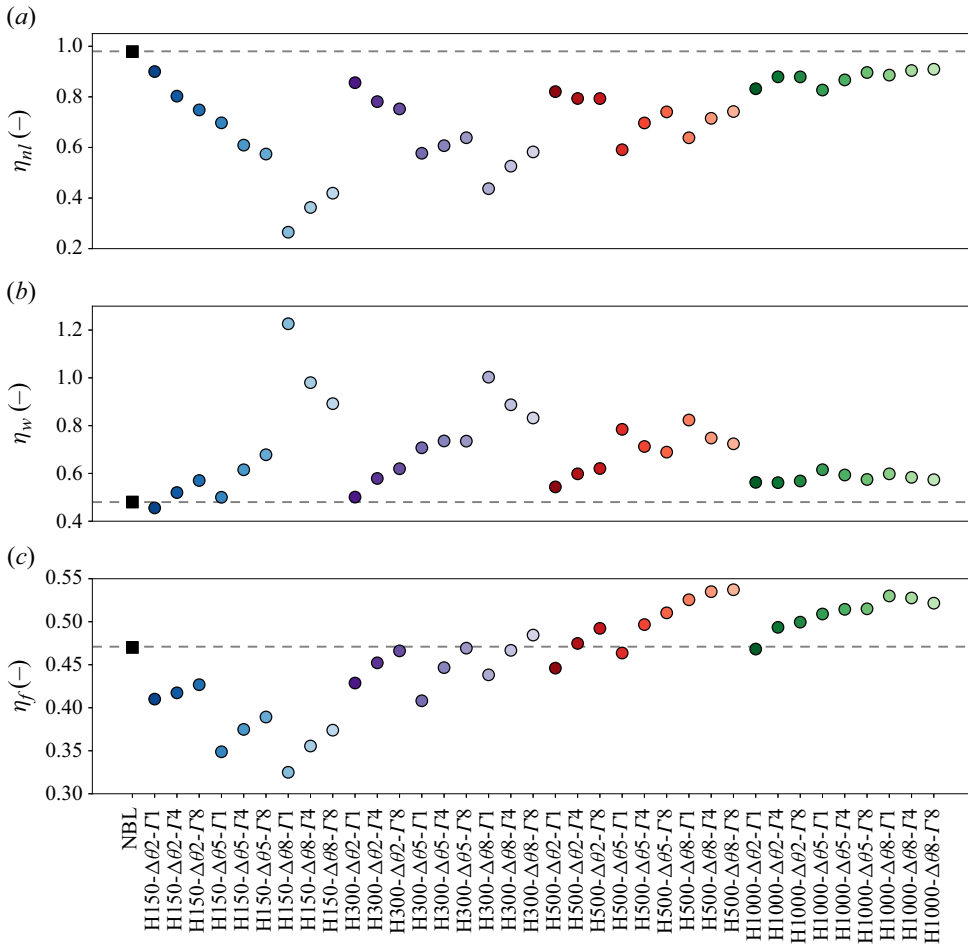


Figure 18. (a) Non-local, (b) wake and (c) farm efficiency as a function of all simulation cases. The cases with thermal stratification above the ABL are represented by a circle while the NBL reference case is marked with a square. The horizontal grey dashed line indicates the relative efficiency value obtained in the NBL reference case.

in the H1000 cases. The highest non-local efficiency is attained in the NBL reference case, showing that the cumulative turbine induction has a minor contribution to the flow-blockage effect for this case. The wake efficiency is shown in figure 18(b). As hypothesized by Allaerts & Meyers (2018), a low non-local efficiency leads to a higher wake efficiency. In fact, the accumulation of potential energy caused by the flow slow down in front of the farm is converted back into kinetic energy that accelerates the flow across the farm (Allaerts & Meyers 2018). This negative correlation is clearly visible when comparing results in figure 18(a,b). We note that case H150- $\Delta\theta 8$ -I1 has a wake efficiency greater than 1. For this atmospheric condition, the average power generated by the waked rows is higher than that extracted by first-row turbines. The absence of favourable pressure gradients across the farm causes the wake efficiency of the NBL reference case to be among the lowest. Finally, figure 18(c) displays the overall farm efficiency. The farm efficiency in the H150 and H300 cases is lower than the NBL reference case. For the H500 and H1000 cases, the farm efficiency becomes higher than the NBL reference

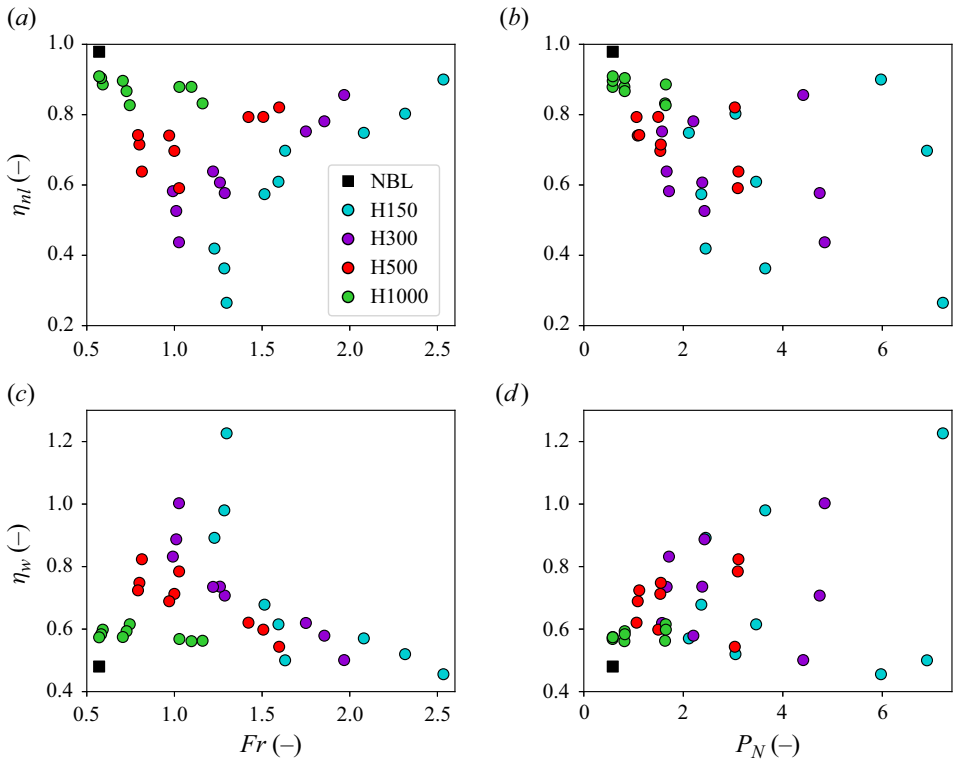


Figure 19. (a,b) Non-local and (c,d) wake efficiency as a function of the (a,c)  $Fr$  and (b,d)  $P_N$  numbers.

value. This further highlights the strong influence that the capping-inversion height has on the wind-farm power output. Moreover, we observe that the farm efficiency is positively related with  $\Gamma$  in the majority of the cases. We note that the error bars representing the 95 % confidence interval computed with the moving block bootstrapping method for all efficiencies are in the order of  $\pm 1\%$  and for this reason are not shown in [figure 18](#).

Next, we investigate how the non-local and wake efficiencies scale with the atmospheric state. In a first attempt, we plot the efficiencies against the  $Fr$  and  $P_N$  numbers, which are the two non-dimensional groups that govern gravity-wave effects. Results are shown in [figure 19](#). The lowest values of non-local efficiency are attained for  $Fr \approx 1.3$ . [Figure 19\(b\)](#) shows that, in general, the non-local efficiency decreases as  $P_N$  increases. The wake efficiency shown in [figure 19\(c,d\)](#) shows an opposite trend, as expected. Overall, values remain scattered along the parameter space and strong trends are not observed.

In the previous sections we have seen that gravity-wave induced pressure gradients play a primary role in the flow dynamics. Therefore, in a second attempt, we try to scale the farm efficiencies against these pressure feedbacks. In particular, we define  $\Delta p_u = (\langle \bar{p} \rangle_{f,r}(x_{ft}) - \langle \bar{p} \rangle_{f,r}(x_{in})) / \rho_0$  and  $\Delta p_f = (\langle \bar{p} \rangle_{f,r}(x_{lt}) - \langle \bar{p} \rangle_{f,r}(x_{ft})) / \rho_0$ , where  $x_{in} = 0$  km represents the main domain inflow. Moreover,  $x_{ft} = 18$  km and  $x_{lt} = 32.85$  km denote the location of the first- and last-row turbines, respectively. Given this definition,  $\Delta p_u$  and  $\Delta p_f$  quantify the pressure feedback upstream and across the farm, respectively. [Figure 20\(a\)](#) shows the non-local efficiency as a function of  $\Delta p_u$  normalized by the geostrophic wind. Here, we can observe a very strong negative correlation, with coefficient of determination close to unity. This is expected since the non-local efficiency quantifies the flow slow down in front of the farm, which depends on the magnitude

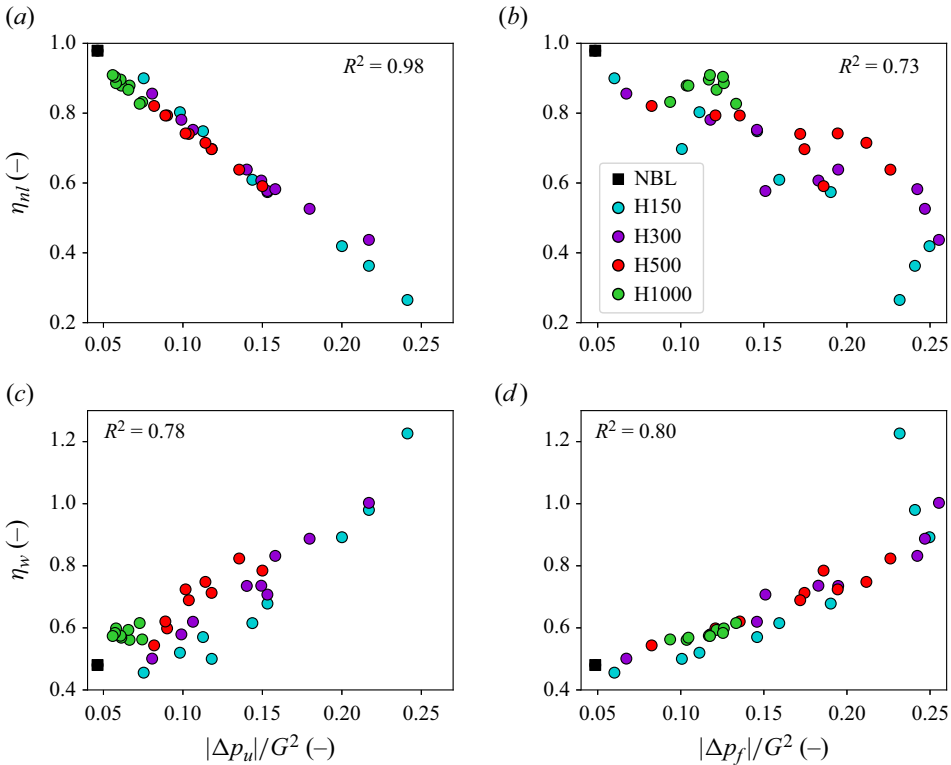


Figure 20. (a,b) Non-local and (c,d) wake efficiency as a function of the (a,c) unfavourable and (b,d) favourable pressure gradients magnitude normalized by the geostrophic wind. The  $R^2$  value denotes the coefficient of determination.

of the unfavourable pressure gradient. An opposite trend is visible in figure 20(d), where the wake efficiency shows a strong positive correlation with  $\Delta p_f$ , confirming the role of the favourable pressure gradient in accelerating the wake recovery mechanism. High coefficients of determination are also observed in figure 20(b,c), as a consequence of the natural correlation between unfavourable and favourable pressure gradients. The latter is shown in figure 21. Both the favourable and unfavourable pressure gradient magnitude decrease as the capping-inversion height increases, with the lowest value attained in the NBL reference case (see also table 2). Moreover,  $\Delta p_f$  is higher than  $\Delta p_u$  in the majority of the cases.

In light of these results, we believe that finding a good scaling parameter for  $p$  would also result in a scaling parameter for the efficiencies. Pressure perturbations induced by gravity waves scale with the capping-inversion vertical displacement  $\eta$ . In fact, Smith (2010) has shown that in Fourier domain

$$\frac{\hat{p}}{\rho_0} = \left( g \frac{\Delta\theta}{\theta_0} + \frac{i(N^2 - \Omega^2)}{m} \right) \hat{\eta} \quad (4.8)$$

with  $m$  the vertical wavenumber and  $\Omega$  the intrinsic wave frequency. After assuming a hydrostatic free atmosphere and ignoring variation along the spanwise direction (i.e. a

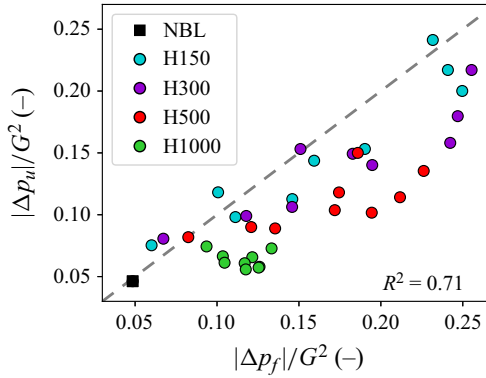


Figure 21. Unfavourable pressure gradient magnitude as a function of the favourable pressure gradient magnitude normalized by the geostrophic wind. The  $R^2$  value denotes the coefficient of determination.

one-dimensional model), (4.8) can be written as

$$\frac{\hat{p}}{\rho_0} = \frac{U_B^2}{H} \left( Fr^{-2} + iP_N^{-1} \right) \hat{\eta}. \tag{4.9}$$

A simple model that provides an estimate for  $\eta$  as a function of the atmospheric state has been proposed by Allaerts & Meyers (2018) and is reported in (4.4). In the Fourier domain, this model reads as

$$\left( 1 - Fr^{-2} \right) ik\hat{\eta} = c_t \hat{\Pi} - \frac{2c_t}{H} \hat{\Pi} * \hat{\eta} - 2c_d \frac{\hat{\eta}}{H} - P_N^{-1} |k| \hat{\eta}, \tag{4.10}$$

where the operator  $*$  denotes a convolution. The second and third terms on the right-hand side of (4.10) represent a second-order term and the friction with the ground normalized with  $H$ , respectively, which are much smaller than the other terms. After neglecting these two terms, we can write

$$\hat{\eta} = \frac{c_t}{k} \left( P_N^{-1} \frac{|k|}{k} + i \left( 1 - Fr^{-2} \right) \right)^{-1} \hat{\Pi}. \tag{4.11}$$

By substituting (4.11) into (4.9), we obtain

$$\frac{1}{\rho_0} \frac{H}{U_B^2} \frac{k}{c_t} \frac{\hat{p}}{\hat{\Pi}} = \left( Fr^{-2} + iP_N^{-1} \right) \left( P_N^{-1} \frac{|k|}{k} + i \left( 1 - Fr^{-2} \right) \right)^{-1}. \tag{4.12}$$

Using the dominant wavelength  $k_d = 2\pi/L_x^f$  in the streamwise direction, we define the non-dimensional group

$$F_p \triangleq \frac{8s_x s_y H k_d}{\rho_0 U_{B,r}^2 \pi C_T \eta_w \|\hat{\Pi}(k_d)\|} \|\hat{p}(k_d)\| = \sqrt{\frac{Fr^{-4} + P_N^{-2}}{(1 - Fr^{-2})^2 + P_N^{-2}}}, \tag{4.13}$$

where  $\|\hat{\Pi}(k_d)\|$ ,  $k_d$ ,  $s_x$ ,  $s_y$  and  $C_T$  are constant values since we do not vary the farm layout and the turbines thrust coefficient. Following the results discussed previously, we have

$$1 - \eta_{nl} \propto \frac{1}{\rho_0} \frac{\Delta p_u}{G^2} \propto \frac{L_x^f}{G^2} \frac{1}{\rho_0} \|\hat{p}(k_d)\| \propto \eta_w \frac{L_x^f}{H} \frac{U_{B,r}^2}{G^2} F_p \tag{4.14}$$

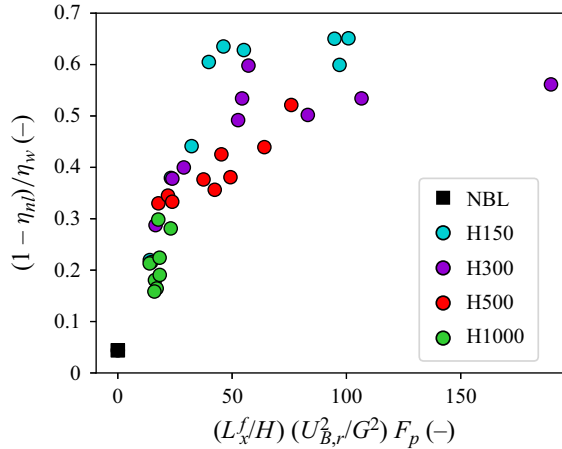


Figure 22. Ratio between the non-local and wake efficiency as a function of the  $F_p$  number.

implying that

$$\frac{1 - \eta_{nl}}{\eta_w} \propto \frac{L_x^f}{H} \frac{U_{B,r}^2}{G^2} F_p. \quad (4.15)$$

Figure 22 confirms this result, showing a relatively good scaling.

## 5. Conclusions

This study set out to analyse the flow response to wind-farm forcing under atmospheres with different thermal stratification above the ABL. To this end, we performed 40 LES of a  $14.85 \times 9.4 \text{ km}^2$  wind farm. The simulations were carried out with SP-Wind, an LES solver developed at KU Leuven. The main domain was driven by turbulent fully developed statistically steady flow fields obtained in precursor simulations. Moreover, the solver periodicity in the streamwise direction was broken using a wave-free fringe-region technique while at the top of the domain an RDL was placed to damp gravity waves. Special effort in tuning the buffer regions was spent in order to minimize gravity-wave reflectivity and correctly impose the inflow conditions.

We investigated the effect of changes in the capping-inversion height and strength, as well as free-atmosphere lapse rate, on the flow behaviour in and around the farm. In all cases, the flow convergence caused by the farm drag force displaces the capping inversion upward, creating a cold anomaly that induces pressure perturbations. We found very strong velocity deficits in shallow boundary layers, caused by the limited flow mixing and energy entrainment due to the close proximity of the inversion layer to the turbine-tip height. In turn, this resulted in higher inversion-layer vertical displacement and stronger cold anomalies. Therefore, shallow boundary-layer flows are characterized by a very strong counteracting pressure gradient in the farm induction region, further amplified by the presence of a strong inversion layer. Deeper boundary layers can accommodate the IBL growth, limiting flow redirection at the farm sides together with the vertical displacement of the capping inversion. Therefore, the counteracting pressure feedback has a lower magnitude in such cases. The pressure build-up in the farm entrance region is then released as a form of kinetic energy throughout the farm, which accelerates the wake recovery mechanism. This effect is more pronounced in shallow boundary layers.

In regard to changes in  $\Delta\theta$ , we found that a stronger capping inversion reduces its vertical displacement, therefore increasing the flow rate at the farm sides. Moreover, inversion layers with higher strengths support interfacial waves with lower horizontal wavelengths. Finally, we noticed that a stronger free-atmosphere lapse rate limits air-parcel vertical motion, therefore reducing the magnitude of both the counteracting and favourable pressure gradients. We remark that the pressure perturbations in the NBL reference case were at least one order of magnitude lower than those in the CNBL cases.

The turbine power generation per row was also investigated. We observed that the flow divergence–convergence generated by interfacial waves causes considerable power fluctuations within the farm. Moreover, the turbine power tends to increase towards the farm trailing edge, particularly in cases with a shallow boundary layer and a high capping-inversion strength.

A non-local efficiency of 98 % was observed for the NBL reference case. In contrast, the non-local efficiency attained values as low as 26 % in the presence of thermal stratification above the ABL. Among cases with a stratified atmosphere, the non-local efficiency varied between 26 % and 91 %, suggesting that flow blockage is primarily related to atmospheric gravity waves. Moreover, we noticed that the non-local and wake efficiencies are inversely related. The farm efficiency in the H150 and H300 cases was lower than the NBL reference case, while it became higher for the H500 and H1000 cases. We also observed that the farm efficiency is positively related with  $\Gamma$ . In fact, a free atmosphere with strong stratification leads to a higher wind-farm power output than a weakly stratified atmosphere, for a fixed  $H$  and  $\Delta\theta$  value. These observations suggested that the shape of the vertical potential-temperature profile has a significant impact on the wind-farm performance. Finally, we found no simple scaling between the efficiencies and the  $Fr$  and  $P_N$  numbers. Instead, a very good scaling was found with the pressure gradients. This observation allowed us to derive a new scaling parameter  $F_p$  for the ratio of non-local to wake efficiencies.

Thereafter, we compared our results against various one- and two-dimensional gravity-wave linear-theory models. Here, we noticed an excellent agreement between the internal gravity-wave pattern and magnitude, underlining the importance of properly calibrating the fringe region and RDL. Moreover, the LES results were in line with linear theory also in terms of interfacial-wave horizontal wavelength and maximum inversion-layer vertical displacement.

Finally, the sensitivity study to the domain size conducted in [Appendix A](#) has shown that the wind-farm performance is quasi-independent of the induction-region length when using the wave-free fringe-region technique. In fact, by varying the fetch between the main domain inflow and the first-row turbine from 10 km to 50 km, the non-local and wake efficiency only varied by about 1 percentage point, independently from the capping-inversion height. However, we observed more pronounced differences in the flow behaviour as the domain width was increased. For instance, the non-local efficiency obtained in a domain with a ratio  $L_y/L_y^f$  of 6.38 is 1.12 times that measured in a domain with  $L_y/L_y^f = 2.13$  for a shallow boundary layer. Besides enhancing the flow-blockage effect, a domain with a low  $L_y/L_y^f$  ratio also increases the channelling effect at the farm sides. Therefore, we concluded that it is necessary to have a domain with a  $L_y/L_y^f$  ratio of at least 6 when simulating wind-farm operations in shallow boundary-layer flows. Deeper boundary-layer flows are less sensitive to the domain width, but still require a wider space at the farm sides than simulations with a neutral atmosphere.



The good agreement between gravity-wave linear-theory models and LES results and their consistency with previous findings entails that the numerical results are not distorted by the domain boundaries, and result in a valid benchmark for the development, validation and calibration of existing and future low- and medium-fidelity wind-farm models. In the future we plan to extend the database to baroclinic atmospheres, where the geostrophic wind varies with height. Moreover, the presence of multiple capping inversions is also of interest. The farm geometry was kept constant in the current study, but we are aware that it can have significant effects on the flow behaviour. Therefore, pressure feedbacks under various farm layouts and densities will be investigated. Furthermore, an analysis on the wave drag (Teixeira 2014) and its relation with the energy radiated outward (i.e. away from the farm) could be of use to further explore the effects of gravity waves on the mean flow in and around the farm. Finally, we plan to study wind-farm operation in weak and strong SBLs, which are known to enhance the flow-blockage effect.

**Acknowledgements.** The authors thank Koen Devesse for useful discussions and Steven Vandenbrande for HPC technical support.

**Funding.** The authors acknowledge support from the Research Foundation Flanders (FWO, grant no. G0B1518N), from the project FREEWIND, funded by the Energy Transition Fund of the Belgian Federal Public Service for Economy, SMEs, and Energy (FOD Economie, K.M.O., Middenstand en Energie) and from the European Union Horizon Europe Framework programme (HORIZON-CL5-2021-D3-03-04) under grant agreement no. 101084205. The computational resources and services in this work were provided by the VSC (Flemish Supercomputer Center), funded by the Research Foundation Flanders (FWO) and the Flemish Government department EWI.

**Declaration of interests.** The authors report no conflict of interest.

**Data availability statement.** The full dataset underlying the analysis in the current article, including, e.g. turbine statistics, three-dimensional mean flow fields of first-, second- and third-order statistics of precursor and main domain, as well as some post-processing example scripts are available open source as a KU Leuven RDR dataset: <https://doi.org/10.48804/L45LTT> (Lanzilao & Meyers 2023a).

#### **Author ORCIDs.**

 L. Lanzilao <https://orcid.org/0000-0003-1976-3449>;

 J. Meyers <https://orcid.org/0000-0002-2828-4397>.

**Author contributions.** L.L. and J.M. jointly set up the simulation studies and wrote the manuscript. L.L. performed code implementations and carried out the simulations. J.M. supervised the research and was responsible for acquisition of funding.

## **Appendix A. Sensitivity of wind-farm performance to the domain length and width**

The numerical domain should be wide enough to limit artificial sidewise blockage. The latter occurs when the lateral boundaries are too close to the farm. Moreover, enough streamwise distance should be present upwind of the farm, to properly account for the flow deceleration due to the wind-farm blockage effect. Similarly, the fringe region should be located far enough from the last-turbine row to avoid spurious effects on the flow development in proximity to the farm. In the presence of neutral atmospheres, these numerical artefacts have a very limited impact on the farm performance. In fact, the absence of thermal stratification above the ABL reduces the wind-farm footprint, allowing for a smaller numerical domain. However, the effects of the domain boundaries can significantly alter the wind-farm performance when thermal stratification above the ABL is considered. To date, there are no guidelines on how to select the domain length and width when performing wind-farm simulations in CNBLs. The goal of this appendix is to define such criteria.

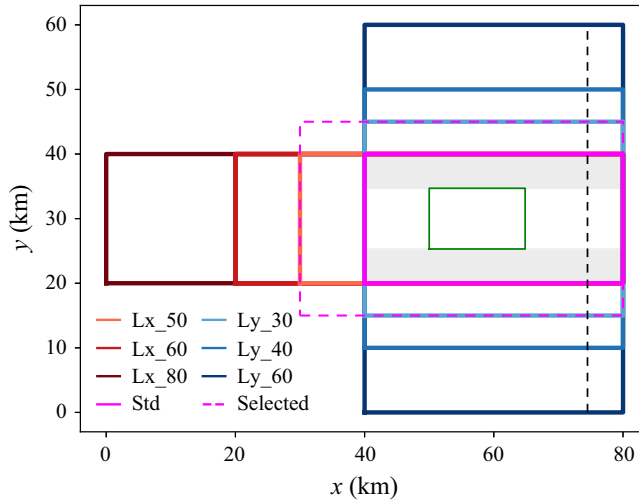


Figure 23. Sketch of the numerical domain length and width adopted in the sensitivity study. The dashed pink rectangle denotes the domain selected for performing the sensitivity study to the atmospheric state. Moreover, the green rectangle represents the wind-farm dimension while the vertical dashed black line denotes the starting point of the fringe region. Finally, the grey shaded areas and the region in between them represent the areas over which spanwise averages are taken by the operator  $\langle \cdot \rangle_s$  and  $\langle \cdot \rangle_f$ , respectively.

Cases	$L_x$ (km)	$L_y$ (km)	$L_z$ (km)	$L_{ind}/L_x^f$ (-)	$L_y/L_y^f$ (-)	$N_x$ (-)	$N_y$ (-)	$N_z$ (-)	DOF (-)
Std	40	20	25	0.67	2.13	1280	920	490	$2.89 \times 10^9$
Lx-50	50	20	25	1.35	2.13	1600	920	490	$3.46 \times 10^9$
Lx-60	60	20	25	2.02	2.13	1920	920	490	$4.04 \times 10^9$
Lx-80	80	20	25	3.37	2.13	2560	920	490	$5.19 \times 10^9$
Ly-30	40	30	25	0.67	3.19	1280	1380	490	$4.33 \times 10^9$
Ly-40	40	40	25	0.67	4.26	1280	1840	490	$5.77 \times 10^9$
Ly-60	40	60	25	0.67	6.38	1280	2760	490	$8.66 \times 10^9$
Selected	50	30	25	1.21	3.19	1600	1380	490	$5.19 \times 10^9$

Table 3. Overview of the numerical domains used to perform the sensitivity study on the domain size. The parameters  $L_x$ ,  $L_y$  and  $L_z$  denote the streamwise, spanwise and vertical domain dimensions while  $N_x$ ,  $N_y$  and  $N_z$  denote the number of grid points used along the respective directions. Moreover,  $L_{ind}$  denotes the fetch of domain between the inflow and the first-row turbine location while  $L_x^f$  and  $L_y^f$  represent the wind-farm length and width, respectively. The last column reports the number of DOF comprehensive of both precursor and main domains. We note that each case is driven by three different CNBLs, that is H300- $\Delta\theta 5$ - $\Gamma 4$ , H500- $\Delta\theta 5$ - $\Gamma 4$  and H1000- $\Delta\theta 5$ - $\Gamma 4$ , for a total of 21 simulations. Finally, the last row reports the selected domain used to perform the sensitivity study to the atmospheric state.

To this end, we first fix a relatively small reference domain with  $L_x$  and  $L_y$  equal to 40 and 20 km, respectively, which correspond to a typical domain length and width used in previous studies (Allaerts & Meyers 2017, 2018; Lanzilao & Meyers 2022, 2023b). Thereafter, we first keep  $L_y$  constant and we vary  $L_x$  between 40 and 80 km, so that the fetch of the domain from the inflow to the first-row turbine location (i.e.  $L_{ind}$ ) varies between 10 and 50 km, respectively. This corresponds to a ratio  $L_{ind}/L_x^f$  of 0.67 and 3.37. Next, we keep  $L_x$  constant and we vary  $L_y$  between 20 and 60 km, so that the ratio  $L_y/L_y^f$  goes from 2.13 to 6.38, respectively. In total, we end up with seven domain

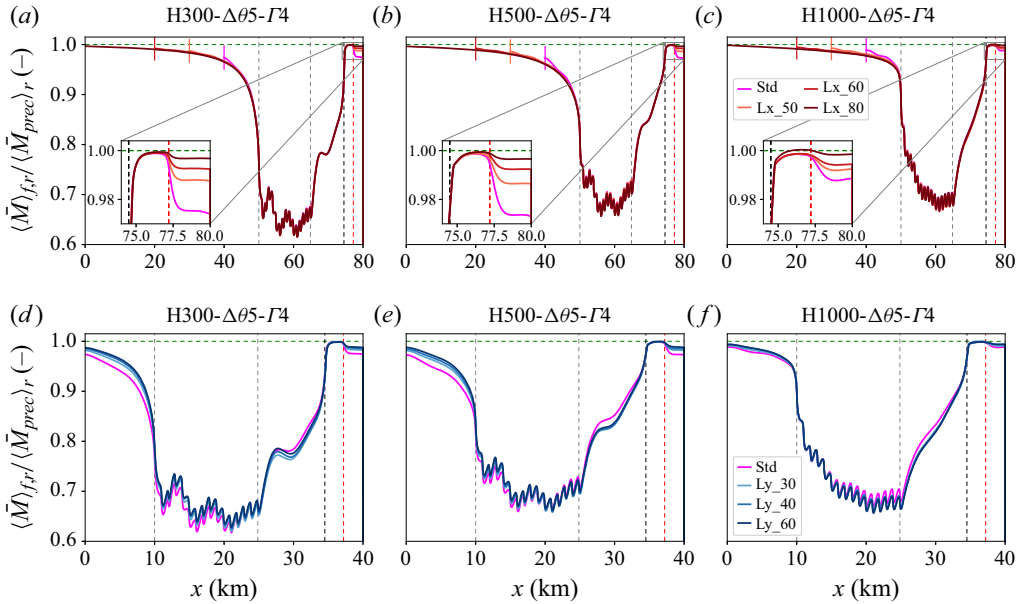


Figure 24. Time-averaged velocity magnitude  $M = (u^2 + v^2)^{1/2}$  averaged in the horizontal direction along the farm width and in height along the turbine rotor. We normalize the results with the velocity magnitude obtained in the precursor simulation and we plot it as a function of the streamwise direction. Results are shown for different (a–c) domain lengths and (d–f) domain widths. The simulations are driven by the cases (a,d) H300- $\Delta\theta$ 5- $\Gamma$ 4, (b,e) H500- $\Delta\theta$ 5- $\Gamma$ 4 and (c,f) H1000- $\Delta\theta$ 5- $\Gamma$ 4. The grey vertical dashed lines are positioned in correspondence of the first- and last-row turbines. Moreover, the black and red vertical dashed lines denote the starting and ending points of the fringe forcing. The fringe region extends to the domain end to account for the damping of the convective term. In the bottom left corner of panels (a–c), the flow behaviour within the fringe region is magnified. Finally, the vertical segments in panels (a–c) facilitate the identification of the starting points of the domains with smaller  $L_x$ .

configurations, which are illustrated in figure 23. We note that all simulations adopt a vertical domain height of 25 km and have the same grid resolution. Since we speculate that the domain size should scale with the height of the capping inversion, we drive these simulations with three different inflow profiles with equal  $\Delta\theta$  and  $\Gamma$  but different  $H$ , that is, H300- $\Delta\theta$ 5- $\Gamma$ 4, H500- $\Delta\theta$ 5- $\Gamma$ 4 and H1000- $\Delta\theta$ 5- $\Gamma$ 4, for a total of 21 simulations. The various cases analysed in this section are summarized in table 3.

Figure 24(a) shows the time-averaged velocity magnitude further averaged in the horizontal directions along the farm width and in height along the turbine rotor. We scale the plot with the velocity magnitude obtained in the precursor simulation. Here, the results refer to domains of different lengths driven by the H300- $\Delta\theta$ 5- $\Gamma$ 4 case. Interestingly, the large  $L_{ind}$  value in the Lx\_80 case allows us to observe that the flow begins to slow down several tens of kilometres upstream of the farm. Within the farm, the effect of turbines and wake mixing is clearly visible. In the last 5.5 km of the domain, the body force applied within the fringe region restores the inflow provided by the precursor simulation. Surprisingly, the solutions obtained on shorter domains follow the same trend and also have the same magnitude. In fact, the convective damping region within the fringe region seems to indirectly account for the additional flow slow down necessary to match the solution obtained on longer domains. Figure 24(b,c) shows that the same behaviour is attained for deeper boundary layers.

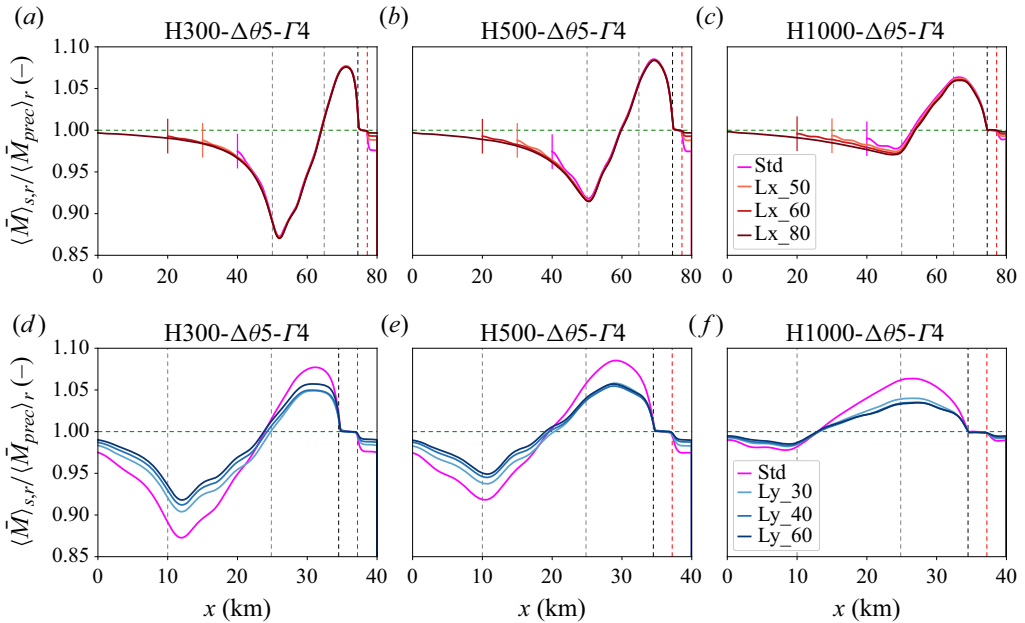


Figure 25. Time-averaged velocity magnitude  $M = (u^2 + v^2)^{1/2}$  averaged in the horizontal directions along the farm sides and in height along the turbine rotor. We normalize the results with the velocity magnitude obtained in the precursor simulation and we plot it as a function of the streamwise direction. Results are shown for different (a–c) domain lengths and (d–f) domain widths. The simulations are driven by the cases (a,d) H300- $\Delta\theta 5$ - $\Gamma 4$ , (b,e) H500- $\Delta\theta 5$ - $\Gamma 4$  and (c,f) H1000- $\Delta\theta 5$ - $\Gamma 4$ . The grey vertical dashed lines are positioned in correspondence of the first- and last-row turbines. Moreover, the black and red vertical dashed lines denote the starting and ending points of the fringe forcing. The fringe region extends to the domain end to account for the damping of the convective term. Finally, the vertical segments in panels (a–c) facilitate the identification of the starting points of the domains with smaller  $L_x$ .

The numerical solution is much more sensitive to the domain width. This is illustrated in figure 24(d), which shows the velocity magnitude obtained with domains of different widths driven by the H300- $\Delta\theta 5$ - $\Gamma 4$  case. Here, the solution obtained on the standard domain has a velocity that is 1.5% lower than case  $L_y$ \_60 at  $x = 0$  km. This additional slow down is purely artificial and comes from the fact that  $L_y/L_y^f$  measures only 2.12 in the standard domain. This is a result that we expected. In fact, as the ratio  $L_y/L_y^f \rightarrow 1$ , the farm layout tends to a semi-infinite farm, which is known to over-predict flow blockage; see Allaerts & Meyers (2017). The same difference reduces to 0.5% for the deep boundary-layer case; see figure 24(f). This is also expected since the influence of the inversion layer on the flow behaviour is inversely related to its height.

The results in terms of velocity magnitude averaged in the horizontal directions along the farm sides (i.e. the shaded areas in figure 23) and in height along the turbine rotor are shown in figure 25. Again, when varying  $L_x$ , all solutions collapse onto the one obtained with the standard domain. However, considerable differences are observed in figure 24(d–e), where we vary the domain width. In fact, the presence of the inversion layer limits the boundary-layer thickening, causing the flow to accelerate at the farm sides. A narrow domain artificially enhances this channelling effect of about 2% in terms of velocity magnitude. As the inversion-layer height increases, solutions on wider domains tend to collapse onto each other.

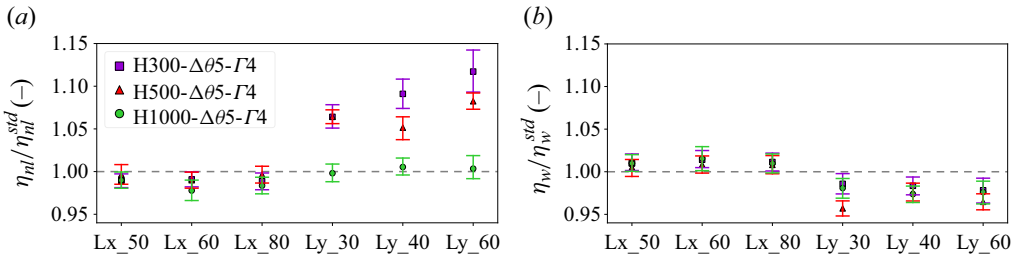


Figure 26. (a) Non-local and (b) wake efficiency normalized by the values obtained in the standard domain. The symbol denotes the time-averaged value while the error bars represent the 95 % confidence interval. The latter are computed using the moving block bootstrapping method developed by Beyaztas, Firuzan & Beyaztas (2017) and Boufidi, Lavagnoli & Fontaneto (2020), using the procedure described by Bon & Meyers (2022).

Finally, for a quantitative estimate of the influence of the domain length and width on wind-farm performance, we look at the farm efficiencies. Figure 26(a) shows that the time-averaged non-local efficiency normalized with the value obtained in the standard domain is quasi-independent on the distance between the first-row turbine and the main domain inflow, i.e. on the ratio  $L_{ind}/L_x^f$ . This is expected in light of the results shown in figure 24(a–c). However, considerable differences are observed when varying the domain width in shallow boundary layers. For instance, the time-averaged non-local efficiency obtained in case Ly\_60 driven by H300- $\Delta\theta_5$ - $\Gamma_4$  is 1.12 times higher than that measured in the standard domain. The wake efficiency, shown in figure 26(b), is less dependent on the numerical domain size and it shows a negative correlation with respect to  $\eta_{nl}$ .

In conclusion, the wind-farm performance is quasi-independent of the distance between the domain inflow and the first-row turbine location when using the wave-free fringe-region technique. However, a narrow domain artificially enhances flow blockage. Finally, we observe that the domain size should depend upon the inversion-layer height. In fact, shallower boundary layers require wider domains than deeper ones. This also implies that wind-farm–LES in CNBLs should adopt wider domains than simulations in neutral atmospheres. As a result of this study, we fix the main domain length and width to 50 and 30 km, respectively, with  $L_{ind} = 18$  km. A sketch of this domain is reported in figure 23. We remark that this choice is mainly dictated by the computational resources at our disposal. In fact, an even wider domain would have been relevant. Based on the current analysis, we conclude that we may overestimate the effect of blockage on farm efficiency with a factor of roughly 1.05 for  $H \leq 500$  m, while the effect of blockage is properly represented for the H1000 cases.

## Appendix B. Large-eddy simulation of a turbine operating in isolation

Single-turbine simulations are necessary to evaluate the power output of a turbine operating in isolation, which we define as  $P_\infty$ . In the farm, first-row turbines are affected by flow blockage, so that their power output is naturally lower than  $P_\infty$ . Moreover, figure 3 illustrates that the turbulent statistically steady velocity profiles obtained with the precursor simulations are independent of the capping-inversion strength and free-atmosphere lapse rate. They only differ as  $H$  varies. Therefore, we perform only four single-turbine simulations, one per each value of  $H$ .

The presence of a single turbine allows us to use a much smaller domain, with an equal length and width of 10 km. This size corresponds to that of the precursor domain. In the vertical direction, we keep  $L_z = 25$  km as in the wind-farm simulations. The horizontal

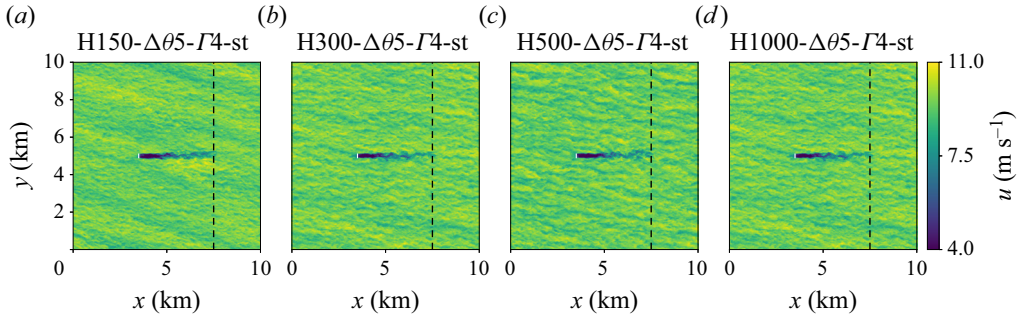


Figure 27. Contours of the instantaneous streamwise velocity field in an  $x$ - $y$  plane taken at turbine hub height for cases (a) H150- $\Delta\theta 5$ - $\Gamma 4$ -st, (b) H300- $\Delta\theta 5$ - $\Gamma 4$ -st, (c) H500- $\Delta\theta 5$ - $\Gamma 4$ -st and (d) H1000- $\Delta\theta 5$ - $\Gamma 4$ -st. The vertical black dashed line represents the start of the fringe region while the vertical white line denotes the turbine rotor disk location.

and vertical grid resolution also correspond to those adopted in the wind-farm simulations, meaning that we have 320, 460 and 490 points in the  $x$ ,  $y$  and  $z$  directions, respectively. The RDL and fringe region adopt the same set-up described in § 2.4. However, to account for the smaller domain, also the fringe-region length has been reduced to 2.5 km compared with the 5.5 km adopted for the wind-farm simulations. Finally, the time horizon for the wind-farm start-up phase has been set to 1 h. Afterwards, statistics are collected over a simulation time of 1.5 h.

Figure 27 illustrates instantaneous streamwise velocity fields in an  $x$ - $y$  plane taken at turbine hub height for the four single-turbine simulations. In all cases, we can easily distinguish the turbine wake, which recovers downwind before being fully replenished by the fringe-region body force, which restores the inflow conditions. Overall, we observe that the perturbations that the turbine induces on the flow are too small to excite any noticeable gravity-wave effects, such as flow blockage upstream and flow speed up at its side. Consequently, we believe that this set of simulations is suitable for providing an estimate for  $P_\infty$ . The free-stream power values are reported in table 2.

### Appendix C. A simple two-dimensional gravity-wave linear-theory model

We consider the Euler equations for irrotational, frictionless and adiabatic flow. Moreover, we neglect the Coriolis force and we assume that there is no variation in the  $y$  direction, so that the problem can be considered to be two dimensional. After manipulating the governing equations, the following solution in Fourier space for the streamwise and vertical velocity, pressure and potential temperature can be derived:

$$\hat{u}(k, z) = -iGm\hat{h}_o e^{imz}, \tag{C1}$$

$$\hat{w}(k, z) = iGk\hat{h}_o e^{imz}, \tag{C2}$$

$$\hat{p}(k, z) = iG^2 \rho_0 m \hat{h}_o e^{imz}, \tag{C3}$$

$$\hat{\theta}(k, z) = -\frac{N^2 \theta_0}{g} \hat{h}_o e^{imz}. \tag{C4}$$

Here the hat denotes a variable in the Fourier domain,  $k$  represents the streamwise wavenumbers while  $i$  is the imaginary unit. Moreover, the vertical wavenumber  $m$  depends

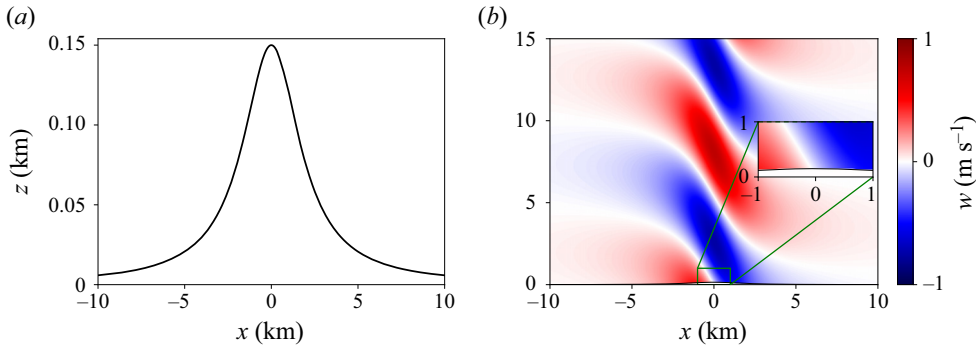


Figure 28. (a) Bell-shaped mountain known in the literature as the Witch of Agnesi. (b) Vertical velocity field predicted by the two-dimensional linear-theory model as a response to the obstacle shown in panel (a). In the centre right of panel (b), the solution in the region close to the obstacle is magnified.

upon  $k$ , which is assumed to be positive, and the atmospheric state, being defined as

$$m = \begin{cases} \sqrt{N^2/G^2 - k^2}, & N^2/G^2 > k^2, \\ i\sqrt{k^2 - N^2/G^2}, & N^2/G^2 < k^2, \end{cases} \quad (\text{C5})$$

where  $N$  is the Brunt–Väisälä frequency and  $G$  the geostrophic wind. We refer the reader to Nappo (2002), Lin (2007), Sutherland (2010) and Cushman-Roisin & Beckers (2011) for more details on the derivation of (C1)–(C4). The only input to the model consists of the obstacle shape in Fourier space, here denoted with  $\hat{h}_o$ . The latter is assumed impermeable. Moreover, it is assumed that the streamline slope equals the terrain slope locally. Finally, an inverse Fourier transform is necessary to express (C1)–(C4) in real space.

To conclude, we briefly show an example case. We consider a bell-shaped mountain, also known as the Witch of Agnesi. The latter is defined as

$$h_o(x) = \frac{h_m a^2}{x^2 + a^2}, \quad \hat{h}_o(k) = \frac{h_m a}{2} e^{-ka} \quad \text{for } k > 0, \quad (\text{C6})$$

where  $h_m = 0.15$  km is the mountain height while  $a = 2$  km denotes the mountain half-width. Moreover, we fix the geostrophic wind to  $10 \text{ m s}^{-1}$  and the free-atmosphere lapse rate to  $1 \text{ K km}^{-1}$ . Figure 28(a) shows the obstacle shape while the vertical velocity field is illustrated in figure 28(b), where internal waves triggered by the obstacle are clearly visible.

#### Appendix D. Internal gravity-wave reflectivity

In this appendix we investigate the performance of the RDL by analysing the internal gravity-wave reflectivity  $r = E_{\downarrow}/E_{\uparrow}$ , where  $E_{\downarrow}$  and  $E_{\uparrow}$  denote the vertical kinetic energy per unit mass (i.e.  $0.5w^2$ ) associated with upward and downward internal gravity waves. To compute  $r$ , we use the algorithm proposed by Taylor & Sarkar (2007) that makes use of the fact that the sign of the vertical phase velocity is opposite to the sign of the vertical group velocity for internal gravity waves. Moreover, similarly to Allaerts & Meyers (2017, 2018) and Lanzilao & Meyers (2023b), the upward and downward vertical kinetic energy are computed over a  $x$ – $z$  plane including the free atmosphere only (i.e. starting at a height of 1.5 km above the capping inversion) without the buffer regions.

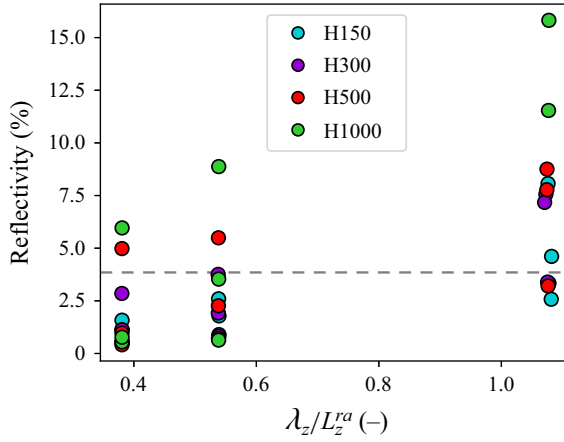


Figure 29. Reflectivity as a function of the ratio between the gravity-wave vertical wavelength and the RDL vertical extension.

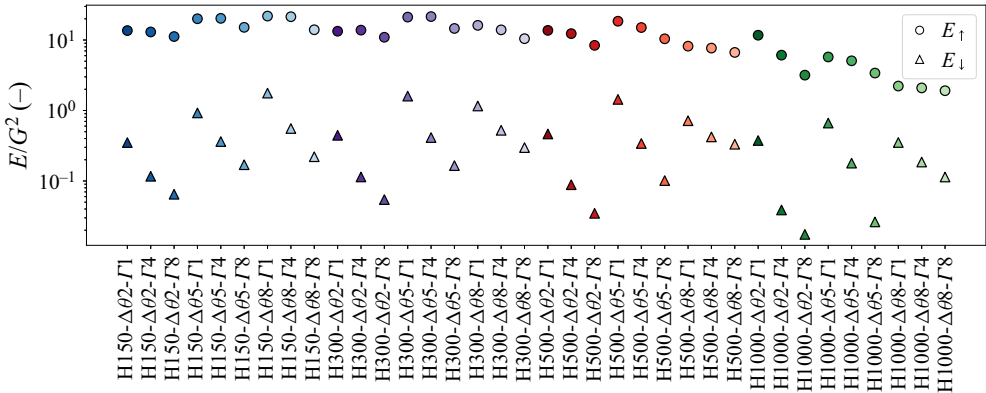


Figure 30. Vertical kinetic energy associated with upward ( $E_{\uparrow}$  – circle) and downward ( $E_{\downarrow}$  – triangle) internal waves scaled with the geostrophic wind.

Results are shown in [figure 29](#), which illustrates the reflectivity in percentage points as a function of the ratio  $\lambda_z/L_z^{ra}$ . The internal gravity-wave vertical wavelength only depends upon the Brunt–Väisälä frequency since the geostrophic wind is constant in our study. Therefore, the results are naturally divided into three groups defined by a free-atmosphere lapse rate of 1, 4 and 8 K km<sup>-1</sup>. For the RDL to be effective, Klemp & Lilly (1977) mentioned that  $L_z^{ra}$  should be at least one time the internal gravity-wave vertical wavelength. Therefore, it is no surprise to see on average higher values of reflectivity when  $\Gamma = 1$  K km<sup>-1</sup>, which corresponds to a ratio  $\lambda_z/L_z^{ra}$  of 1.08. As the stability of the free atmosphere increases, the ratio  $\lambda_z/L_z^{ra}$  reduces to 0.38, and so does the reflectivity. Overall,  $r$  spans from a minimum of 0.41 % to a maximum of 15.82 %, with an average value over all cases of 3.85 %. The NBL reference case does not support gravity waves, therefore, it is not included in the results. We note that the reflectivity values for all cases are summarized in [table 2](#).

Next, the vertical kinetic energy associated with upward and downward waves is shown in [figure 30](#). Overall,  $E_{\downarrow}$  is roughly an order of magnitude lower than  $E_{\uparrow}$ . Moreover, the highest values of  $E_{\downarrow}$  are always attained in weakly stratified atmospheres, i.e. when  $\Gamma =$



1 K km<sup>-1</sup>. This is expected since the RDL does not perform optimally in such a case. Finally, we note that  $E_{\uparrow}$  gradually reduces as  $H$  increases. This is related to the fact that the capping-inversion displacement diminishes with  $H$ , therefore inducing vertical motions with a lower magnitude in the free atmosphere.

REFERENCES

- ABKAR, M. & PORTÉ-AGEL, F. 2013 The effect of free-atmosphere stratification on boundary-layer flow and power output from very large wind farms. *Energies* **6**, 2338–2361.
- ACHESON, D.J. 1990 *Elementary Fluid Dynamics*. Oxford University Press.
- ALLAERTS, D. 2016 Large-eddy simulation of wind farms in conventionally neutral and stable atmospheric boundary layers. PhD thesis, KULeuven, Leuven, Belgium.
- ALLAERTS, D. & MEYERS, J. 2015 Large eddy simulation of a large wind-turbine array in a conventionally neutral atmospheric boundary layer. *Phys. Fluids* **27** (6), 065108.
- ALLAERTS, D. & MEYERS, J. 2017 Boundary-layer development and gravity waves in conventionally neutral wind farms. *J. Fluid Mech.* **814**, 95–130.
- ALLAERTS, D. & MEYERS, J. 2018 Gravity waves and wind-farm efficiency in neutral and stable conditions. *Boundary-Layer Meteorol.* **166**, 269–299.
- ALLAERTS, D. & MEYERS, J. 2019 Sensitivity and feedback of wind-farm induced gravity waves. *J. Fluid Mech.* **862**, 990–1028.
- ALLAERTS, D., VANDEN BROUCKE, S., VAN LIPZIG, N. & MEYERS, J. 2018 Annual impact of wind-farm gravity waves on the Belgian–Dutch offshore wind-farm cluster. *J. Phys.: Conf. Ser.* **1037**, 072006.
- ARCHER, C.L., MIRZAEISEFAT, S. & LEE, S. 2013 Quantifying the sensitivity of wind farm performance to array layout options using large-eddy simulation. *Geophys. Res. Lett.* **40** (18), 4963–4970.
- BARTHELMIE, R.J., *et al.* 2009 Modelling and measuring flow and wind turbine wakes in large wind farms offshore. *Wind Energy* **12**, 431–444.
- BEYAZTAS, B.H., FIRUZAN, E. & BEYAZTAS, U. 2017 New block bootstrap methods: sufficient and/or ordered. *Commun. Stat. Simulat.* **46** (5), 3942–3951.
- BLEEG, J. & MONTAVON, C. 2022 Blockage effects in a single row of wind turbines. *J. Phys.: Conf. Ser.* **2265** (2), 022001.
- BLEEG, J., PURCELL, M., RUISI, R. & TRAIGER, E. 2018 Wind farm blockage and the consequences of neglecting its impact on energy production. *Energies* **11**, 1609.
- BON, T. & MEYERS, J. 2022 Stable channel flow with spanwise heterogeneous surface temperature. *J. Fluid Mech.* **933**, A57.
- BORTOLOTTI, P., TARRÉS, H.C., DYKES, K., MERZ, K., SETHURAMAN, L., VERELST, D. & ZAHLE, F. 2019 IEA wind task 37 on systems engineering in wind energy wp2.1 reference wind turbines. *Tech. Rep.* National Renewable Energy Laboratory (US).
- BOUFIDI, E., LAVAGNOLI, S. & FONTANETO, F. 2020 A probabilistic uncertainty estimation method for turbulence parameters measured by hot-wire anemometry in short-duration wind tunnels. *Trans. ASME J. Engng Gas. Turbines Power* **142** (3), 031007.
- BRANLARD, E. & MEYER FORSTING, A.R. 2020 Assessing the blockage effect of wind turbines and wind farms using an analytical vortex model. *Wind Energy* **23** (11), 2068–2086.
- BRANLARD, E., QUON, E., MEYER FORSTING, A.R., KING, J. & MORIARTY, P. 2020 Wind farm blockage effects: comparison of different engineering models. *J. Phys.: Conf. Ser.* **1618** (6), 062036.
- BROST, R.A., LENSCHOW, D.H. & WYNGAARD, J.C. 1982 Marine stratocumulus layers. Part 1: mean conditions. *J. Atmos. Sci.* **39** (4), 800–817.
- BROST, R.A. & WYNGAARD, J.C. 1978 A model study of the stably stratified planetary boundary layer. *J. Atmos. Sci.* **35** (8), 1427–1440.
- CALAF, M., MENEVEAU, C. & MEYERS, J. 2010 Large eddy simulation study of fully developed wind-turbine array boundary layers. *Phys. Fluids* **22**, 015110.
- CAÑADILLAS, B., FOREMAN, R., STEINFELD, G. & ROBINSON, N. 2023 Cumulative interactions between the global blockage and wake effects as observed by an engineering model and large-eddy simulations. *Energies* **16** (7).
- CANUTO, C., HUSSAINI, M.Y., QUARTERONI, A. & ZANG, T.A. 1988 *Spectral Methods in Fluid Dynamics*. Springer.
- CENTURELLI, G., VOLLMER, L., SCHMIDT, J., DÖRENKÄMPER, M., SCHRÖDER, M., LUKASSEN, L.J. & PEINKE, J. 2021 Evaluating global blockage engineering parametrizations with LES. *J. Phys.: Conf. Ser.* **1934** (1), 012021.

- CHURCHFIELD, M.J., LEE, S., MORIARTY, P.J., MARTINEZ, L.A., LEONARDI, S., VIJAYAKUMAR, G. & BRASSEUR, J.G. 2012 Large-eddy simulation of wind-plant aerodynamics. <https://www.osti.gov/biblio/1047962>.
- CSANADY, G.T. 1974 Equilibrium theory of the planetary boundary layer with an inversion lid. *Boundary-Layer Meteorol.* **6**, 63–79.
- CUSHMAN-ROISIN, B. & BECKERS, J.M. 2011 *Introduction to Geophysical Fluid Dynamics*. Academic.
- DELPORT, S. 2010 Optimal control of a turbulent mixing layer. PhD thesis, KULeuven, Leuven, Belgium.
- DEVESSE, K., LANZILAO, L., JAMAER, S., VAN LIPZIG, N. & MEYERS, J. 2022 Extending the applicability of a wind-farm gravity-wave model to vertically non-uniform atmospheres. *Wind Energy Sci. Discuss.* **2022**, 1–25.
- DURRAN, D.R. & KLEMP, J.B. 1983 A compressible model for the simulation of moist mountain waves. *Mon. Weath. Rev.* **111**, 2341–2361.
- FORNBERG, B. 1996 *A Practical Guide to Pseudospectral Methods*. Cambridge University Press.
- GILL, A.E. 1982 *Atmosphere-Ocean Dynamics*. International Geophysics Series, vol. 30. Academic.
- GOIT, J.P. & MEYERS, J. 2013 Effect of Ekman layer on windfarm roughness and displacement height. In *Proceedings of Direct and Large-Eddy Simulation IX, Dresden, Germany* (ed. J. Frohlich, H. Kuerten, B.J. Geurts & V. Armenio), pp. 423–434. Springer.
- GOIT, J.P. & MEYERS, J. 2015 Optimal control of energy extraction in wind-farm boundary layers. *J. Fluid Mech.* **768**, 5–50.
- HESS, G.D. 2004 The neutral, barotropic planetary boundary layer, capped by a low-level inversion. *Boundary-Layer Meteorol.* **110**, 319–355.
- INOUE, M., MATHEOU, G. & TEIXEIRA, J. 2014 LES of a spatially developing atmospheric boundary layer: application of a fringe method for the stratocumulus to shallow cumulus cloud transition. *Mon. Weath. Rev.* **142**, 1365–1393.
- KIRBY, A., NISHINO, T. & DUNSTAN, T.D. 2022 Two-scale interaction of wake and blockage effects in large wind farms. *J. Fluid Mech.* **953**, A39.
- KLEMP, J.B. & LILLY, D.K. 1977 Numerical simulations of hydrostatic mountain waves. *J. Atmos. Sci.* **35**, 78–107.
- KLEMP, J.B. & LILLY, D.R. 1975 The dynamics of wave-induced downslope winds. *J. Atmos. Sci.* **32** (2), 320–339.
- VAN DER LAAN, M.P., HANSEN, K.S., SØRENSEN, N.N. & RÉTHORÉ, P.E. 2015 Predicting wind farm wake interaction with RANS: an investigation of the coriolis force. *J. Phys.: Conf. Ser.* **625** (1), 012026.
- LANGE, B., LARSEN, S., HØJSTRUP, J. & BARTHELMIE, R. 2004 The influence of thermal effects on the wind speed profile of the coastal marine boundary layer. *Boundary-Layer Meteorol.* **112**(3), 587–617.
- LANZILAO, L. & MEYERS, J. 2022 Effects of self-induced gravity waves on finite wind-farm operations using a large-eddy simulation framework. *J. Phys.: Conf. Ser.* **2265** (2), 022043.
- LANZILAO, L. & MEYERS, J. 2023a A reference database of wind-farm large-eddy simulations for parametrizing effects of blockage and gravity waves. KU Leuven RDR, V1. <https://doi.org/10.48804/L45LTT>.
- LANZILAO, L. & MEYERS, J. 2023b An improved fringe-region technique for the representation of gravity waves in large eddy simulation with application to wind farms. *Boundary-Layer Meteorol.* **186**, 567–593.
- LIN, Y.L. 2007 *Mesoscale Dynamics*. Cambridge University Press.
- LU, H. & PORTÉ-AGEL, F. 2011 Large-eddy simulation of a very large wind farm in a stable atmospheric boundary layer. *Phys. Fluids* **23**, 065101.
- LUNDBLADH, A., BERLIN, S., SKOTE, M., HILDINGS, C., CHOI, J., KIM, J. & HENNINGSON, D.S. 1999 An efficient spectral method for a simulation of incompressible flow over a flat plate. Trita-mek. *Tech. Rep.* 11 KTH.
- MAAS, O. 2022 From gigawatt to multi-gigawatt wind farms: wake effects, energy budgets and inertial gravity waves investigated by large-eddy simulations. *Wind Energy Sci. Discuss.* **2022**, 1–31.
- MAAS, O. 2023 Large-eddy simulation of a 15 GW wind farm: flow effects, energy budgets and comparison with wake models. *Front. Mech. Engng* **9**.
- MAAS, O. & RAASCH, S. 2022 Wake properties and power output of very large wind farms for different meteorological conditions and turbine spacings: a large-eddy simulation case study for the German Bight. *Wind Energy Sci.* **7** (2), 715–739.
- MASON, P.J. & THOMSON, D.J. 1992 Stochastic backscatter in large-eddy simulations of boundary layers. *J. Fluid Mech.* **242**, 51–78.
- MCTAVISH, S., RODRIGUE, S., FESZTY, D. & NITZSCHE, F. 2015 An investigation of in-field blockage effects in closely spaced lateral wind farm configurations. *Wind Energy* **18** (11), 1989–2011.
- MEDICI, D., IVANELLI, S., DAHLBERG, J.A. & ALFREDSSON, P.H. 2011 The upstream flow of a wind turbine: blockage effect. *Wind Energy* **14** (5), 691–697.

- MEYER FORSTING, A.R., TROLDORGBORG, N. & GAUNAA, M. 2017 The flow upstream of a row of aligned wind turbine rotors and its effect on power production. *Wind Energy* **20** (1), 63–77.
- MEYERS, J. & MENEVEAU, C. 2010 Large eddy simulations of large wind-turbine arrays in the atmospheric boundary layer. In *48th AIAA Aerospace Sciences Meeting Including the New Horizons Forum and Aerospace Exposition*. doi:10.2514/6.2010-827.
- MEYERS, J. & SAGAUT, P. 2007 Is plane-channel flow a friendly case for the testing of large-eddy simulation subgrid-scale models? *Phys. Fluids* **19** (4), 048105.
- MOENG, C.H. 1984 A large-eddy-simulation model for the study of the planetary boundary-layer turbulence. *J. Atmos. Sci.* **41**, 2052–2062.
- MUNTERS, W., MENEVEAU, C. & MEYERS, J. 2016 Shifted periodic boundary conditions for simulations of wall-bounded turbulent flows. *Phys. Fluids* **28** (2), 025112.
- MUNTERS, W. & MEYERS, J. 2018 Dynamic strategies for yaw and induction control of wind farms based on large-eddy simulation and optimization. *Energies* **11**, 177.
- NAPPO, C.J. 2002 *An Introduction to Atmospheric Gravity Waves*. International Geophysics Series, vol. 85. Academic.
- NORDSTROM, J., NORDIN, N. & HENNINGSON, D. 1999 The fringe region technique and the Fourier method used in the direct numerical simulation of spatially evolving viscous flows. *SIAM J. Sci. Comput.* **20**, 1365–1393.
- OTTE, M.J. & WYNGAARD, J.C. 2001 Stably stratified interfacial-layer turbulence from large-eddy simulation. *J. Atmos. Sci.* **58** (22), 3424–3442.
- PEDERSEN, J.G., GRYNING, S.-E. & KELLY, M. 2014 On the structure and adjustment of inversion-capped neutral atmospheric boundary-layer flows: large-eddy simulation study. *Boundary-Layer Meteorol.* **153**, 43–62.
- PORTÉ-AGEL, F., BASTANKHAH, M. & SHAMSODDIN, S. 2020 Wind-turbine and wind-farm flows: a review. *Boundary-Layer Meteorol.* **174**, 1–59.
- PORTÉ-AGEL, F., WU, Y.T. & CHEN, C.H. 2013 A numerical study of the effects of wind direction on turbine wakes and power losses in a large wind farm. *J. Energy* **6** (10), 5297–5313.
- RAMPANELLI, G. & ZARDI, D. 2004 A method to determine the capping inversion of the convective boundary layer. *J. Appl. Meteor.* **43**, 925–933.
- SACHSPERGER, J., SERAFIN, S. & GRUBIŠIĆ, V. 2015 Lee waves on the boundary-layer inversion and their dependence on free-atmospheric stability. *Front. Earth Sci.* **3**.
- SANCHEZ GOMEZ, M., LUNDQUIST, J.K., MIROCHA, J.D. & ARTHUR, R.S. 2023 Investigating the physical mechanisms that modify wind plant blockage in stable boundary layers. *Wind Energy Sci. Discuss.* **2023**, 1–28.
- SCHLATTER, P., ADAMS, N. & KLEISER, L. 2005 A windowing method for periodic inflow/outflow boundary treatment of non-periodic flows. *J. Comput. Phys.* **206**, 505–535.
- SCHNEEMANN, J., THEUER, F., ROTT, A., DÖRENKÄMPER, M. & KÜHN, M. 2021 Offshore wind farm global blockage measured with scanning lidar. *Wind Energy Sci.* **6**, 521–538.
- SEGALINI, A. 2021 An analytical model of wind-farm blockage. *J. Renew. Sustain. Energy* **13** (3), 033307.
- SEGALINI, A. & DAHLBERG, J.A. 2019 Blockage effects in wind farms. *Wind Energy* **23** (2), 120–128.
- SMEDMAN, A.S., BERGSTROM, H. & GRISOGONO, B. 1997 Evolution of stable internal boundary layers over a cold sea. *J. Geophys. Res.* **102**, 1091–1099.
- SMITH, R. 2023 The wind farm pressure field. *Wind Energy Sci. Discuss.* **2023**, 1–14.
- SMITH, R.B. 2010 Gravity wave effects on wind farm efficiency. *Wind Energy* **13**, 449–458.
- SMITH, R.B. 2022 A linear theory of wind farm efficiency and interaction. *J. Atmos. Sci.* **79**, 7.
- SPALART, P.R. & WATMUFF, J.H. 1993 Experimental and numerical study of a turbulent boundary layer with pressure gradients. *J. Fluid Mech.* **249**, 337–371.
- SPIEGEL, E.A. & VERONIS, G. 1960 On the Boussinesq approximation for a compressible fluid. *Astrophys. J.* **131**, 442.
- STEVENS, B., MOENG, C.H. & SULLIVAN, P.P. 2000 Entrainment and subgrid length scales in large-eddy simulations of atmospheric boundary-layer flows. *Symp. Dev. Geophys. Turbul.* **58**, 253–269.
- STEVENS, R.J.A.M., GAYME, D.F. & MENEVEAU, C. 2014a Large eddy simulation studies of the effects of alignment and wind farm length. *Phys. Fluids* **6**, 023105.
- STEVENS, R.J.A.M., GAYME, D.F. & MENEVEAU, C. 2016 Effects of turbine spacing on the power output of extended wind-farms. *Wind Energy* **19** (2), 359–370.
- STEVENS, R.J.A.M., GRAHAM, J. & MENEVEAU, C. 2014b A concurrent precursor inflow method for large eddy simulations and applications to finite length wind farms. *Renew. Energy* **68**, 46–50.
- STIEREN, A. & STEVENS, R.J.A.M. 2022 Impact of wind farm wakes on flow structures in and around downstream wind farms. *Flow* **2**, E21.

- STRICKLAND, J.M.I. & STEVENS, R.J.A.M. 2020 Effect of thrust coefficient on the flow blockage effects in closely-spaced spanwise-infinite turbine arrays. *J. Phys.: Conf. Ser.* **1618** (6), 062069.
- STRICKLAND, J.M.I. & STEVENS, R.J.A.M. 2022 Investigating wind farm blockage in a neutral boundary layer using large-eddy simulations. *Eur. J. Mech. (B/Fluids)* **95**, 303–314.
- SUTHERLAND, B.R. 2010 *Internal Gravity Waves*. Cambridge University Press.
- TAYLOR, J.R. & SARKAR, S. 2007 Internal gravity waves generated by a turbulent bottom Ekman layer. *J. Fluid Mech.* **590**, 331–354.
- TAYLOR, J.R. & SARKAR, S. 2008 Direct and large eddy simulations of a bottom Ekman layer under an external stratification. *Int'l J. Heat Fluid Flow* **29**, 721–732.
- TAYLOR, P.K. & YELLAND, M.J. 2000 The dependence of sea surface roughness on the height and steepness of the waves. *J. Phys. Oceanogr.* **31**, 572–590.
- TEIXEIRA, M.A.C. 2014 The physics of orographic gravity wave drag. *Front. Phys.* **2**.
- TÜRK, M. & EMEIS, S. 2010 The dependence of offshore turbulence intensity on wind speed. *J. Wind Engng Ind. Aerodyn.* **98** (8), 466–471.
- VERSTAPPEN, R.W.C.P. & VELDMAN, A.E.P. 2003 Symmetry-preserving discretization of turbulent flow. *J. Comput. Phys.* **187**, 343–368.
- VOSPER, S.B. 2004 Inversion effects on mountain lee waves. *Q. J. R. Meteorol. Soc.* **130** (600), 1723–1748.
- WU, K.L. & PORTÉ-AGEL, F. 2017 Flow adjustment inside and around large finite-size wind farms. *Energies* **10**, 2164.
- WU, Y.-T., LIAO, T.-L., CHEN, C.-K., LIN, C.-Y. & CHEN, P.-W. 2019 Power output efficiency in large wind farms with different hub heights and configurations. *Renew. Energy* **132**, 941–949.
- WU, Y.-T. & PORTÉ-AGEL, F. 2011 Large-eddy simulation of wind-turbine wakes: evaluation of turbine parametrisations. *Boundary-Layer Meteorol.* **138**, 345–366.
- WU, Y.-T. & PORTÉ-AGEL, F. 2013 Simulation of turbulent flow inside and above wind farms: model validation and layout effects. *Boundary-Layer Meteorol.* **146** (2), 181–205.
- WU, Y.T. & PORTÉ-AGEL, F. 2015 Modeling turbine wakes and power losses within a wind farm using LES: an application to the Horns Rev offshore wind farm. *Renew. Energy* **75**, 945–955.
- WYNGAARD, J.C. 2010 *Turbulence in the Atmosphere*. Cambridge University Press.
- YANG, D., MENEVEAU, C. & SHEN, L. 2014a Effect of downwind swells on offshore wind energy harvesting – a large-eddy simulation study. *Renew. Energy* **70**, 11–23, special issue on aerodynamics of offshore wind energy systems and wakes.
- YANG, D., MENEVEAU, C. & SHEN, L. 2014b Large-eddy simulation of offshore wind farm. *Phys. Fluids* **26**, 025101.
- ZILITINKEVICH, S. & ESAU, I. 2003 The effect of baroclinicity on the equilibrium depth of neutral and stable planetary boundary layers. *Q. J. R. Meteorol. Soc.* **129**, 3339–3356.
- ZILITINKEVICH, S., ESAU, I. & BAKLANOV, A. 2007 Further comments on the equilibrium height of neutral and stable planetary boundary layers. *Q. J. R. Meteorol. Soc.* **133** (622), 265–271.
- ZILITINKEVICH, S.S. 1989 Velocity profiles, the resistance law and the dissipation rate of mean flow kinetic energy in a neutrally and stably stratified planetary boundary layer. *Boundary-Layer Meteorol.* **46**, 367–387.
- ZILITINKEVICH, S.S. & ESAU, I.N. 2002 On integral measures of the neutral barotropic planetary boundary layer. *Boundary-Layer Meteorol.* **104**, 371–379.
- ZILITINKEVICH, S.S. & ESAU, I.N. 2005 Resistance and heat-transfer laws for stable and neutral planetary boundary layers: old theory advanced and re-evaluated. *Q. J. R. Meteorol. Soc.* **131** (609), 1863–1892.